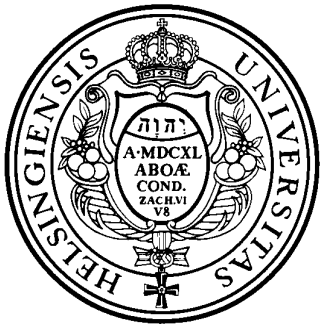

Master's thesis
Geography
Geoinformatics

Atmospheric Correction of a Seasonal Time Series of Hyperion EO-1 Images and Red Edge Inflection Point Calculation

Veli-Heikki Vesanto

2012

Supervisor:
Matti Mõttus

UNIVERSITY OF HELSINKI
DEPARTMENT OF GEOSCIENCES AND GEOGRAPHY
DIVISION OF GEOGRAPHY

P.O. Box 64 (Gustaf Hällströmin katu 2)
00014 University of Helsinki

HELSINGIN YLIOPISTO – HELSINGFORS UNIVERSITET – UNIVERSITY OF HELSINKI

Tiedekunta/Osasto – Fakultet/Sektion – Faculty/Section	Laitos – Institution – Department
Faculty of Science	Depatment of Geosciences and Geography

Tekijä – Författare – Author
Vesanto Veli-Heikki

Työn nimi – Arbetets titel – Title
Atmospheric Correction of a Seasonal Time Series of Hyperion EO-1 Images and Red Edge Inflection Point Calculation

Oppiaine – Läroämne – Subject
Geoinformatics

Työn laji – Arbetets art – Level	Aika – Datum – Month and year	Sivumäärä – Sidoantal – Number of pages
Master's thesis	June 2012	74

Tiivistelmä – Referat – Abstract

While spaceborne satellite data has been extensively used to extract biophysical forest characteristics through reflectance features and indices, there are still many questions regarding seasonal changes in reflectance. Boreal forests have already seen changes in growth patterns from climate change, and the large scale monitoring of these forests is becoming more important. Understanding seasonal changes in reflectance in the boreal region will allow for the monitoring of seasonal biophysical changes using satellite imagery. For this monitoring to be possible the satellite imagery needs to be preprocessed and atmospherically corrected to create a time series of hemispherical-directional reflectance factors.

The red edge is the abrupt change in reflectance between 680 and 740 nm seen in vegetation spectra. The red edge inflection point is the wavelength, at which the slope is steepest in the red edge. The red edge inflection point is sensitive to plant chlorophyll content and has been extensively used for estimating vegetation biophysical parameters including: leaf-area index, biomass and plant health levels. Hyperion is a narrowband imaging spectrometer aboard the Earth Observer-1 satellite. Hyperion captures data across 242 spectral bands covering a spectral range of 356 to 2577 nm resulting in a nominal spectral range of 10 nm. While the high spectral resolution of Hyperion makes it possible to calculate the REIP, there is no consensus on how this should be done, with different methods producing conflicting results.

This study explains the preprocessing and atmospheric correction of a seasonal time series of five Hyperion EO-1 images (Provided courtesy of the USGS) from Hyytiälä, Southern Finland (61° 51 N, 24° 17 E). The time series ranges from 31.5.2010 to 12.8.2010, covering much of the growing season and the seasonal changes in reflectance. The first derivative, four-point linear interpolation, Lagrangian interpolation, and fifth-order polynomial fitting methods for calculating the REIP are looked at to determine their applicability for Hyperion imagery using this time series.

Hyperion data requires considerable preprocessing before atmospheric correction can be done. In this study the preprocessing covered: destriping, desmiling, atmospheric correction and finally geocorrection. Atmospheric correction was done using both FLAASH and ATCOR, both of which are MODTRAN based absolute atmospheric correction algorithms. The final atmospherically corrected HDRF images were evaluated using in situ handheld spectrometer reference measurements of a grass field in the area. An average RMSE value of around 3% was achieved with both algorithms. The corrected Hyperion images were also compared against two MODIS products, which also showed good agreement. The aerosol retrieval however did not work with either algorithm, on any scene. The use of a sun photometer for aerosol level estimation was also not effective.

Due to the dynamics of the red edge and expected seasonal red edge inflection point trends, the fifth-order polynomial fitting method was seen as the best method for calculating the red edge inflection point. The red edge inflection point did not correlate strongly with leaf area index overall, however there was a strong correlation with individual plots. A strong correlation was observed between Hyperion red edge inflection point and understory red edge inflection point, both overall and for individual plots.

Avainsanat – Nyckelord – Keywords
Hyperion, Hyperspectral, Atmospheric Correction, Red Edge Inflection Point, FLAASH, ATCOR

Säilytyspaikka – Förvaringställe – Where deposited
University of Helsinki, Kumpula Science Library

Muita tietoja – Övriga uppgifter – Additional information

HELSINGIN YLIOPISTO – HELSINGFORS UNIVERSITET – UNIVERSITY OF HELSINKI

Tiedekunta/Osasto – Fakultet/Sektion – Faculty/Section	Laitos – Institution – Department
Matemaattis-luonnontieteellinen tiedekunta	Geotieteiden ja maantieteen laitos

Tekijä – Författare – Author
Vesanto Veli-Heikki

Työn nimi – Arbetets titel – Title
Atmospheric Correction of a Seasonal Time Series of Hyperion EO-1 Images and Red Edge Inflection Point Calculation

Oppiaine – Läroämne – Subject
Geoinformatiikka

Työn laji – Arbetets art – Level	Aika – Datum – Month and year	Sivumäärä – Sidoantal – Number of pages
Pro Gradu - tutkielma	Kesäkuu 2012	74

Tiivistelmä – Referat – Abstract

Kaukokartoitusmenetelmiä on pitkään käytetty metsän biofyysisten ominaisuuksien arvioinnissa, käyttäen hyväksi niiden heijastusominaisuuksia ja kasvillisuusindeksejä. Metsän heijastuksen muutokset kasvukauden aikana eivät kuitenkaan ole täysin ymmärrettyjä. Boreaalisten metsien kasvussa on havaittu muutoksia ilmastonmuutoksen myötä, minkä vuoksi niiden monitorointi on erityisen tärkeää. Kaukokartoitusaineistoon pohjautuvaan monitorointiin vaaditaan ymmärrystä metsien heijastusominaisuuksien muutoksista kasvukauden aikana. Tätä myöten käytettävän aineiston täytyy olla esikäsitelty ja ilmakehäkorjattu.

Niin kutsuttu punainen reuna (red edge) on tyypillinen ominaisuus kasvillisuuden heijastuksessa, joka näkyy äkillisenä muutoksena heijastuksessa 680 ja 740 nm välillä. Punaisen reunan käännepiste (red edge inflection point) on se aallonpituus, jossa heijastuksen muutos on jyrkimmillään. Punaisen reunan käännepiste on herkkä klorofyllin määrälle kasvillisuudessa, ja sitä on käytetty arvioimaan kasvillisuuden biofyysisiä parametreja, kuten lehtialaindeksiä, biomassaa ja kasvillisuuden terveyttä. Hyperion on kapeakanavainen kuvaava spektrometri EO-1 satelliitissa. Hyperion mittaa aallonpituusalueen 356 – 2577 nm heijastusta 242 kanavalla, ja sensorin nominaalinen spektrinen resoluutio on 10 nm. Korkea spektrinen resoluutio mahdollistaa punaisen reunan käännepisteen laskemisen. Laskemiseen on kuitenkin useita menetelmiä, jotka tuottavat erilaisia tuloksia.

Tämä Pro Gradu - tutkielma kattaa viiden Hyperion EO-1 kuvan esikäsittelyn ja ilmakehäkorjauksen. Kuvat ovat Hyytiälästä, Etelä-Suomesta (61 ° 51 N, 24 ° 17 E). Aikasarja alkaa 5. toukokuuta 2010 ja päättyy 11. heinäkuuta 2010, kattaen suurimman osan kasvukaudesta ja kasvillisuuden heijastuksen vaihtelusta. Seuraavia punaisen reunan käännepisteen laskentamenetelmien soveltuvuutta testattiin Hyperion-aineistolla: neljän pisteen lineaarinen interpolaatio, Lagrangian interpolaatio, ja viidennen asteen yhtälön sovittaminen.

Hyperion-data vaatii paljon esikäsittelyä ennen kuin ilmakehäkorjaus voidaan suorittaa. Tässä tutkielmassa esikäsittely kattoi seuraavat vaiheet: spektrisen hymyn poisto, viivojen poisto, ilmakehäkorjaus, ja lopuksi geometrinen korjaus.

Ilmakehäkorjaus toteutettiin käyttäen FLAASH ja ATCOR -algoritmeja, jotka ovat absoluuttisia ilmakehäkorjauksia ja käyttävät MODTRAN -algoritmia ilmakehän mallinnuksessa. Lopullisten, ilmakehäkorjattujen kuvien heijastusta verrattiin maastossa mitattuun tukiaineistoon. Maastoaineisto mitattiin tutkimusalueella sijaitsevalla ruohokentällä. Molemmat algoritmit tuottivat hyvän tuloksen, mutta kummankaan algoritmin automaattinen aerosolin määrän arviointi ei toiminut. Myöskään arviointi aurinkofotometrin avulla ei toiminut. Korjatut Hyperion-kuvat sopivat kuitenkin hyvin yhteen verrattaessa niitä kahteen MODIS-tuotteeseen.

Punaisen reunan dynamiikan takia viidennen asteen yhtälön sovittaminen punaiseen reunaan todettiin parhaaksi menetelmäksi laskea punaisen reunan käännepiste. Hyperion-aineistosta johdettu punaisen reunan käännepiste ei korreloitunut voimakkaasti lehtialaindeksin kanssa, vaikka yksittäiset koealat korreloivatkin vahvasti. Sen sijaan Hyperion-aineiston punaisen reunan käännepisteen ja aluskasvillisuuden punaisen reunan käännepisteen välillä oli hyvin vahva korrelaatio.

Avainsanat – Nyckelord – Keywords
Hyperion, Hyperspektrinen, Ilmakehäkorjaus, Punaisen reunan käännepiste, FLAASH, ATCOR

Säilytyspaikka – Förvaringställe – Where deposited
Helsingin yliopisto, Kumpulan tiedekirjasto

Muita tietoja – Övriga uppgifter – Additional information

TABLE OF CONTENTS

LIST OF TERMS

AERONET	AErosol RObotic NETwork
AOD	Aerosol Optical Depth
ASD	Analytical Spectral Devices
ATCOR	ATmospheric CORrection
BRDF	Bidirectional Reflectance Distribution Function
CNES	Centre National d'Études Spatiales
CHRIS	Compact High Resolution Imaging Spectrometer
CV-MVC	Constrained View Angle – Maximum Value Composite
DLR	Deutsche Forschungsanstalt für Luft- und Raumfahrt (German Aerospace Research Establishment)
DN	Digital Number
DOS	Dark Object Subtraction
EL	Empirical Line
EnMAP	Environmental Mapping and Analysis Program
EO-1	Earth Observing-1
ESA	European Space Agency
EVI	Enhanced Vegetation Index
FLAASH	Fast Line-of-sight Atmospheric Analysis of Spectral Hypercubes
FWHM	Full-Width at Half Maximum
GIS	Geographic Information System
HDRF	Hemispherical-Directional Reflectance Factor
HYSPIRI	Hyperspectral Infrared Imager
ISA	Israeli Space Agency
KT method	Method for retrieving aerosol levels from reflectance outlined by Kaufman et. al. (2007)
LAI	Leaf Area Index
MCD43A4	Nadir BRDF-Adjusted Reflectance 16-Day L3 Global 500m
MD	Mean Deviation
MISR	Multi-angle Imaging Spectro-Radiometer
MNF	Minimum Noise Fraction
MOD13Q1	Vegetation Indices 16-Day L3 Global 250m
MODIS	Moderate Resolution Imaging Spectroradiometer
NASA	National Aeronautics and Space Administration
NDVI	Normalized Difference Vegetation Index
NIR	Near Infrared
REIP	Red Edge Inflection Point
RMSD	Root Mean Square Deviation
SIN	Sinusoidal Grid
SMEAR	Station for Measuring Forest Ecosystem - Atmosphere Relations
SPECMM	Spectral Moment Matching
SPOT	Le Systéme Pour l'Observation de la Terre
STD	Standard Deviations
SWIR	Shortwave Infrared

ETM+	Landsat Endhanced Thematic Mapper Plus
UAV	Unmanned Aerial Vehicle
USGS	United States Geological Survey
VALERI	Validation of Land European Remote Sensing Instruments
VENμS	Vegetation and Environmental New micro Spacecraft
VNIR	Visible and Near Infrared
WRS-2	World Reference System-2

1. INTRODUCTION

Boreal forests have already seen changes in growth patterns from climate change, increasing the demand for the large scale monitoring of these forests (Myneni *et al*., 1997). While small scale monitoring is possible on a site by site basis through *in situ* data collection, large scale monitoring requires the use of remote sensing. Remote sensing can be defined as the "practice of deriving information about the earth's land and water surfaces using images acquired from an overhead perspective, using electromagnetic radiation in one of more regions of the electromagnetic spectrum, reflected or emitted from the earth's surface" (Campbell, 1996, p.5). There is no specification of what classifies as 'remote', however generally remote sensing can be divided into two classes based on remoteness: airborne and spaceborne. Airborne containing all data captured from the air: balloons, aircraft, helicopter or Unmanned Aerial Vehicle (UAV). Spaceborne covers data captured from satellites. Key to remote sensing is that the data is acquired within a spatial reference; the data can be directly related to a specific area on the ground. Processing of remote sensing data can thus be done within a Geographic Information System (GIS). A GIS can be defined as "an integrated collection of computer software and data … [for] gathering and organizing spatial data and related information so it can be displayed and analyzed" (Wade and Sommer, 2006, p.90).

The boreal region witnesses large seasonal variations in incoming solar irradiance and vegetation structure. The spectral reflectance of boreal forests is thus dependent on the seasonal timing of the measurement, which complicates its temporal monitoring. Understanding the seasonal changes in reflectance is essential for any accurate monitoring of vegetation in boreal forests. To study the seasonal changes in reflectance over the growing season, a time series of preprocessed and atmospherically corrected hemispherical-directional reflectance factors (HDRF) is needed.

While spaceborne satellite data has been extensively used to extract biophysical forest characteristics through reflectance characteristics and indices, there are still many questions regarding seasonal changes in reflectance. Current spaceborne remote sensing is dominated by earth-observing satellites with broadband imaging sensors, including among others Landsat Endhanced Thematic Mapper Plus (ETM+) and le Systéme Pour l'Observation de la Terre (SPOT) (Thenkabail *et al*., 2000). Broadband sensors are limited in their applicability for much vegetation monitoring. The coarse spectral resolution is unable to detect narrow spectral features that are sensitive to biophysical forest parameters. This has prompted the development of hyperspectral sensors. The term hyperspectral in this study refers to a

narrowband imaging spectrometer that takes contiguous spectral measurements for a certain spectral range. Imaging means that these spectral measurements are made in a contiguous manner geographically. Thus, the final product is a datacube containing geographic information on the X-Y plane, and spectral information in the Z direction (Bannon, 2009).

The current field of hyperspectral imaging is dominated by airborne sensors, due to their availability and commercial viability. Currently there are only two spaceborne hyperspectral sensors operational. Hyperion aboard the National Aeronautics and Space Administration (NASA) Earth Observing-1 (EO-1) satellite and Compact High Resolution Imaging Spectrometer (CHRIS) aboard the ESA (European Space Agency) Proba-1 satellite. Neither of which provide continuous coverage of large land areas. The future however looks bright for hyperspectral satellite imaging, with multiple sensors currently being developed, increasing the importance of studying the applicability of spaceborne hyperspectral sensors (Puschell, 2000). Currently in the production and planning stages are among others: Vegetation and Environmental New micro Spacecraft (VENμS), Sentinel-2, Hyperspectral Infrared Imager (HYSPIRI), and Environmental Mapping and Analysis Program (EnMAP). Of these only HYSPIRI and EnMAP are truly hyperspectral, with contiguous bands over a wavelength range. While VENμS and Sentinel-2 can be called superspectral, with 10 or more spectral bands focused of certain spectral features (Maliet and Poinsignon, 2006). They provide a higher number of spectral bands then currently available high spatial resolution multispectral sensors.

VENμS will be launched in 2014 as a collaboration between CNES (Centre National d'Études Spatiales) and ISA (Israeli Space Agency) (CNES, 2011). The instrument will capture data with twelve narrow bands ranging from 415 to 910 nm; with the bands spaced out to measure specific spectral features (Herrmann *et al*., 2010). The ESA Sentinel-2 mission will consist of two satellites being launched in 2013. With thirteen spectral bands covering a range from 443 nm to 2190 nm, like VENμS spaced out to capture specific spectral features (ESA, 2011). HYSPIRI is a NASA project which combines a hyperspectral sensor with a thermal infrared multispectral sensor, with a launch date planned for between 2013 and 2019. The hyperspectral sensor will cover a range from 380 to 2500 nm, at a spectral resolution of 10nm, and a spatial resolution of 60 m. The instrument will be always on, with a temporal revisit time of 5 days at the equator, with the possibility of tilting for even lower temporal resolution for high priority targets (NASA, 2009a). EnMAP is being developed by the German Aerospace Center (DLR) with a planned launch in 2015. The sensor will capture 249

bands covering a spectral range from 420 nm to 2450 nm (DLR, 2012). This study will focus on the currently available Hyperion sensor aboard the NASA EO-1 satellite. Hyperion captures data across 242 spectral bands covering a spectral range of 356 to 2577nm resulting in a nominal spectral range of 10nm.

There are numerous methods for relating remote sensing data to biophysical parameters, including vegetation indices, landscape indicators and patch metrics (Jensen, 2000). All of the current methods however have their limitations, with saturation being a key concern. Parameter estimation works to a certain level, after which the parameter saturates and differences cannot be detected (Mutanga and Skidmore, 2004). The spectral resolution of hyperspectral remote sensing allows us to look at specific parts of the spectrum, like the red edge. The red edge is the abrupt change in reflectance between 680nm and 740nm seen in vegetation spectra. The Red Edge Inflection Point (REIP) is the wavelength, at which the slope of reflectance plotted against wavelength is steepest within the red edge. The REIP is sensitive to plant chlorophyll content and has been extensively used for estimating vegetation biophysical parameters including Leaf Area Index (LAI), biomass and plant stress (Filella and Peñuelas, 1994; Kodani *et al*., 2001; Pu *et al*., 2003; Herrmann *et al*., 2010). The high spectral resolution of Hyperion makes it possible to calculate the REIP; however there is no consensus on how this calculation should be done, and different methods produce conflicting results.

1.1. Aims

1) To create a pre-processed and atmospherically corrected seasonal time series of Hyperion images, showing top of canopy HDRF, comparing two atmospheric correction algorithms.

2) Evaluate the uncertainties and temporal consistency of this time series, using *in situ* measured reflectance and Moderate Resolution Imaging Spectroradiometer (MODIS) satellite imagery.

3) Determine the applicability of the REIP calculated from Hyperion data, comparing the available calculation methods, and to analyze the seasonal dynamics of the boreal forest REIP.

4) Look at the correlation between the REIP from Hyperion data, REIP from understory reflectance and canopy level LAI.

2. LITERATURE REVIEW

2.1. Hyperion

Hyperion is a narrow-band hyperspectral sensor aboard the NASA EO-1 satellite. Hyperion captures data in the 'pushbroom' manner, with a single measurement made through a slit covering 30 m along-track and 7.7 km across-track on the ground. The along-track measurement consists of a single pixel, with the across-track direction consisting of 256 pixels, resulting in a spatial resolution of 30 m by 30 m on the ground. The forward motion of the satellite, at an altitude of 705 km, shifts the slit to the next along-track row. The data is truly hyperspectral with a spectral range of 357 to 2576 nm covered by 242 bands. Each band covers a nominal spectral range of 10nm with approximately 11nm full-width at half maximum (FWHM). To increase the signal-to-noise ratio, the bands are split between two spectrometers, one for Visible and Near Infrared (VNIR) and the other for Shortwave Infrared (SWIR) (Pearlman *et al*., 2003). A dichroic filter reflects the wavelengths from 357 to 1058nm to the VNIR spectrometer and wavelengths from 852 to 2576 nm to the SWIR spectrometer, leaving a spectral overlap between the two sensors between 852 and 1058nm allowing for cross calibration (Ungar *et al*., 2003). Hyperion data capture is performed upon request, with scene lengths varying from 42km to 185km (USGS, 2011). As of the fifth of August 2009, data acquisition requests could be made at no cost (USGS, 2010a). Hyperion has a 16-day nadir temporal resolution following the World Reference System-2 (WRS-2) path and row system. In addition, the sensors aboard EO-1 are capable of cross-track pointing, allowing for imaging of the adjacent WRS-2 path. While the look angle can vary from 19.976 to -19.976 degrees (the scene width is always a consistent 7.7km) there is an increased risk of pixel distortion and band-to-band misalignment with larger look angles (USGS, 2010b).

Out of the potential 242 spectral bands, a number lack illumination or have a very low spectral response. These bands are left uncalibrated and set to 0 in the final products. This leaves 198 bands that contain spectral data, bands 8-57 in VNIR (436-926 nm) and bands 77-224 in SWIR (933–2406 nm) (CSIRO, 2002). The final end user products, level 1A and 1B, are provided as calibrated radiance (W/m^2 sr μm), with a gain factor of 40 applied to the VNIR and 80 to the SWIR (Barry, 2001). Level 1 processing flows contain a series of steps that correct echo and smear from the raw images; in addition the 198 bands are radiometrically calibrated. Level 1B differs from 1A in that the SWIR bands in 1B and shifted to achieve a better spatial alignment with the VNIR bands (Barry, 2001). Due to the different readout techniques between the VNIR and SWIR focal planes, there is a misalignment

between the VNIR and SWIR bands. The actual shift is angular, with the VNIR bands being rotated 0.22° from the SWIR bands (Khurshid *et al*., 2006; McVicar, 2001). Simplified the shift can be explained as a one pixel shift in the across-track direction and a shift in the along-track direction that is dependent on position, starting as a shift of -0.5 in the first column and linearly progressing to a one pixel shift by the final column (Pearlman *et al*., 2003). In Level 1B products, the shift is simply dealt with by moving the SWIR bands one pixel to the left and shifting rows 129-256 one pixel down (Barry, 2001). This improves the spatial alignment between SWIR and VNIR without any loss of data from resampling, however, at worst the misalignment between the VNIR and SWIR pixels is still up to half a pixel (Pearlman *et al*., 2003).

2.2. Hyperion processing

The main advantage of Hyperion data over multispectral satellite imagery is the high spectral resolution. This allows for the identification of spectral features impossible to detect with lower resolution SPOT or Landsat imagery. However, even the end user products require extensive processing before they can be utilized. A number of processing steps have been outlined by Goodenough *et al*. (2003), Datt *et al*. (2003) and Khurshid *et al*. (2006). The main steps consist of spatial shift correction between SWIR and VNIR, destriping, smile correction, atmospheric correction and geocorrection. In addition, noise reduction, keystone correction, and angular shift correction can also be performed (Khurshid *et al*., 2006).

While the misalignment between the VNIR and SWIR bands has been corrected to an extent in the Level 1B processing, further steps have been suggested. Because the correction applied in the Level 1B processing does not require any resampling it can easily be undone and a more complex processing can be applied. McVicar (2001) suggests a '-0.25 to 1 and –1' shift; meaning that the SWIR is shifted to the VNIR in the across-track direction by starting at line 1 with a -0.25 shift and linearly progressing to a +1 shift by line 256. The along-track is then shifted -1 for the whole image. Khurshid *et al*. (2006) alternatively suggests a partial removal of Level 1B processing by shifting lines 129-256 in the SWIR to their original along-track position, one pixel higher. The VNIR bands of the image are then rotated 0.22° counter clockwise. The VNIR is chosen for resampling due to the lower radiometric fidelity. Both of these methods however require a resampling of either the VNIR or SWIR, which will lead to a loss of spectral accuracy.

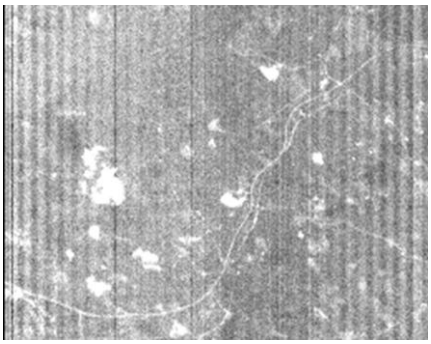

Figure 1. Hyperion band 8 with clearly evident striping, both missing lines (far left column) and variations in brightness.

Hyperion suffers from systematic striping along-track, affecting both the VNIR and SWIR bands. The striping can be broadly divided into two classes: completely missing the lines and stripes. The missing lines contain no information and can be identified and replaced using the values from either spatially or spectrally adjacent pixels (Goodenough *et al*., 2003). Goodenough *et al*. (2003) suggests a process of local destriping for this, which looks at the first pixel in each column to identify potential stripes by checking if the pixel has a lower value than both spatially adjacent pixels, if so the column is flagged as a potential stripe. The flagged columns are then checked to see if over 50% of the pixels are lower than the adjacent pixels and a continuous stretch of over five pixels is found with lower values. When these conditions are met, the column is replaced by the mean value of either the spatially or spectrally adjacent pixels.

The actual striping is more difficult to correct, and can be seen as columns with clearly abnormal brightness values, compared to the spatially or spectrally adjacent columns (Figure 1). The amount of striping in an image is a function of the instrument temperature. There is however no accurate way to predict the striping in Hyperion imagery. While the stripes contain valid image information, their brightness differs from the overall image (Sun *et al*., 2008). Sun *et al*. (2008) outline a Spectral Moment Matching (SpecMM) approach to removing stripes. Because of the high spectral resolution of Hyperion data, there is high autocorrelation between the along-track columns in different bands. This makes it possible to compare the statistics of corresponding along-track columns. Briefly outlined the Sun *et al*. (2008) SpecMM method first calculates the means and standard deviations (STD) for each along-track column in the image and can be called the original mean and original STD. Then highly correlated bands are determined based on spatially smoothed original mean and STD profiles. The original means and STDs of the highly correlated bands are then averaged to create an expected mean and STD. The difference between the expected mean and STD and original mean and STD are used to calculate a gain and offset value for each column in a band. The gain and offset values are then applied to each individual pixel.

Hyperion data exhibits a shift in the wavelength of each column in the across-track direction from central wavelength of the band. This shift, known as spectral smile, is characteristic to pushbroom sensors and is a result of different optical paths leading to the receiving elements. The shift is a function of wavelength and the position of the receiving element within the receiving array. In Hyperion data, the spectral shift manifests itself as a 'frown', with the wavelengths of the columns near the edges of each band shifting negatively from the band's average wavelength. The shift is most clearly evident in the VNIR bands (Barry, 2001). While it is hard to detect from single bands, the spectral smile in individual bands it can be visualized in two ways. Firstly, a Minimum Noise Fraction (MNF) forward rotation can be used (Goodenough *et al*., 2003). The MNF rotation is performed separately on the VNIR and SWIR bands due to the differing nature of the smile in the two detectors. A clear gradient can be seen in Figure 2, in the across-track direction after a MNF rotation is applied to the VNIR bands of a FLAASH atmospherically corrected Hyperion image, which can be attributed to spectral smile. The other way to visualize spectral smile is by performing a simple band math operation around an atmospheric absorption feature. The result of subtracting two bands from each other, which are located either side of a spectral absorption feature should be near zero, with any remaining signal likely caused by noise. Figure 2 shows the results of band subtraction around the 752 nm oxygen absorption feature, by subtracting

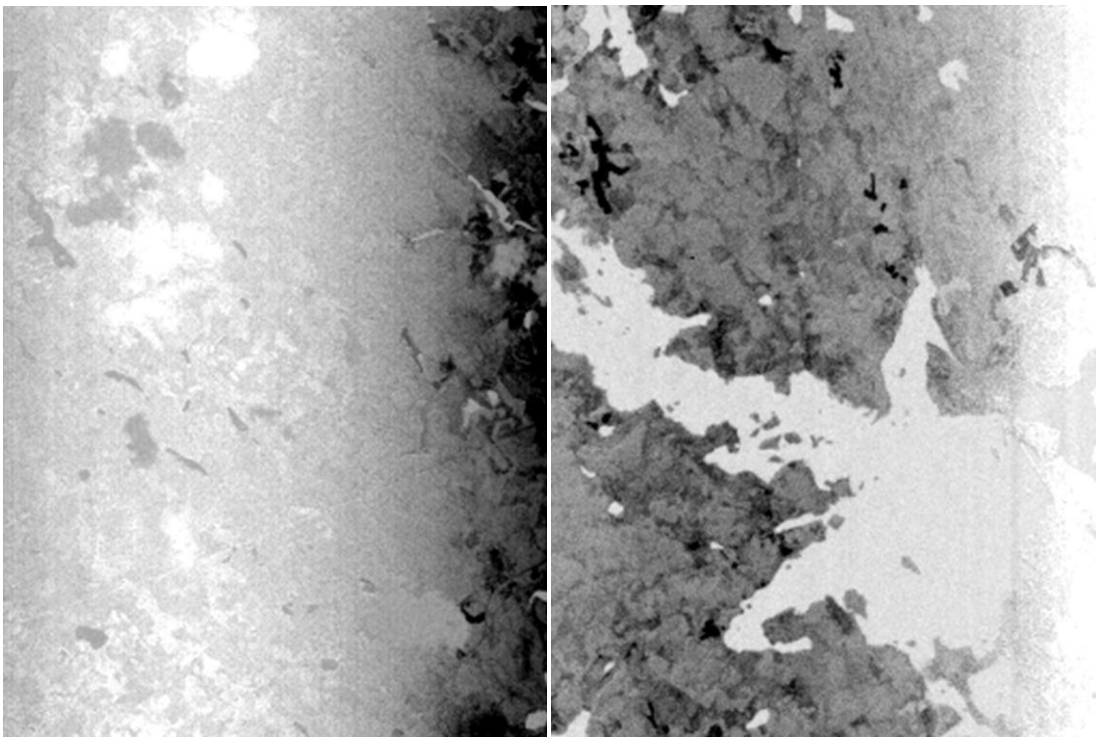

Figure 2. Result of a MNF rotation on the VNIR bands of a Hyperion image showing a clear gradient in the across-track direction due to spectral smile (left). Band math around the 752 nm oxygen absorption feature (Hyperion bands 40 – band 42) (right).

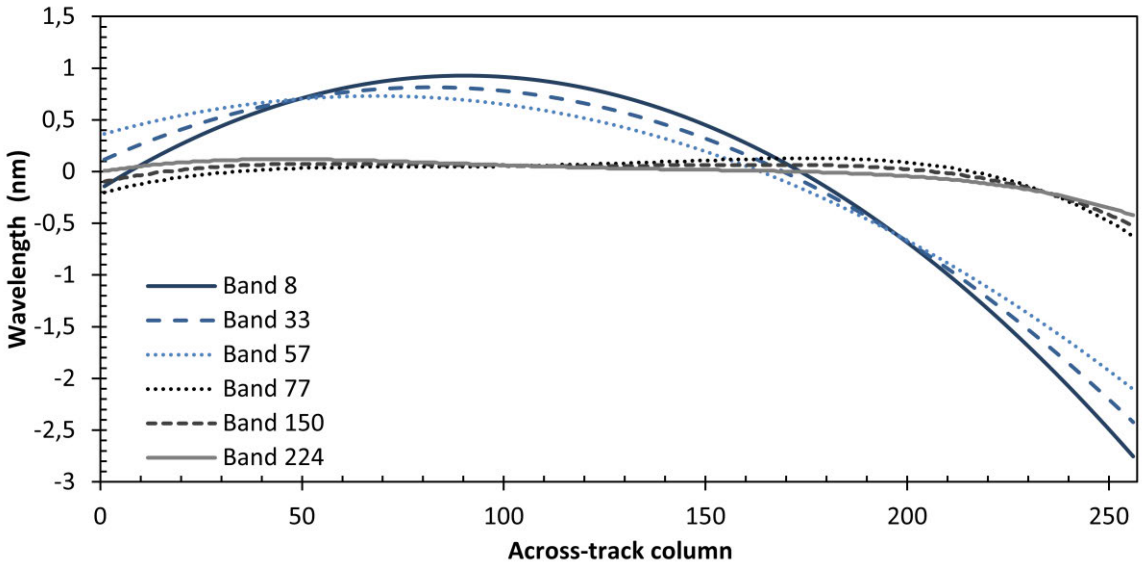

Figure 3. Pre-launch laboratory measured spectral response from Hyperion.

Hyperion band 42 from band 40 in a FLAASH atmospherically corrected Hyperion image. A clear gradient can be seen in the across-track direction due to spectral smile.

There are a number of suggested methods for the removal of smile. There is however no clear or widely accepted method. Goodenough *et al*. (2003) outlines three potential methods for desmiling: moving linear fitting and interpolation, column mean adjusted in radiance space, and column mean adjusted in MNF space. The latter two methods created false spectra and resulted in a loss of spectral fidelity. The moving linear fitting provided the best results but is reliant on accurate measurements of the offset for each column in each band. The method uses a moving linear fitting to interpolate all of the bands to a common wavelength using the pre-launch laboratory measurements (Figure 3).

ATCOR offers an option to estimate spectral smile using atmospheric gas absorption features or solar Fraunhofer lines. Sharp absorption features resulting in drops in reflectance can be used quantify the extent of smile in hyperspectral imagery. The shift in wavelength due to spectral smile is generally hard to detect, due to the correlation between adjacent wavelengths. If part of a band is affected by an absorption feature the shift can be significant. The extent of the spectral smile can be estimated using known absorption features (Richter and Schläpher, 2011). These estimates could then be used instead of the pre-launch laboratory measurements.

Ideally the amount of radiant energy recorded by a sensor is a direct function of the amount of radiance leaving the terrain at a specific view angle (Jensen, 2000). Unfortunately

the radiant energy received by the remote sensing system is made up of energy following different paths through the atmosphere (Figure 4):

Path 1) Contains the spectral solar irradiance that was very weakly impacted by the atmosphere before illuminating the target. Thus the ammount of irradiance reaching the terrain through this path is a function of the atmospheric transmittance.

Path 2) Contains the spectral diffuse sky irradiance, which never reaches the the Earth's surface.

Path 3) Contains energy that has been scattered and potentially impacted by absorption in the atmosphere before illuminating the target.

Path 4) Contains the radiation that is reflected by nearby terrain into the remotes sensing system.

Path 5) Is the energy reflected from nearby terrain into the atmosphere and subsequently scattered into the target.

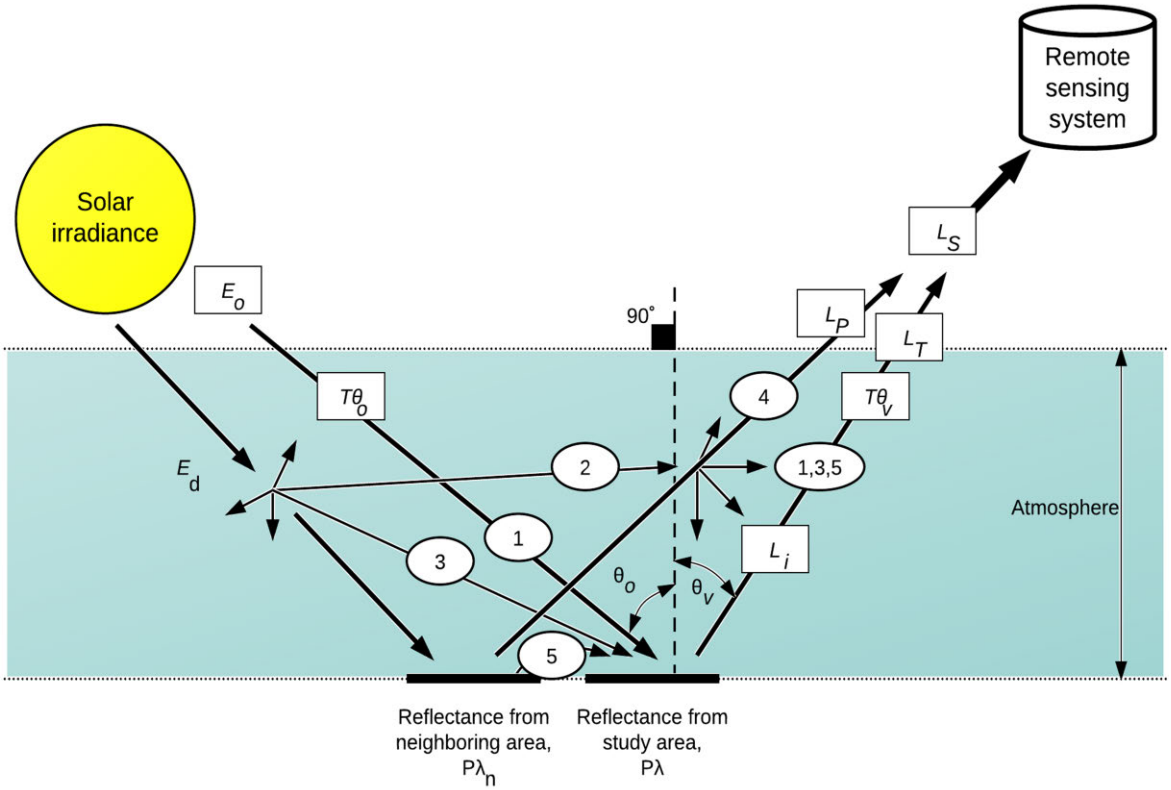

Figure 4. Paths of radiance received by a remote sensing system (after Jensen 2000, Figure 2-20, p. 50). Radiance (L_T) from paths 1, 3, and 5 contains spectral information about the target of interest. Path radiance (L_P) from paths 2 and 4 includes diffuse sky irradiance or radiance from neighbouring areas.

Table 1. Radiometric variables

E_o	Solar irradiance at the top of the atmosphere
E_{o_λ}	Spectral solar irradiance at the top of the atmosphere
E_d	Diffuse sky irradiance to surface
E_{d_λ}	Spectral diffuse sky irradiance to surface
E_g	Global irradiance incident on the surface
E_{g_λ}	Spectral global irradiance on the surface
τ	Normal atmospheric optical thickness
T_θ	Atmospheric transmittance at an angle θ to the zenith
θ_o	Solar optical angle
θ_v	View angle of the satellite sensor (look angle)
r_λ	Average target reflectance at a specific wavelength
r_{λ_n}	Average reflectance from a neighboring area
L_s	Total radiance at sensor
L_T	Total radiance from the target of interest toward the sensor
L_i	Intrinsic radiance of the target (what a handheld spectroradiometer would record on the ground without any intervening atmosphere)
L_P	Path radiance from multiple scattering
E_n	Energy reflected from nearby terrain into the target

The total solar irradiance reaching the Earth's surface at a specific electromagnetic wavelenght range (λ_1 to λ_2) is mainly made up of a number of components from paths 1, 3, and 5 (Figure 4, Table 1):

$$E_{g_\lambda} = \int_{\lambda_1}^{\lambda_2} (E_{o_\lambda} T_{\theta_o} cos\theta_o + E_{d_\lambda} + E_{n_\lambda})\, d\lambda$$

Of this irradiance reaching the surface only a small amount is reflected in the direction of the remote sensing system. If we assume a perfectly reflecting lambertian surface, the total amout of radiance exiting towards the remote sensing sytem is:

$$L_T = \frac{1}{\pi} \int_{\lambda_1}^{\lambda_2} r_\lambda T_{\theta_v} (E_{o_\lambda} T_{\theta_o} cos\theta_o + E_{d_\lambda} + E_{n_\lambda})\, d\lambda$$

Some of the incoming irradiance is selectively absorbed by the terrain so the average target reflectance factor (r_λ) is included.

The final radiance recorded by the remote sensing system can then be written as:

$$L_s = L_T + L_P$$

We can see from Figure 4 that the path radiance (L_P) is an intrusive component consisting of the diffuse sky irradiance from path 2 as well as the reflectance from nearby ground areas from path 4.

The goal of atmospheric correction is to retrieve the intrinsic radiance of the target (L_i) from the signal received by the sensor (L_s). This requires the removal of the intrusive component L_P, in addition to removing the impact of atmospheric transmittance (T_θ) from the total radiance from the target toward the sensor (L_T).

The impacts of the atmosphere on the final signal received by the satellite can be corrected in two general ways: relative atmospheric correction or absolute atmospheric correction. Relative atmospheric correction is used to normalize the intensities of different bands within a scene. This does not generally require the knowledge of atmospheric variables. A relatively corrected scene cannot be directly compared to another scene with different atmospheric or solar conditions (Jensen, 1996). To remove the impacts of the atmosphere completely, absolute atmospheric correction is needed. Absolute atmospheric correction produces a reflectance factor (generally HDRF) for the scene that is comparable to the same reflectance factors retrieved from other dates or other scenes.

While there are a number of different forms of atmospheric correction, they are fundamentally based on two basic steps: parameter estimation and surface reflectance retrieval (Liang *et al*., 2001). If the parameters can be estimated accurately, the retrieval of surface reflectance from a well calibrated instrument is relatively straightforward. Absolute atmospheric correction thus generally requires either information about atmospheric conditions or *in situ* reflectance measurements.

Using *in situ* based reflectance measurements the Empirical Line (EL) method can be used for atmospheric correction. The EL method assumes that the atmospheric conditions for a scene are homogeneous and using specific calibration targets, which have a known surface reflectance, the reflectance factors for the rest of the scene can be calculated (Clark *et al*.,

2010). Ideally these calibration targets would be measured at the same time the scene is captured. The targets need to be as homogeneous as possible, cover an area of multiple pixels in the satellite image, and be as near-Lambertian as possible (Karpouzli and Malthus, 2003). At least one bright calibration site and one dark site is needed. Using these calibration sites, the satellite pixels are linearly regressed against the *in situ* reflectance spectra to derive the gain and offset curves (Gao *et al*., 2006). The gain and offset curves are then applied to the whole image to derive a comparable surface reflectance as measured in the field. The method is reliant on *in situ* measurements, which are often unavailable.

An alternate approach for absolute atmospheric correction is the Dark Object Subtraction (DOS) method. DOS methods do not require *in situ* measurements nor information about the atmospheric conditions. It makes use of the information from the scene itself to calculate the path radiance (L_P) and the downwelling diffuse irradiance (E_d). This can be done for each specific band using a dark object within the scene that has low reflectance (Clark *et al*., 2010). These variables can then be used to calculate the reflectance factor for each pixel in the scene.

A widely used approach for hyperspectral data is the look-up table method (Liang *et al*., 2001). The approach makes use of pre-calculated tables of atmospheric radiative transfer to determine path radiance and at sensor radiance. Two look-up table based atmospheric correction algorithms have been used extensively with Hyperion data: Fast Line-of-sight Atmospheric Analysis of Spectral Hypercubes (FLAASH), and ATmospheric CORrection (ATCOR). Both are based on the Air Force Research Laboratory/Geophysics Directorate moderate spectral resolution background radiance and transmittance model, MODTRAN (Berk *et al*., 1998). MODTRAN models the scattering and transmission in the atmosphere to calculate the difference between at sensor radiance and at ground radiance. FLAASH works within ENVI (ITT VIS) utilizing MODTRAN 4 and is developed by Spectral Sciences Inc, under the sponsorship of The Air Force Research Laboratory (ENVI, 2009). ATCOR is developed by ReSe Applications and makes use of a newer MODTRAN 5 model than its competing products. ATCOR is available as a stand-alone client running in an IDL Virtual Machine (ITT VIS), as well as an add-on to either Geomatica (PCI) or ERDAS (Intergraph). ATCOR comes in a number of different versions, ATCOR 2 for flat surfaces, ATCOR 3 for rugged terrain, and ATCOR 4 for airborne sensors (Richter and Schläpfer, 2011).

The ATCOR and FLAASH algorithms share a number of input requirements, solar conditions (elevation, azimuth) or scene location and imaging time, sensor location (zenith, azimuth), aerosol model (rural, urban, marine, etc…), sensor type, scene elevation etc. (ENVI, 2009; Richter and Schläpfer, 2011). Water vapor conditions are automatically calculated based on atmospheric water absorption feature at around 1130 nm, specifically 1130 nm for ATCOR and 1135 nm for FLAASH.

The most difficult part of atmospheric correction is eliminating the impact of atmospheric aerosols (Liang *et al*., 2001). Both ATCOR and FLAASH attempt to extract atmospheric aerosol levels using a ratio between the reflectance at 2000nm and 500nm in dark pixels identified by Kaufman et. al. (2007) (KT method). Implementation in FLAASH uses a ratio of 0.45, while ATCOR uses 0.5 as suggested by Kaufman et. al. (2007). By iterating the MODTRAN calculations with visibilities ranging from 17 to 200 km in FLAASH and 5 to 80 km in ATCOR, the best match to the ratio determines the aerosol level. In addition ATCOR reiterates the MODTRAN calculation with lower estimates of aerosol if reflectance in the red (for vegetation) or NIR (for water) bands become negative. In addition to automatic aerosol retrieval, estimates can be entered manually by giving an estimate of visibility in kilometers. Surface visibility has an exponential relationship with aerosol optical thickness, which is representative of the amount of aerosols in the atmosphere (NASA, 2012). Either direct measurements of surface visibility can be used for the manual input or measurements from sun photometers. A sun photometer can directly measure the aerosol optical depth at different wavelengths. NASA operates the international AErosol RObotic NETwork (AERONET), which is a network of CIMEL Electronique 318A sun and sky spectral sun photometers (NASA, 2007).

2.3. Red edge inflection point

The red edge is the abrupt change in reflectance between 680 and 740 nm seen in vegetation spectra. The steep increase in reflectance in this region is the transition between the chlorophyll absorption zone in the visible part of the spectrum and the NIR infrared plateau of high reflectivity (Herrman *et al*., 2010).

The visible region impacts the red edge through chlorophyll absorption features, which peak around 430 nm and 660 nm for chlorophyll A and 435 nm and 625 nm for chlorophyll B (PhotochemCAD absorption database, Du *et al*., 1998). The peaks at 430 nm and 435 nm are also impacted by the absorption from liquid water, α-carotene, and lutein

(xanthophyll). Only chlorophyll shows strong absorption features around 625 nm and 660 nm (Gates *et al*., 1965). As chlorophyll content increases, its absorption feature becomes broader, moving the red edge towards longer wavelengths. The red edge has been shown to strongly correlate with chlorophyll content in vegetation (Gates *et al*., 1965; Filella and Peñuelas, 1994; Zhang *et al*., 2007; Kodani *et al*., 2001).

The NIR region of the spectrum for vegetation has a plateau of high reflectivity that is mainly affected by plant cell structure and leaf layers (Herrmann *et al*., 2010). As the amount of vegetation and leaf layers increases, the reflectance in the NIR increases. This would also move the red edge towards longer wavelengths. The red edge also shows a strong correlation with LAI, an indicator of biomass levels (Filella and Peñuelas, 1994; Kodani *et al*., 2001; Pu *et al*., 2003; Herrmann *et al*., 2010).

The red edge is impacted by at least two factors; chlorophyll in the visible and leaf layers and structure in the NIR, which can be indicated by LAI. The increase of either chlorophyll or leaf biomass would shift the red edge towards a longer wavelength. Both chlorophyll and LAI show strong seasonal trends in broadleaf forests, with strong growth in the spring, a stable period in the summer, and finally a rapid decrease in the autumn (Kodani *et al*., 2001; Rautiainen *et al*., 2009; Rautiainen *et al*., 2011). With coniferous forests the trend in LAI and chlorophyll at a canopy level is less distinct. While not as strong as the trend with broadleaved forests, Rautiainen *et al*. (2011) showed a seasonal dynamic in Finnish boreal coniferous canopy-level LAI, with an increase in the spring, peaking in the summer, and decreasing in the autumn. Only the xeric pine site effectively showed no seasonal change in LAI. For chlorophyll the seasonal dynamics are more complex as identified by and Silkina and Vinokurova (2008). First year P. abies needles show a decreasing trend in chlorophyll a concentration (mg/needle) from May onwards, while chlorophyll B concentration mg/needle shows a slight increase from August to September (Silkina and Vinokurova, 2008). Overall however, chlorophyll content for first P. abies year needles (mg/needle) does show a seasonal trend for both chlorophyll A and B, with chlorophyll A peaking in mid-September and chlorophyll B in late September. Canopy scale chlorophyll is hard to estimate, and the seasonal dynamics of coniferous chlorophyll content at a canopy scale is unclear.

The red edge inflection point (REIP) is simply the point of inflection in the red edge and has been extensively used as an indicator of red edge position (Danson and Plummer, 1995; Dawson and Curran, 1998; Bonhan-Carter, 1988; Guyot *et al*., 1992; Jago *et al*., 1999;

Li *et al*., 1993; Pu *et al*., 2003). The red edge position has been shown to be correlated with LAI and chlorophyll content, specifically Guyot *et al*. (1992, p. 160) determine that the "most important factors [influencing the REIP] are the leaf chlorophyll content and the LAI". Thus, the seasonal trends of the REIP should closely follow those of LAI and chlorophyll content.

The correlations between REIP and biophysical forest parameters have however been questioned. According to Darvishzadeh *et al*. (2009), in laboratory conditions while narrowband vegetation indices show reasonable correlation with LAI, the REIP does not. There is also concern about the basic assumptions about the red edge itself. Filella and Peñuelas (1994) identify that in the first derivative curves of the red edge of vegetation two distinct peaks can be seen, with the longer wavelength peak becoming higher in intensity as the growing season advances. In addition to LAI and chlorophyll, the red edge may be impacted by other biophysical parameters, like nitrogen content (Cho and Skidmore, 2006).

The high spectral resolution Hyperion data provides an opportunity to calculate the REIP from large areas. As previous studies have pointed out the good correlation of REIP and LAI, REIP may provide an opportunity to estimate the LAI in boreal forests for large areas. While multispectral satellite imagery has been extensively used for LAI estimation, it suffers from saturation at low LAI levels, which has limited its applicability in dense coniferous forests (Mutanga and Skidmore, 2004).

The REIP is the most widely used parameter from the red edge, however other parameters have been suggested, or have correlated with biophysical parameters (Liang, 2004). Li *et al*. (1993) suggest that the second derivative from two narrow windows, 690 nm and 740 nm, can be used for LAI estimation despite varied soil conditions. Pu *et al*. (2003) suggest the red well position, which is the wavelength of minimum reflectance in the red region of a vegetation spectrum. Filella and Peñuelas (1994) suggest the area of the red edge peak, which is the sum of the derivatives between 680 nm and 780 nm. The area of the red edge peak was correlated with LAI "because LAI determines the ratio between near-infrared and red reflectances" (Filella and Peñuelas, 1994, p. 1469). The REIP is however the best established of the red edge parameters. The REIP has been extensively studied using a range of spectra including: modelled (Guyot *et al*. 1992), laboratory measured (Darvishzadeh *et al*., 2009), *in situ* field (Filella and Peñuelas, 1994), airborne (Schlerf *et al*., 2005), and satellite (Pu *et al*., 2003).

2.4. Red edge inflection point calculation

While the REIP can simply be defined as the wavelength in the red edge where the slope is steepest, the sensitivity and calculation method for the REIP varies with the spectral resolution of the data. Working with high resolution Hyperion data and very high resolution *in situ* data presents us with a number of different methods for calculating the REIP, which produce different results. With a nominal resolution of 10 nm with Hyperion data, we have thirteen reflectance values in the region of the red edge (661-783 nm). While with an interpolated spectral resolution of 1nm (from a sampling interval of 1.5 nm and a FWHM of 3.5 nm) we have 123 reflectance values with our *in situ* data (Hatchell, 1999).

While the different methods of calculating the REIP produce different results, they also rely on different assumptions about the REIP. By comparing the results of the different methods of calculating the REIP we can question the assumptions the methods are based on.

A review of the literature has identified five basic methods for calculating the REIP with both high resolution and very high resolution spectral data; maximum first derivative (Dawson and Curran, 1998), four-point interpolation (Pu *et al*., 2003), Lagrangian interpolation (Dawson and Curran, 1998), fifth-order polynomial fitting (Pu *et al*., 2003), and inverted-Gaussian modeling (Bonhan-Carter, 1988).

1) Maximum first derivative:

The maximum first derivative is the simplest approach for REIP calculation. The method determines the first derivative of stand reflectance in between measured wavelengths directly using the measured reflectance. The REIP is then the wavelength corresponding to the highest derivative value in the red edge.

$$D_{\lambda(i)} = (R_{\lambda(j+1)} - R_{\lambda(j)})/(\lambda_{(j+1)} - \lambda_{(j)})$$

Where: $D =$ Derivative, $R =$ Reflectance, $\lambda =$ Wavelength and $i = (j + (j + 1))/2$.

The method is based on the definition of the REIP; it is located where the rate of change within the red edge is highest, the maximum first derivative. The derivative values are calculated for points between measured wavelengths.

2) Four-point linear interpolation:

The four-point linear interpolation is based on observations made by Guyot and Baret (1988) on the properties of the red edge. As Figure 5 shows, the spectral reflectance at the REIP can be calculated as being halfway between the reflectance at 670 nm (red) and 780 nm (NIR). While the red edge itself can be approximated as a straight line between 700 and 740 nm.

Thus the REIP can be calculated after Pu *et al*. (2003) by first determining the reflectance at the REIP:

$$R_i = (R_1 + R_4)/\,2$$

Calculating where on the straight line between 700 and 740 nm this reflectance is found:

$$REIP\ (\lambda) = \lambda_2 + \ (\lambda_3 - \ \lambda_2)\ \frac{R_i - \ R_2}{R_3 - \ R_2}$$

$$\lambda_1 = 670 \text{ nm},\ \lambda_2 = 700 \text{ nm},\ \lambda_3 = 740 \text{ nm},\ \lambda_4 = 780 \text{ nm}$$

Where: $R =$ Reflectance, and $\lambda =$ Wavelength.

The benefit of the method is that only four reflectance values are needed to calculate the REIP. The assumption of a linear red edge is a questionable one. There is an assumption that the only impacting factor in the red edge is the reflectance at red and NIR wavelengths and no significant absorption or reflectance features are located between 700 and 740 nm.

3) Lagrangian interpolation:

The Lagrangian interpolation technique is similar to the direct first derivative approach, but instead of making use of a single measurement it takes into account the highest first derivative value and the ones directly preceding and following it (Dawson and Curran, 1998). Using these three derivative values a three-point Lagrangian interpolation is performed

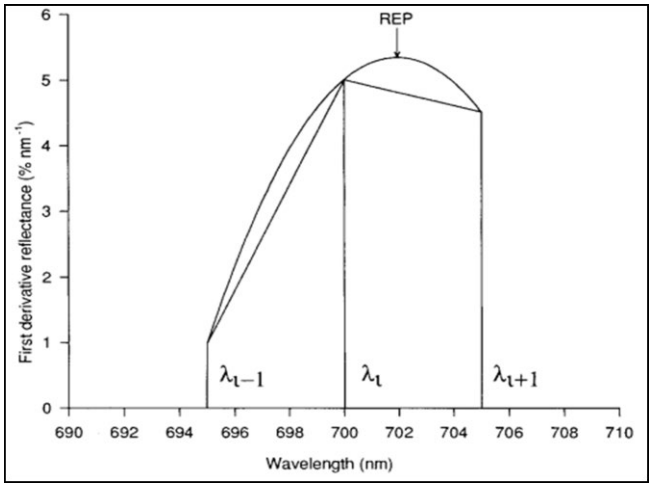

Figure 6. Lagrangian interpolation technique to determine the red edge inflection point wavelength. λ_i is the the maximum first derivative wavelength. (Dawson and Curran, 1998, Figure

(Jeffrey, 1985). The Lagrangian interpolation is a second-order polynomial fitting procedure. The benefit applying a Lagrangian interpolation to the first derivative values over other forms of interpolation techniques is the low computational requirements of the Lagrangian interpolation. In addition, the Lagrangian technique does not require the known derivative values to be equally spaced apart.

While based on the same assumptions of the REIP as the first derivative method, the Lagrangian technique provides an added range to the possible REIP values. As shown in Figure 6 instead of being limited to the spectral resolution of the data, the REIP can be calculated to wavelengths in between the derivative values. This is particularly valuable for our high resolution Hyperion data, allowing us a greater sensitivity in the REIP than the 10nm provided by the first derivative method. The Lagrangian technique is of limited use for the very high resolution *in situ* data if a sub one nm improvement in sensitivity is not needed.

$$REIP = \frac{\mathrm{A}(\lambda_i + \lambda_{i+1}) + B(\lambda_{i-1} + \lambda_{i+1}) + C(\lambda_{i-1} + \lambda_i)}{2(\mathrm{A} + \mathrm{B} + \mathrm{C})}$$

$$A = \frac{D_{\lambda(i-1)}}{(\lambda_{i-1} - \lambda_i)\,(\lambda_{i-1} - \lambda_{i+1})}$$

$$B = \frac{D_{\lambda(i)}}{(\lambda_i - \lambda_{i-1})\,(\lambda_i - \lambda_{i+1})}$$

$$C = \frac{D_{\lambda(i+1)}}{(\lambda_{i+1} - \lambda_{i-1})\,(\lambda_{i+1} - \lambda_i)}$$

Where: $D = \mathrm{Derivative}$, $R = \mathrm{Reflectance}$, and $\lambda = \mathrm{Wavelength}$.

4) Fifth-order polynomial fitting:

$$p = a_0 + \sum_{i=1}^{5} \mathrm{a_i}\lambda^{\mathrm{i}}$$

The fifth-order polynomial fitting method as described by Pu *et al*. (2003) suggests that the red edge can be modeled by fitting a fifth-order polynomial to the reflectance values in between the minimum reflectance in red and the maximum reflectance in the NIR; 661 to 783 nm. A fifth-order polynomial was chosen for the high R^2 values, with over 0.99 being achieved for all plots.

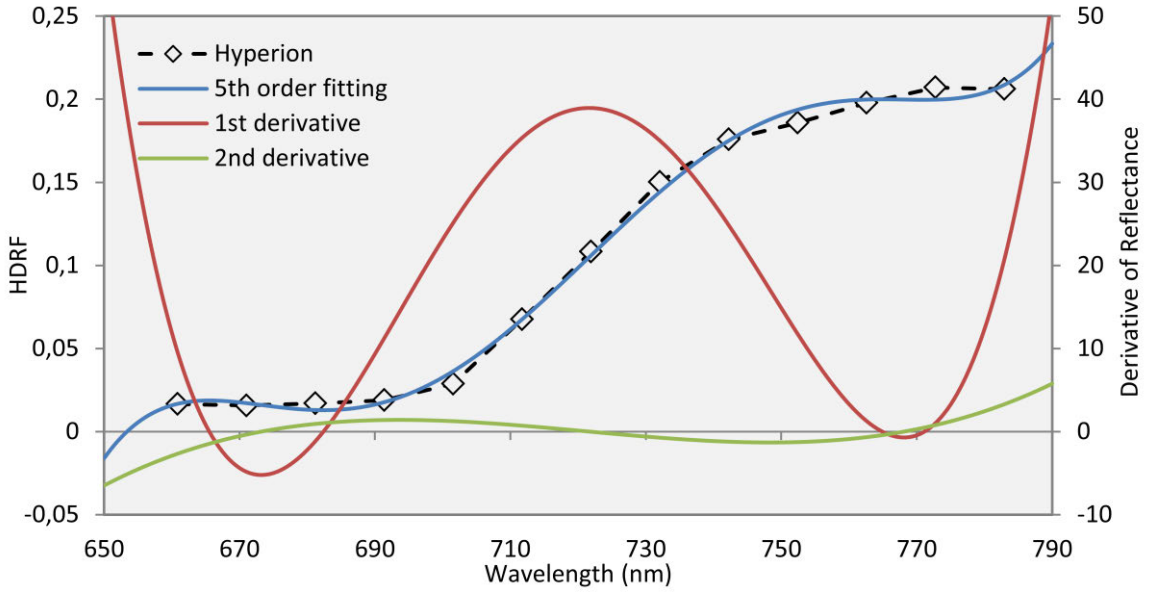

Figure 7. Fifth-order polynomial fitted to a sample Hyperion forest spectra with first and second derivatives.

Once the fifth-order polynomial is fitted the middle root of the second derivative signifies the REIP. Polynomial fitting allows for the direct calculation of the REIP directly using its definition as the point where the slope is highest. The polynomial method is not limited by the resolution of the data used in this study. It however requires enough points within the red edge for an accurate polynomial to be able to be fitted. The spectral resolution of Hyperion does not limit the calculation of REIP.

5) Inverted-Gaussian Modeling:

According to Bonham and Carter (1988) the shape of the spectral reflectance of the red edge in vegetation canopies can be approximated by one half of an inverted Gaussian function. This is due to the consistent low reflectance of vegetation in red, followed by a sharp change and reaching a plateau in the near infrared. The assumption of an inverted Gaussian red edge shape is based solely on the fit seen in laboratory and airborne vegetation spectra, rather than any theoretical basis.

3. DATA

3.1. Study area

The study area of Hyytiälä is located in Southern Finland (61° 51'N, 24°17'E) (Figure 8). The area is a typical example of a boreal coniferous forest that covers about 8% of the Earth's surface and stores about 10% of the total terrestrial ecosystem carbon (Hari and Kulmala, 2005). The dominant tree species in the area are Norway spruce (*Picea abies*), Scots pine (*Pinus sylvestris*), and Silver birch (*Betula pendula*). The understory vegetation is composed of two layers: an upper understory layer (low dwarf shrubs or seedlings, graminoids, herbaceous species) and a ground layer (mosses, lichens). The area witnesses a strong seasonal pattern, with the growing season typically beginning in early May and senescence in late August. The area has an annual mean temperature of 3°C and precipitation of 700 mm.

Figure 8. Location of the Hyytiälä study site within Southern Finland (61° 51'N, 24° 17' E).

3.2. Atmospheric data

The Hyytiälä study site is part of the AERONET program, established by NASA and LOA-PHOTONS, which is a federation of group-based aerosol monitoring networks (NASA, 2007). Hyytiälä is thus home to a CIMEL Electronique 318A spectral radiometer, also known as a sun photometer (NASA, 2007). A sun photometer is used to measure spectral aerosol optical depth (AOD) and the amount of water in the atmosphere. The AOD data is provided at three processing levels: level 1.0 (unscreened), level 1.5 (cloud-screened), and level 2.0 (cloud screened and quality-assured). AERONET generally provides AOD measurements at 1020nm, 870nm, 675nm, 500nm, 440nm, 380nm and 340nm. In addition, a number of Angstrom exponents are provided, which can be used to estimate visibility from aerosol levels (NASA, 2009B).

The SMEAR II (Station for Measuring Forest Ecosystem - Atmosphere Relations) tower located in Hyytiälä, contains a Vaisala FD12P weather sensor. The Vaisala sensor is capable of optically measuring visibility from 10 to 50000 m. The stated accuracy by the manufacturer is +-10% from 10 to 10000m and +-20% from 10000 to 50000 m (Vaisala,

Table 2. Hyperion scene details

Image id	Date	Day of Year	Cloud cover %	Solar elevation	Look Angle	Solar azimuth
EO1H1890172010125110KA_SGS_01	2010/05/05	125	20 to 29	43.34	-0.5064	161.51
EO1H1890172010153110KC_WPS_01	2010/06/02	153	0 to 9	48.49	-14.838	154.71
EO1H1890172010161110KB_SGS_01	2010/06/10	161	30 to 39	49.69	-5.0688	157.36
EO1H1890172010184110KC_SGS_01	2010/07/03	184	0 to 9	49.01	-13.752	152.73
EO1H1890172010192110KA_SGS_01	2010/07/11	192	10 to 19	48.58	-3.896	155.94

2002). While the instrument measures every minute, the data is averaged over 30 minutes. The sensor is located at a height of 17 m.

3.3. Hyperion images

Five Hyperion images were chosen for processing, provided courtesy of the USGS. The images were chosen based on the low cloud cover over the study site. Two of the images had cloud cover of over 20%, however the cloud cover was mainly in the northern and southern parts of the image and not over the actual study site. EO-1 follows the World Reference System-2 path and row system, with a 16 day nadir repeat cycle. It can also vary its look angle from nadir, capable of a variation of 19.976 degrees in either direction (Figure 9). A negative look angle means that the satellite passed the east of the study site, which is the case for all of the scenes chosen in this study (USGS, 2010b). All of the scenes in this study were 42 km in length. The scenes were centered on the study site, however as Hyperion only captures a swath width of 7.5 km one of the forest field sites was only imaged on two of the dates (U10 pine site, Table 3), falling beyond the eastern extent of the images on the three other dates. The Hyperion data is available in two formats; L1GST and L1R. The main difference between the two is the file format: L1GST in GeoTiff and L1R in HDF. The L1GST product is also georeferenced using the satellite coordinates at the time of capture.

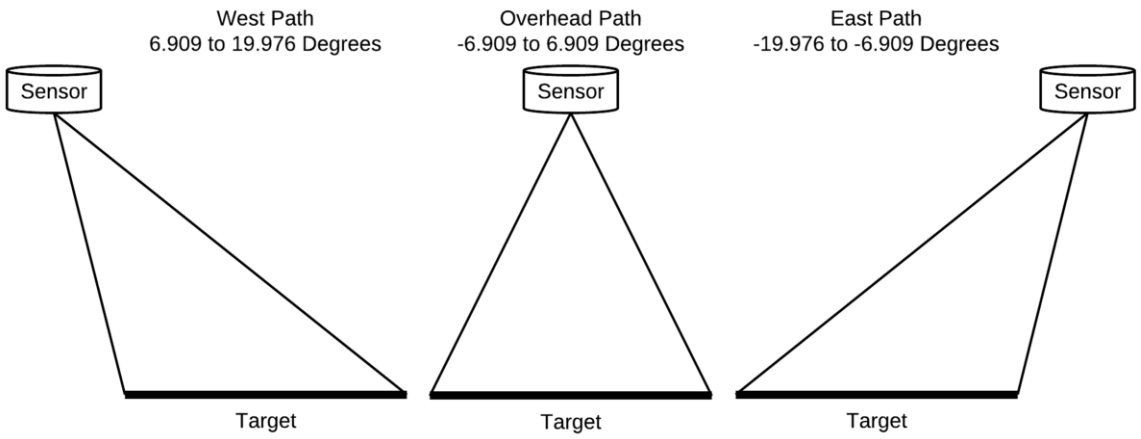

Figure 9. Hyperion look angle and satellite path. All scenens used in this study were taken from an east or overhead path with a negative look angle.

3.4. MODIS products

MODIS is an instrument aboard the both the NASA Terra and Aqua satellites. The two satellites are in sun-synchronous, near-polar orbits at 705 km. Aqua is in an ascending node, crossing the equator at 13:30, while Terra is in a descending node crossing the equator at 10:30. The instrument consists of 36 bands in total, covering various spectral ranges from as low as 405 nm to a maximum of 14385 nm. The bands have a range of spatial resolutions, from 250 m up to 1000 m (NASA, n.d.).

In this study two MODIS science products were used: Vegetation Indices 16-Day L3 Global 250m (MOD13Q1) and Nadir BRDF-Adjusted Reflectance 16-Day L3 Global 500m (MCD43A4). The MODIS science products provide reflectance measurements at a moderate spatial resolution, but have a very high temporal resolution with less than one day revisit times between the two satellites. An advantage of the MODIS products are that they have been extensively used and are rigorously validated (Gao *et al*., 2003; Huete *et al*., 2002). The MODIS products used were provided in a Sinusoidal Grid (SIN) projection with standard tiles representing 10 degree by 10 degree (2400 by 2400 pixels) on the ground (Schaaf, 2010).

Both of the used products use the MODIS MOD09 product. The MOD09 product is an atmospherically corrected daily surface reflectance product, processed to yield an estimate of surface reflectance, as it would be measured at ground level (Vermote, *et al*., 2011). The product is atmospherically corrected using the 6S radiative transfer code (Vermote *et al*., 1997). Input estimates for atmospheric conditions, aerosols, water vapor, ozone, clouds are retrieved from other MODIS products. In addition ancillary products, digital elevation model and atmospheric pressure are inputted into the atmospheric correction. The processing steps also attempt to correct for reflectance from adjacent pixels and Bidirectional Reflectance Distribution Function (BRDF). A full overview of the MOD09 processing steps is found in Vermote and Vermeulen (2009).

The MOD13 product is used to produce vegetation indices; Normalized Difference Vegetation Index (NDVI) and Enhanced Vegetation Index (EVI). The product is also provided with direct reflectance values for the red and NIR wavelengths. The Q1 product used in this study is a 16 day composite at a 250 m spatial resolution. The product uses the best scenes captured within a 16 day period to produce a single reflectance value for each MODIS pixel. After 16 days of observations a composite is created with each pixel produced separately. Scenes with cloud cover, off-nadir capture, and heavy atmospheric interception are

filtered out. For the remaining pixels; if 2 or more pixels are available, a Constrained View Angle - Maximum Value Composite (CV-MVC) is used to produce the final value for each pixel. The CV-MVC looks at the two highest values and uses the one that was captured closest to a nadir viewing angle. If only one measurement is available then it is used, and if no values are available a fill value is used based on a historic average (Strahler, *et al*., 1999).

MCD43 is a combination product that combines information from the MODIS Terra and Aqua sensors. The product combines the satellite observations with a BRDF model to calculate a set of parameters that describes the BRDF of the surface. The parameters can then be used to calculate the surface albedo at specific bands (Schaaf, 2010). The A4 product used in this study is a nadir adjusted reflectance factor. The product simulates the surface reflectance as if it was measured from nadir (Strahler, *et al*., 1999). The product has a spatial resolution of 500m and a temporal resolution of 8 days, from 16 days of observations (Schaaf, 2010).

3.5. Field spectroscopy measurements

In situ field spectroscopy measurements were made from both a grass field site and a number of forest sites. The field spectroscopy was conducted using a FieldSpec Hand-Held UV/VNIR (325–1075 nm) Spectroradiometer manufactured by Analytical Spectral Devices (ASD). The forest measurements were conducted under diffuse lighting conditions (either under full cloud cover or at low solar elevation) to determine understory reflectance. A full account of the understory measurements can be found in Rautiainen *et al*. (2011). Measurements of the grass field were done with low cloud cover and high solar elevation, similar to conditions at satellite overpass. All measurements were done with a transect approach, with 28 m long transects and measurements roughly every meter. White references were taken every third measurement and at the beginning and end of each transect using a white Spectralon panel. The understory measurements were done on permanent transects, marked out in the field. The grass field transect was not permanent however, the grass field was assumed to be homogeneous. The forest stands represent the different species compositions typical to the boreal coniferous forest zone in Finland, covering the main tree species and understory types, excluding bogs (Table 3). Two pine sites were chosen due to the different understory types they represent.

The field spectroscopy measurements were processed to corresponding Hemispherical-Directional Reflectance Factors (HDRF). The Spectralon measurements from before and after three measurements were linearly interpolated to gain a spectral irradiance value for the time of each reflectance measurement. The Spectralon panel was assumed to be a 100% reflecting perfectly Lambertian surface (Labsphere, n.d.).

3.6. Canopy leaf area index

Tree-level LAI was measured from the same forest sites. LAI is defined as hemi-surface area of leaves per unit horizontal ground area (Chen and Black, 1992). Measurements of LAI were made using two LAI-2000 Plant Canopy Analyzer instruments: one above the canopy and one below. The sampling scheme was a 'VALERI-cross' (Validation of Land European Remote Sensing Instruments, http://w3.avignon.inra.fr/valeri/) which consists of two perpendicular 6-point transects. The distance between two measurement points was four meters, so that the sampling scheme corresponded roughly to a 20m x 20m plot. The measurement height was 0.7 meters for below canopy measurements. Measurements were done approximately every two to three weeks; dependent on weather conditions.

The LAI-2000 Plant Canopy Analyzer makes a number of assumptions to calculate LAI. One of them being that: "the foliage is randomly distributed" (LI-COR, 1992, p.2-3). With coniferous forests it has been shown that the distribution is not completely random, while shoots are randomly distributed the actual needles are 'clumped' around the shoots (Stenberg, 1994). This causes an underestimation of LAI in coniferous stands, the measured LAI is thus often referred to as effective LAI rather than true LAI (Stenberg *et al*., 1994; Chen *et al*., 1997).

Table 3. Forest field plots

Study site	Site id	Upper understory layer			Ground layer	Dominant tree species	Mean tree height, m	Mean diameter at breast height, cm
		Dwarf shrubs	Pteridophytes+herbaceous	Graminoids	Mosses/Lichens			
Xeric	U10	Vaccinium vitis-idaea, Calluna vulgaris, Empetrum nigrum			Pleurozium schreberi, Dicranum spp. / Cladina arbuscula, Cladina rangiferina	Scots pine (*Pinus sylvestris*)	16.6	18.6
Sub-xeric	U18	Vaccinium myrtillus, Vaccinium vitis-idaea	Luzula pilosa, Maianthenum bifolium, Oxalis acetosella, Trientalis europaea, Dryopteris carthusiana	Deschampsia flexuosa	Pleurozium schreberi, Dicranum spp.	Scots pine (*Pinus sylvestris*)	16.5	24.3
Mesic	U26	Vaccinium myrtillus, Vaccinium vitis-idaea, Linnea borealis	Luzula pilosa, Maianthenum bifolium, Epilobium angustifolium, Dryopteris carthusiana	Deschampsia flexuosa	Pleurozium schreberi, Dicranum spp. Hylocomium splendens	Norway spruce (*Picea abies*)	16.8	17.8
Herb-rich	H3	Vaccinium myrtillus, Vaccinium vitis-idaea	Trientalis europaea, Maianthenum bifolium, Rubus saxatilis, Dryopteris expansa, Melampyrum sylvaticum, Oxalis acetosella	Deschampsia flexuosa, Calamagrostis spp.	Pleurozium schreberi	Silver birch (*Betula pendula*)	14.9	12.2

4. METHODS

4.1. Hyperion processing

The processing of Hyperion data largely follows the method and sequence outlined by Goodenough *et al*. (2003). The processing covers two-step destriping, desmiling, atmospheric correction, and geocorrection (Figure 10). The L1R file format was used for processing; the ungeocorrected data is beneficial for destriping due to the along-track nature of the striping. All five of the Hyperion scenes were atmospherically corrected using both FLAASH and ATCOR 2. The images were initially subset to 198 bands, with all of the uncalibrated bands being removed from further processing. ATCOR requires bands to be sequential in wavelength, thus bands 77 and 78 were removed from ATCOR processing. ATCOR 2 was chosen over ATCOR 3 due to the study flat topography in the area.

No spatial shift correction was performed; the processing done in the initial Level 1B processing was felt to be sufficient. An improvement of under a pixel in spatial accuracy, with a reduction of spectral accuracy due to resampling, would not be beneficial for this study.

Destriping was done using a two-step process using a combination of SpecMM and

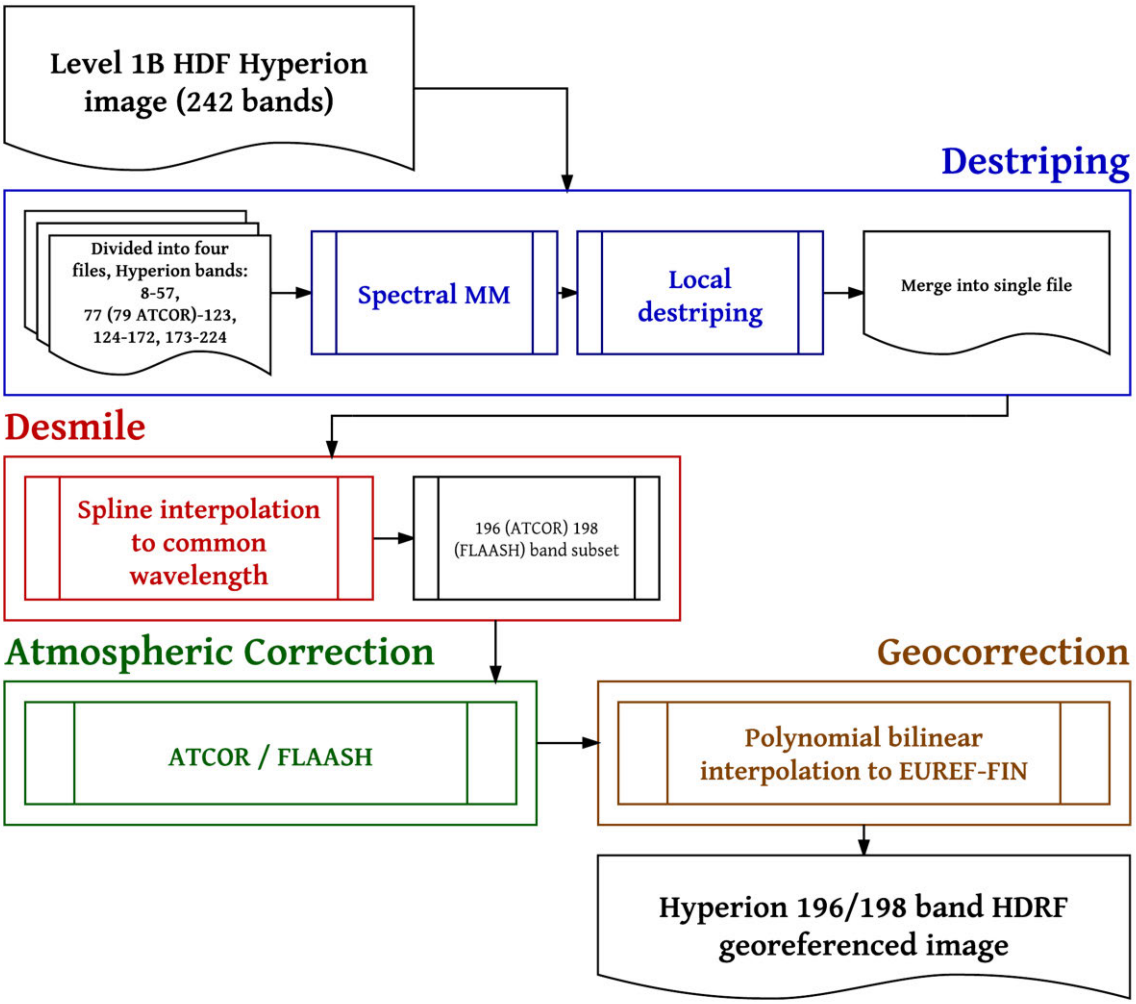

Figure 10. Hyperion pre-processing steps, largely following Goodenough et al. (2003). Destriping was done in four files due to computer memory limitations. ATCOR requires bands to be sequential in wavelength, thus the overlapping bands from the SWIR sensing array (bands 77 and 78) were removed.

local destriping. Both SpecMM and the local destriping were implemented in IDL (ITT VIS). The destriping was performed in four groups of bands due to computer memory limitations. The division of bands was done along heavy atmospheric absorption features, with the following groups processed together: bands 8-57, bands 77-123, bands 124-172, bands 173-224.

SpecMM was performed first. As the highly correlated bands used for correction are expected to be located near in wavelength to the band affected by striping, the splitting of the bands should not have heavily impacted the SpecMM process (Jimenez and Landgrebe, 1999). As the VNIR bands were processed in one group, the spatial shift between VNIR and SWIR did not impact the SpecMM process. As outlined by Sun *et al*. (2008) three parameters can be adjusted in the SpecMM process. First the window size for spatial smoothing, used in the selection of correlated bands, should be set to around the width of the evident stripes in pixels. This was set to 5 for all images based on a visual interpretation of the striping. Second the length of row segments used in determining the similarities between different bands, which should be set three to six times higher than the first parameter. This was set to 21 for all images. Third the number of highly correlated bands be used for the destriping, this should be between 15 and 30 for Hyperion, and was set to 20 for all images.

The local destriping was implemented as outlined by Goodenough *et al*. (2003), each band was looked at to detect if striping was still in evident after SpecMM. Each band was examined to see if the digital number (DN) value of the second pixel in each column (second pixel was used because of the spatial shift applied to the SWIR during level 1B processing) was lower than both the DN value of the pixel immediately to the left and right of the pixel. If so, the column was analyzed as a potential stripe. If a continuous segment of over five pixels with consistently lower DN values and over 50% of the overall pixels in the column were lower than the corresponding pixels in the two adjacent columns, the column was flagged as a stripe. Each pixel in the column was then replaced with the average value of the pixels in the spatially adjacent columns.

Due to the reinterpolation required by the desmiling process it is important to consider if it should be undertaken. While the methods for detecting smile clearly indicate its presence, its effect on the final reflectance values is difficult to judge. Overall a variation of 4 nm in wavelength, as seen in the pre-launch calibration measurements, may not be significant enough to justify a reinterpolation of the data (Filella and Peñuelas, 1994). Even a shift of a

few nanometers could however significantly impact the red edge, where there is a large change in reflectance.

Desmiling was done using the moving linear fitting method outlined in Goodenough *et al*. (2003). All columns in a band were reinterpolated to a common wavelength using the laboratory derived values. Instead of using a linear fitting for interpolating the bands to a common wavelength, a cubic spline interpolation was used. The desmiled images were compared to non-desmiled images to determine the impact of the smile on the final reflectance values, especially in the red edge.

The atmospheric correction process with ATCOR and FLAASH follows the two general steps outlined by Liang *et al*. (2001): parameter estimation followed by surface reflectance retrieval (Figure 11). The parameter estimation differs slightly between the two algorithms, with the atmospheric visibility estimation being a crucial part. The surface reflectance retrieval is performed with MODTRAN for both: MODTRAN 5 for ATCOR and MODTRAN 4 for FLAASH.

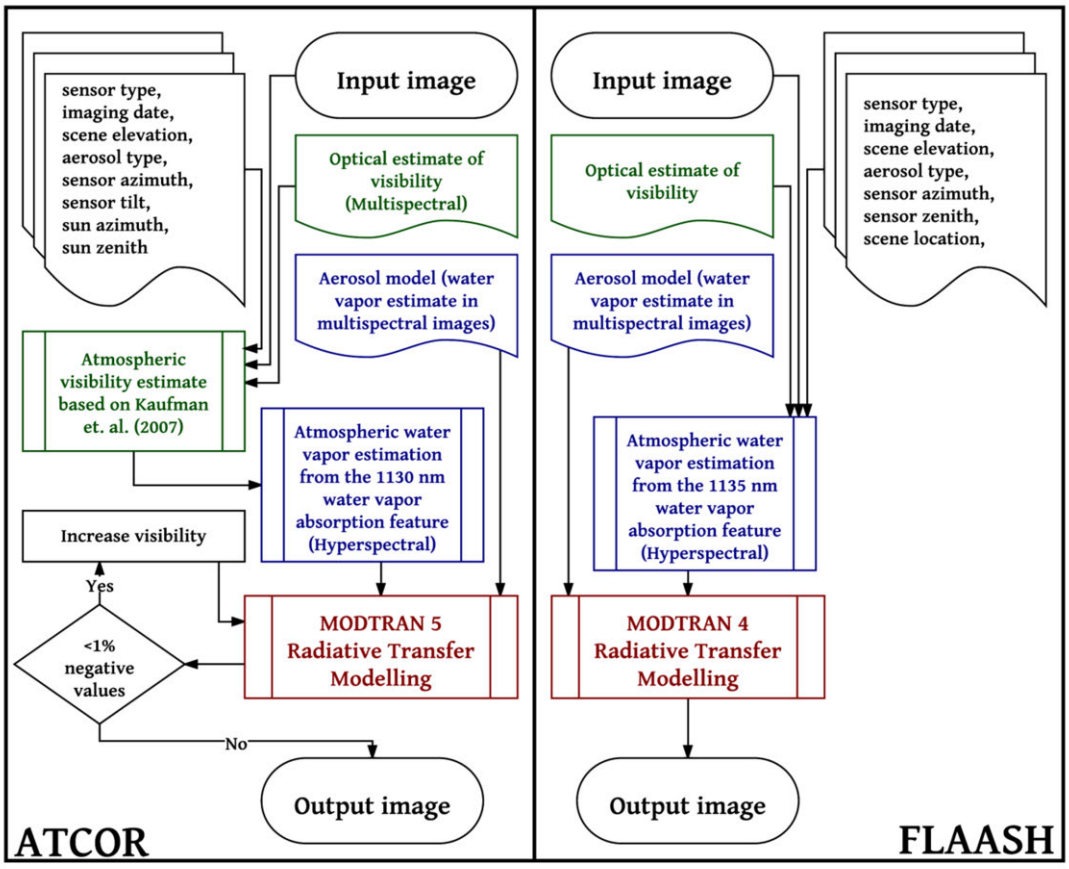

Figure 11. General overview of atmospheric correction steps with ATCOR and FLAASH used in this study. Both use MODTRAN for radiative transfer modeling. The main difference between the two algorithms is the retrieval of atmospheric aerosol levels.

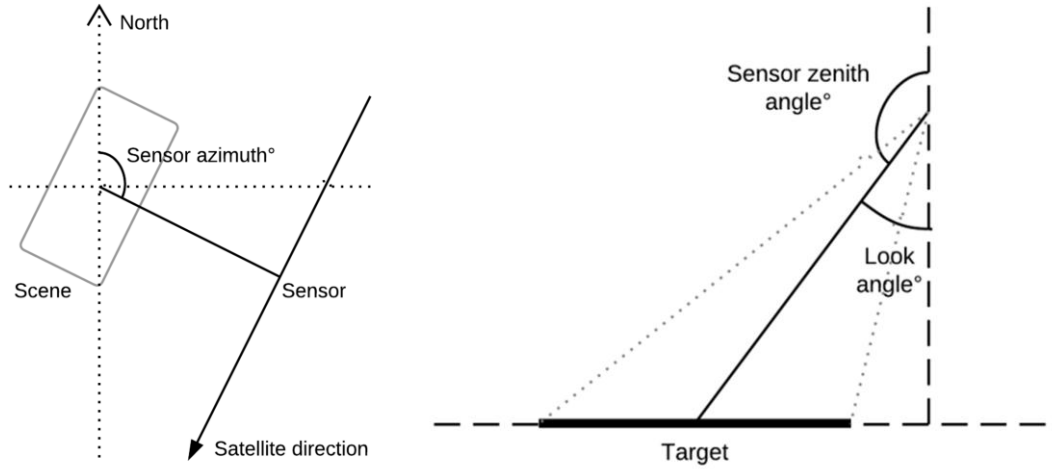

Figure 12. FLAASH sensor azimuth angle for scenens captured from a east path (left). FLAASH sensor zenith angle (right).

The FLAASH algorithm allows for the sensor look geometry to be taken into account. This is done with the input of the sensor zenith and azimuth angles. The zenith value is a positive number between 180 and 90 degrees with 180 representing a nadir look angle (Figure 12). This can be easily calculated from the Hyperion metadata:

$$FLAASH\ sensor\ zenith\ angle = 180° - absolute\ Hyperion\ look\ angle$$

The azimuth angle is the angle between the sensor look direction and north (Figure 12). The angle is between -180 degrees and 180 degrees. For Hyperion a negative look angle (sensor passed east of the scene) the FLAASH sensor azimuth angle is positive. As no satellite heading information is provided in the metadata the L1GST files were used to determine the satellite look angle. As the L1GST scenes are georeferenced using the satellite coordinates, the angle between the side of the L1GST scene and north can be measured. The sensor azimuth angle for Hyperion images with a negative look angle can then be calculated as:

$$FLAASH\ sensor\ azimuth\ angle = 90° + angle\ between\ side\ of\ scene\ and\ north$$

FLAASH processing three methods of atmospheric visibility estimation were identified: the KT method implemented in the algorithm, manual input from AOD data, and manual input from optical visibility data. AOD is defined as the integrated extinction coefficient over a vertical column of a unit cross section, by dividing the AOD at 550 nm by the thickness of the aerosol layer in the atmosphere an extinction coefficient can be estimated (NASA, 2007):

$$extinction\ coefficient = \frac{AOD\ 550\ nm}{thickness\ of\ the\ aerosol\ layer}$$

While AERONET does not directly provide the AOD at 550 nm, it can be calculated using the provided Angstom exponents and AOD at two other wavelengths (NASA, 2009B). The extinction coefficient can be used to calculate visibility using the Koschmieder equation (Horvath, 1971):

$$Visibility = \frac{3.912}{extinction\ coefficient}$$

A comparison of the visibility estimates shows a wide range of results (Table 4). The FLAASH KT method produces very low estimates of visibility. This was evident from heavily negative reflectance factors in vegetation spectra, the estimates of visibility themselves also seemed low for the weather conditions at the time of scene capture. The AOD method, while in theory should directly measure atmospheric aerosol levels, produced very inconsistent estimates of visibility (Table 4). Overall for the FLAASH algorithm the optical estimate of visibility produced the most consistent and realistic estimates of visibility. The optical estimates were limited by the 50 km upper limit of the sensor. Also the final scene (DOY 192) did not have a corresponding optical estimate, for this date a value of 50 km was used based on the very low AOD estimate on the day and high optical visibility measurements from days preceding and following scene capture.

A rural aerosol model was chosen for all scenes due to the location of the study site. Atmospheric water levels were automatically retrieved by the algorithm, with the atmospheric water model determined by latitude and date according to the FLAASH user guide (ENVI, 2009). Additionally, FLAASH has a number of advanced parameters that can be set. Aerosol scale height, which is used for adjacency scattering range, was set to 2 km as with the extinction coefficient calculations. Other levels were also tested, which produced less negative values over water features, but also produced significantly lower reflectance values in the NIR over dense forest areas. CO2 Mixing Ratio is suggested to be set at 20 ppm below actual levels, and was set at 410 ppm (ESRL, N.D.). A MODTRAN resolution of 1 cm was used, with 8 streams and using the scaled disort model.

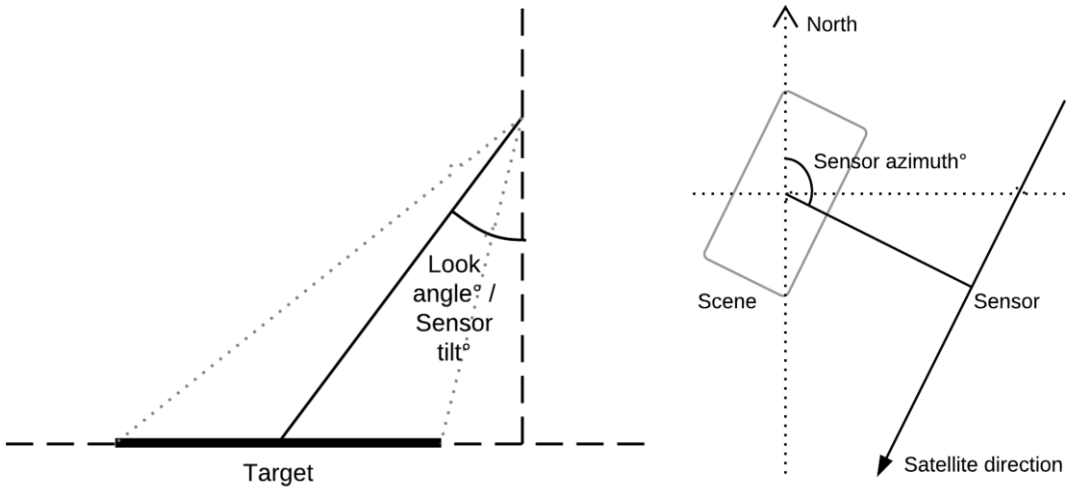

Figure 13 ATCOR sensor tilt angle (left). ATCOR sensor azimuthangle (right).

Like with FLAASH, the ATCOR algorithm can take into account sensor look geometry. This is done with the input of the sensor tilt and azimuth angles. The sensor tilt angle is a positive number with 0 representing a nadir look angle, and for Hyperion data it is directly the absolute look angle provided in the metadata (Figure 13):

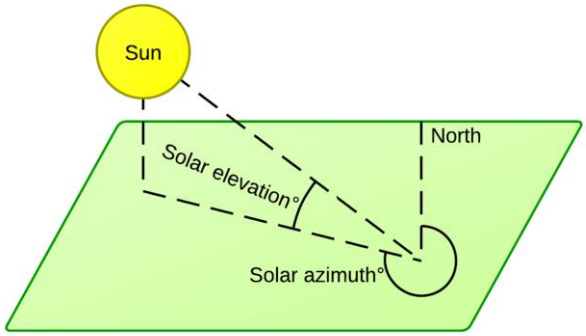

Figure 14. ATCOR required solar elevation and azimuth angles.

$$ATCOR\ sensor\ tilt\ angle = absolute\ Hyperion\ look\ angle$$

The azimuth angle is the angle between the sensor look direction and north (Figure 13). The angle is between 0 degrees and 360 degrees. For Hyperion scenes with a negative look angle (sensor passed east of the scene) the ATCOR sensor azimuth angle is calculated the same as the FLAASH sensor azimuth angle (see FLAASH):

Table 4. Visibility estimates in km. AOD: estimate from AERONET using aerosol optical depth and extinction coefficients. Optical: estimate from optical weather sensor. FLAASH KT: FLAASH algorithm KT method estimate. ATCOR KT: ATCOR algorithm KT method estimate. ATCOR final: Re-iterated final ATCOR algorithm estimate. No optical visibility estimate from DOY 192

DOY	AOD	Optical	FLAASH KT	ATCOR KT	ATCOR final
125	137.75	50.00	17.33	26.30	73.40
153	58.10	46.93	20.39	22.90	73.40
161	6.07	50.00	24.62	27.00	73.40
184	24.07	48.10	23.65	25.70	73.40
192	169.52		24.74	28.40	73.40

$$ATCOR\ sensor\ azimuth\ angle = 90° + angle\ between\ side\ of\ scene\ and\ north$$

Aerosol retrieval in ATCOR was done automatically by the algorithm. An initial estimate is made using the KT method; however the method resulted in negative reflectance values in the red and NIR wavelengths. The MODTRAN calculations are then reiterated by the algorithm, with higher estimates of visibility, until less than 1% of the pixels in red and NIR wavelengths are negative. The result was around an 80 km estimate for all scenes (Table 4). ATCOR uses the same MODTRAN settings as FLAASH, with 8 streams and scaled disort model. A rural aerosol model was used with atmospheric water levels determined automatically by the algorithm. The solar elevation and azimuth angles required for ATCOR were obtained from the Hyperion metadata (Table 2).

Geocorrection was performed with a second degree polynomial correction, with a vector base map from the national land survey of Finland used for reference (Maanmittauslaitos, MML). The area in question contains many roads and crossroads that provided a large number of potential ground control points. Around 20 control points were selected for each scene. The resampling was done to a 30m by 30m cell size using bilinear interpolation. Bilinear interpolation was chosen due to the improved geometric accuracy over nearest neighbor, while maintaining the spectral signature.

4.2. Validation of Hyperion atmospheric correction

4.2.1. Comparison against field spectroscopy measurements

To validate the atmospheric correction the satellite derived reflectance was compared with the in situ measured reflectance from the grass field in the area. Both the FLAASH and ATCOR corrected images were validated. The grass field is about 130 m by 60 m and can easily fit two Hyperion pixels (Figure 15). The Hyperion reflectance used was the mean of the two pixels. The aerial image seen in Figure 15 is taken late in the day when shadows start to come onto the field, at the time of Hyperion capture the field was shadow free. While the area is not optimal, due to the field being used for other purposes, including sports, the field is relatively homogeneous.

While no measurements directly coincided with the Hyperion images, the ground measured reflectance was interpolated to dates coinciding with the Hyperion scene capture; a double parabolic interpolation was used. The interpolation makes the assumption that the measurements on the ground represent the ground truth. After interpolation to Hyperion dates, the ground measured reflectance is binned into corresponding Hyperion bands using the spectral response of each band.

Figure 15. Overlay of two Hyperion pixels on the grass field

4.2.2. Comparison against MODIS products

A time series comparison was done between Hyperion and MODIS data for both FLAASH and ATCOR corrected images, and in comparison to both sets of MODIS data. The Hyperion images were projected into the MODIS SIN projection for the comparison. The comparison was done using the average of 27 MODIS pixels in the study area, with each pixel being about 500 m by 500 m on the ground. The pixel size was limited by the MODIS green band. The area covered by the pixels mainly covers forest. If a cell contained cloud shadow or cloud in the Hyperion image it was left out of the average. The Hyperion data was resampled to the MODIS spectral bands using the spectral response function of each band. The MODIS reflectance values were interpolated to Hyperion dates using a linear interpolation for the statistical analysis. Three bands are used for the comparison: green, red and NIR. The MOD13 product does not include the green band; only

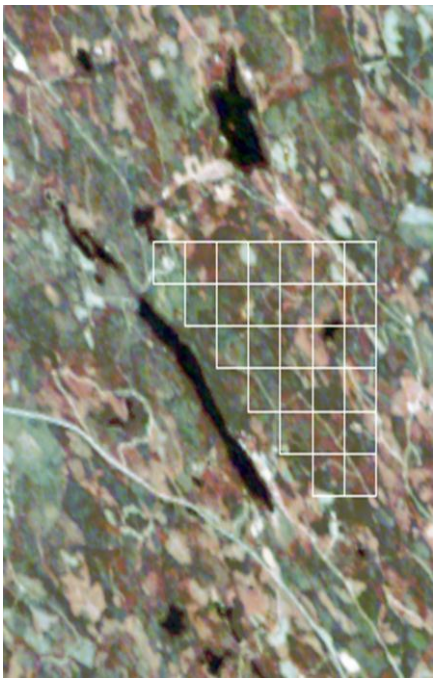

Figure 16. Overlay of MODIS pixels on a Hyperion scene in the MODIS SIN projection.

the MCD43 product was used for the comparison in green.

4.2.3. Statistical analyses

While comparison of reflectance data was performed with visual interpolation, two statistical "goodness-of-fit" measures were also calculated. Mean Deviation (MD) is a common measure of systematic deviation. Root Mean Square Deviation (RMSD) is commonly used as a measure for goodness-of-fit. Squaring the calculation causes more emphasis on data that does not fit well (Gao *et al*., 2003).

$$MD = \frac{\sum_{i=1}^{n} r1_i - r2_i}{n}$$

$$RMSD = \sqrt{\frac{\sum_{i=1}^{n} (r1_i - r2_i)^2}{n}}$$

r1 is the reflectance factor from the sensor being compared, in this study Hyperion. *r2* is the reference reflectance factor, in this study from either *in situ* field spectroscopy measurements or MODIS, *n* is the number of points. The statistical analysis was performed from reflectance factors, which have a range from 0 to 1.

4.3. Red edge inflection point

The REIP from *in situ* data was calculated using the maximum first derivative, four-point linear, and the fifth-order polynomial fitting methods. The Lagrangian interpolation method was left out because it would have provided at most a sub 1 nm improvement over the maximum first derivative method. For REIP calculation from Hyperion data, the Lagrangian interpolation, four-point linear and fifth-order polynomial fitting methods were used. Due to the complex implementation of the method and the poor results received in other studies the inverse Gaussian modeling approach was not implemented in this study (Pu *et al*., 2003). For both *in situ* and Hyperion fifth-order polynomial fitting, all reflectance values between 661 and 783 nm were used. Both the Hyperion and *in situ* data had high R^2 values ($R^2 > 0.99$), signifying a good fit.

The Lagrangian interpolation method of REIP retrieval requires the calculation of the first derivative of the red edge. These calculations were also used to look into the dynamics of the Hyperion red edge.

5. RESULTS AND DISCUSSION

5.1. Hyperion processing

Figure 17 shows that the main destriping with SpecMM produces a considerable reduction in the appearance of striping in the image. The impact of the subsequent local destriping is less apparent, but can be seen in the first and 114th column of the image; the first column was missing data in bands 8-35, while the 114th column showed consistently lower DN values over most of the VNIR bands.

The drawbacks of the SpecMM process, the inability to correct striping found in subsequent bands, is supplemented with the application of the local destriping (Sun *et al*., 2008). The process is optimal for Hyperion data due to the nature of the striping. The main striping, which is band specific, is corrected with the SpecMM process. The less common completely missing lines, which can be band sequential, are corrected with the local destriping (Goodenough *et al.,* 2003).

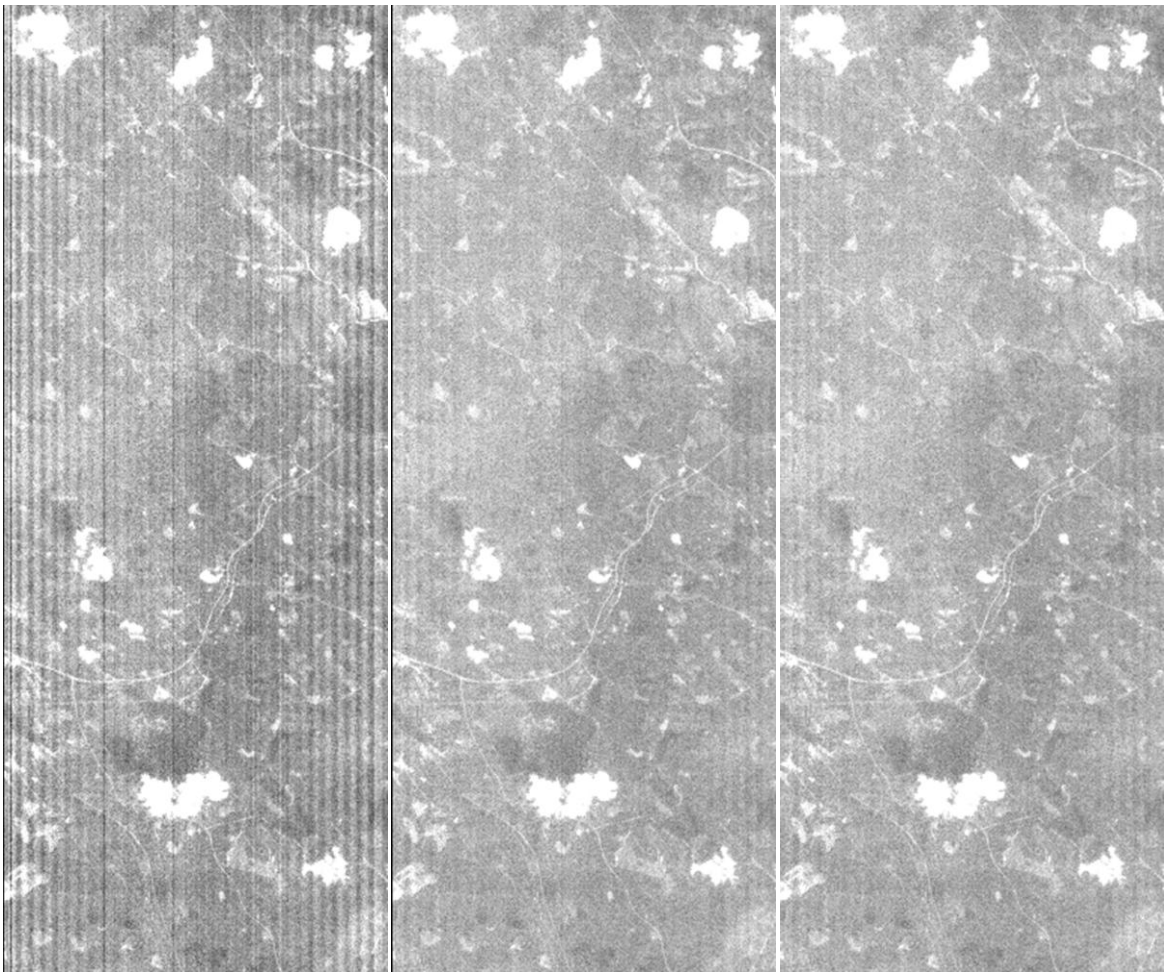

Figure 17. Hyperion band 8: Original (left), SpecMM corrected (middle), SpecMM and local destriping corrected (right).

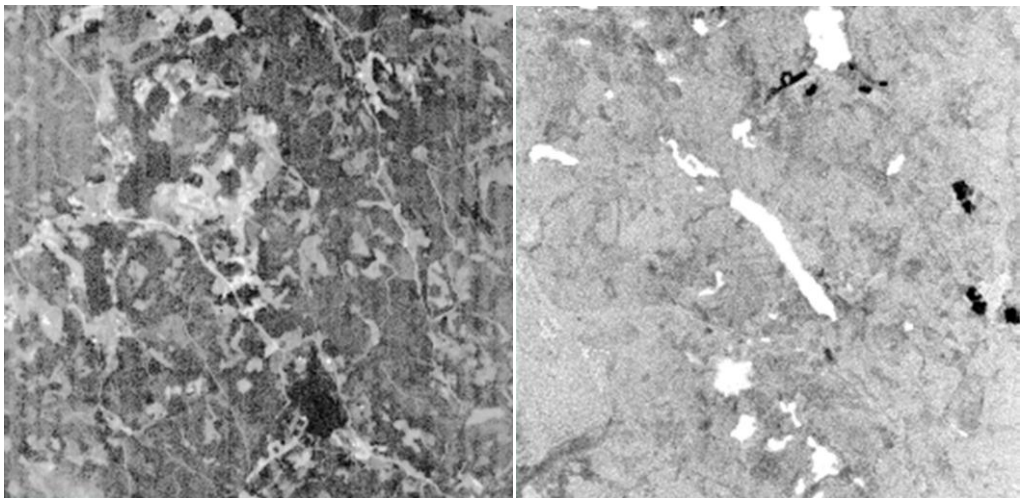

Figure 18. MNF rotation on the VNIR bands of a smile corrected Hyperion image (left). Band math around the 752 nm oxygen absorption feature on a smile corrected image (Hyperion bands 40 – band 42) (right)

The MNF rotation and band math tests suggest that the desmiling process worked well, with no gradient evident after desmiling (Figure 18).

The average difference in percentage reflectance between desmiled and non-desmiled atmospherically corrected forest plots can be in Figure 19. We can see that the desmiling has a large impact in the sub 500 nm region. There is also a large peak at 925 nm; this is due to the switch from the VNIR detecting array to the SWIR detecting array. In addition to these we

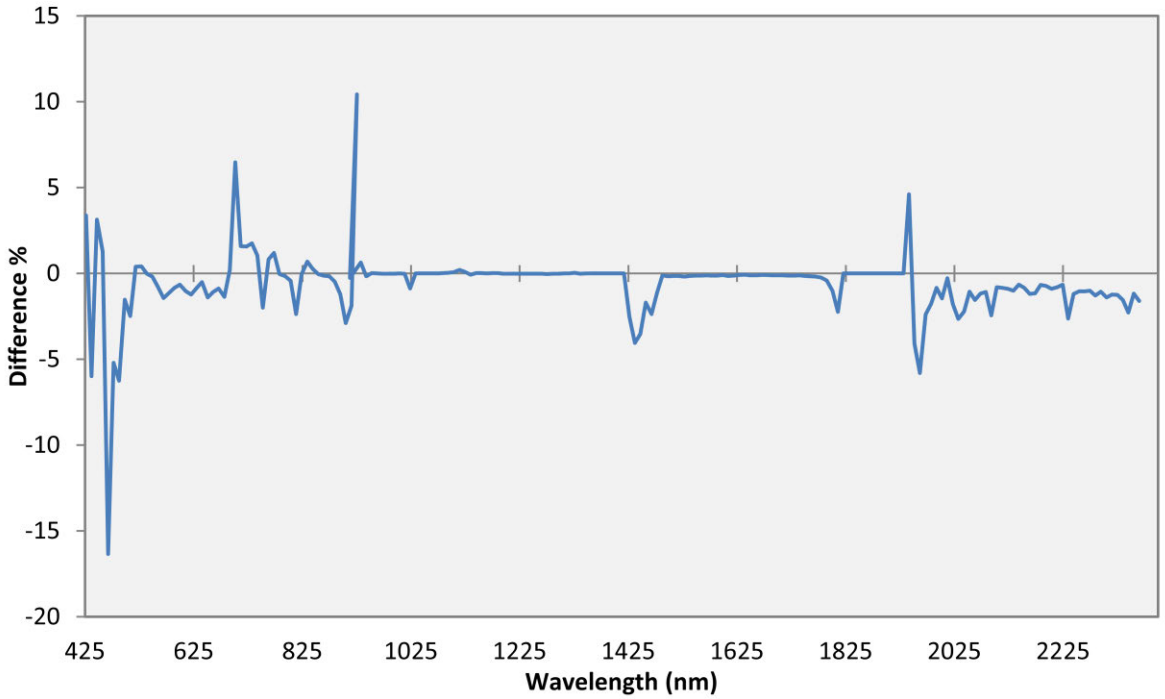

Figure 19. Average percentage difference between absolute reflectance from desmiled and non-desmiled forest plots, using the average of 74 field plots.

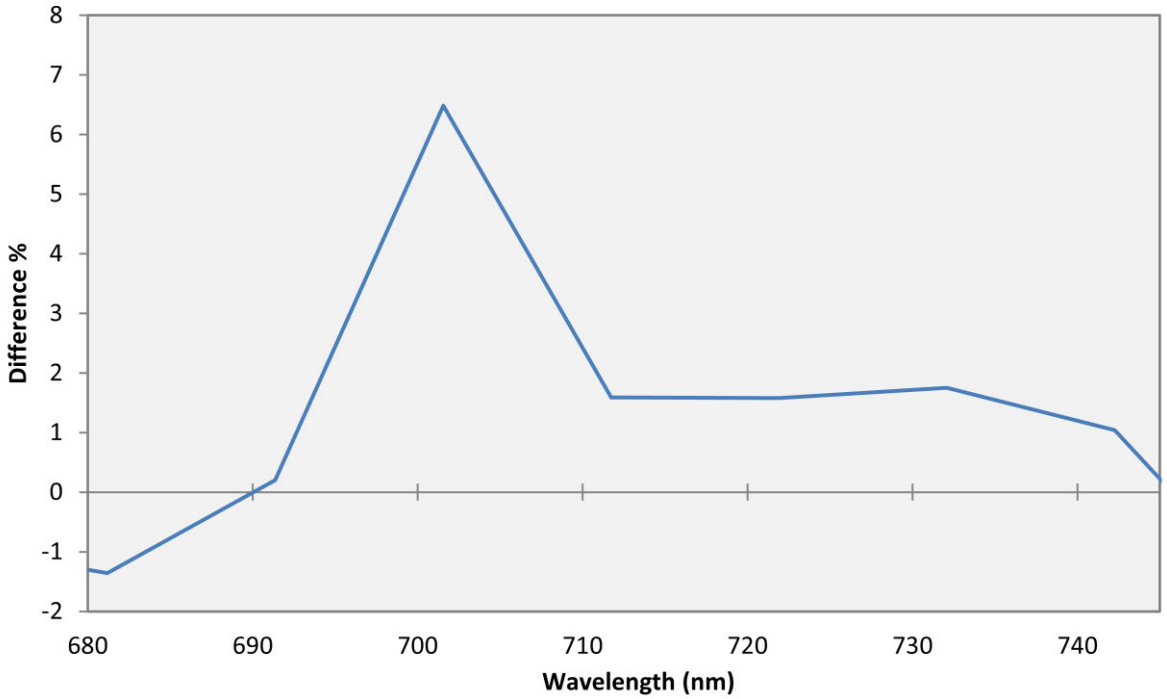

Figure 20. Average percentage difference in the red-edge between desmiled and non-desmiled forest plots, using 74 known field plots.

can see that the red edge region from 680 nm to 720nm is heavily impacted.

A detailed look at the difference in the red-edge part of the spectrum in Figure 20 shows a difference of about 7% at 700 nm. This change in reflectance can be linked to the across-track position of the plots. In Figure 21 we can see the correlation between the difference in the red-edge region of the spectrum and the longitude of each plot, which is

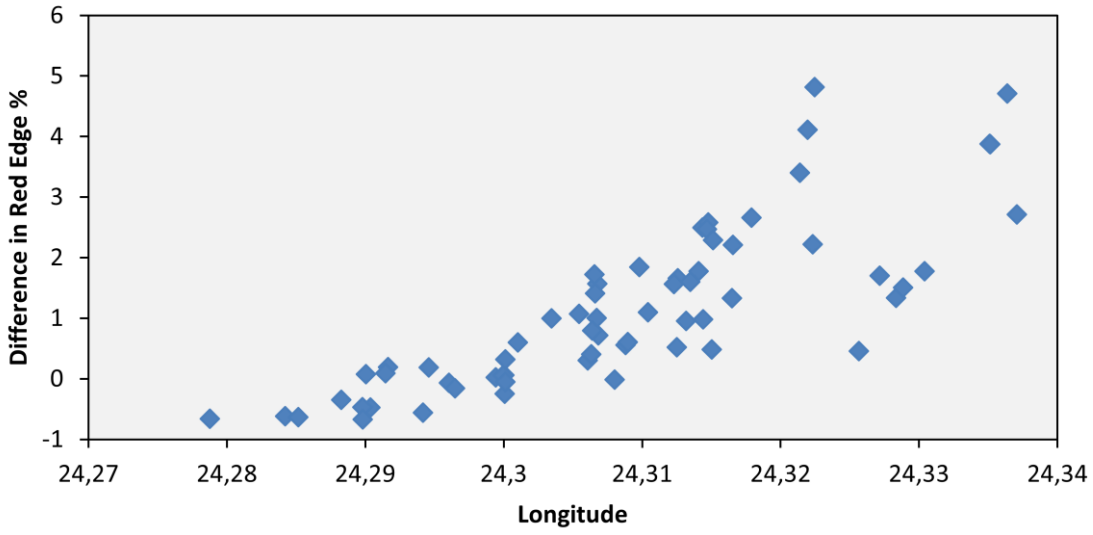

Figure 21. Average difference in bands 34 to 39 between desmiled and non-desmiled forest plots, plotted against across-track location represented by longitude.

correlated with the across-track position of the plot. As expected the plots located on the far right side of the scene are the most impacted by the desmiling.

Table 5. Geocorrection root mean square deviation (RMSD) for each scene

DOY	RMSD
125	0.3973
153	0.385
161	0.2681
184	0.3945
195	0.3395

While spectral smile can change as the instrument ages, the overall character of the smile should stay similar. As Khurshid *et al.* (2006) show, the spectral smile of the VNIR array has not changed significantly, however that of the SWIR has. The smile is no longer primarily a function of cross-track position, but a general shift of about 2 nm towards a longer wavelength. This shift cannot be detected with the MNF rotation or band math tests. There is thus a possible 2 nanometer error in the central wavelengths of the SWIR bands that the desmiling process used does not correct.

A geocorrection RMSD of under 0.5 was achieved for each scene, signifying an error of less than half a pixel (Table 5). Combined with the misalignment between the two detecting arrays, a geographical accuracy of under a pixel can be expected.

5.2. Validation of Hyperion atmospheric correction against field spectroscopy measurements

Figure 22 to Figure 26 show the ATCOR and FLAASH reflectance factors plotted against the *in situ* measured reflectance factors. The plots are limited in wavelength by the spectral range of the field spectrometer. As can be clearly seen from all of the plots, the shift between the VNIR and SWIR sensing arrays is clearly evident. The shift in sensing arrays is located in an area of heavy atmospheric absorption. This area will not be considered in this analysis and the area was not taken into account in the statistical analysis (Table 6). Of note are the very low reflectance values seen in the short wavelengths in the FLAASH reflectance factors for all of the scenes. The reflectance factors produced by FLAASH for wavelengths below 480 nm are likely not reliable. However on the whole both algorithms produce very similar results.

In the DOY 125 plot the *in situ* reflectance is substantially higher than either the FLAASH or ATCOR reflectance (Figure 22). The difference is consistent throughout all wavelengths, with an overall MD of over -0.5 for both FLAASH and ATCOR (Table 6). The shape of the spectra is however similar to the field reference measurement. There is very little difference between the two atmospheric correction methods. ATCOR produces a slightly higher reflectance value for the shorter wavelengths, a trend that can also be seen in the

following dates. This date produced the worst overall RMSE values, with both algorithms over 0.06 (Table 6).

For the DOY 153 plot we see a very good fit between the *in situ* reflectance and both the FLAASH and ATCOR reflectances (Figure 23). FLAASH performs particularly well in the visible wavelengths, with the exception of the very short wavelengths. ATCOR performs slightly better in the NIR. FLAASH performs slightly better overall, obtaining a MD value of under 0.0015 (Table 6). We see RMSE values of under 0.012 for both algorithms, indicating a very good fit to the *in situ* reflectance (Table 6).

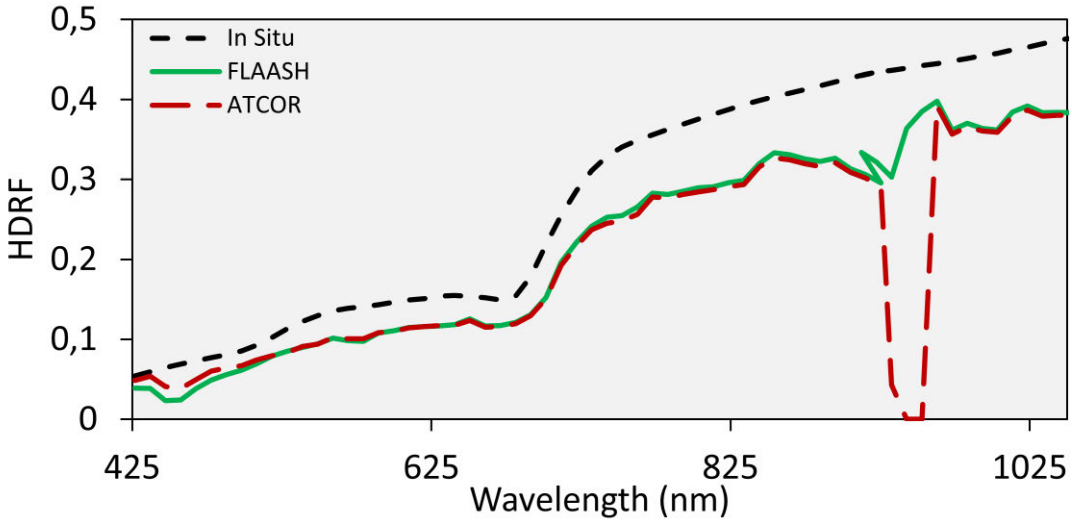

Figure 22. Comparison of HDRF from atmospherically corrected Hyperion images and *in situ* HDRF measurements from a homogeneous grass field. Day of year: 125 (2010/05/05).

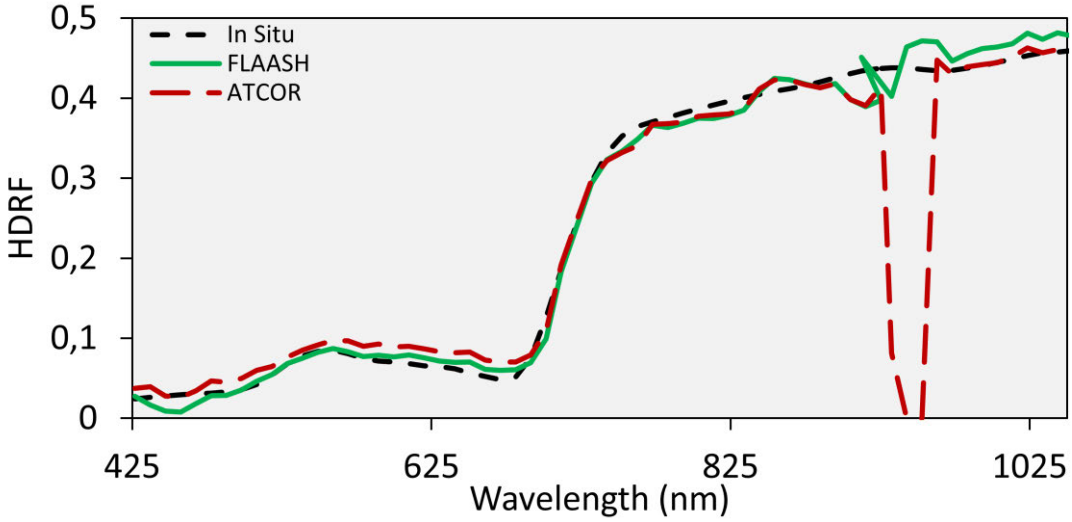

Figure 23. Comparison of HDRF from atmospherically corrected Hyperion images and *in situ* HDRF measurements from a homogeneous grass field. Day of year: 153 (2010/06/02).

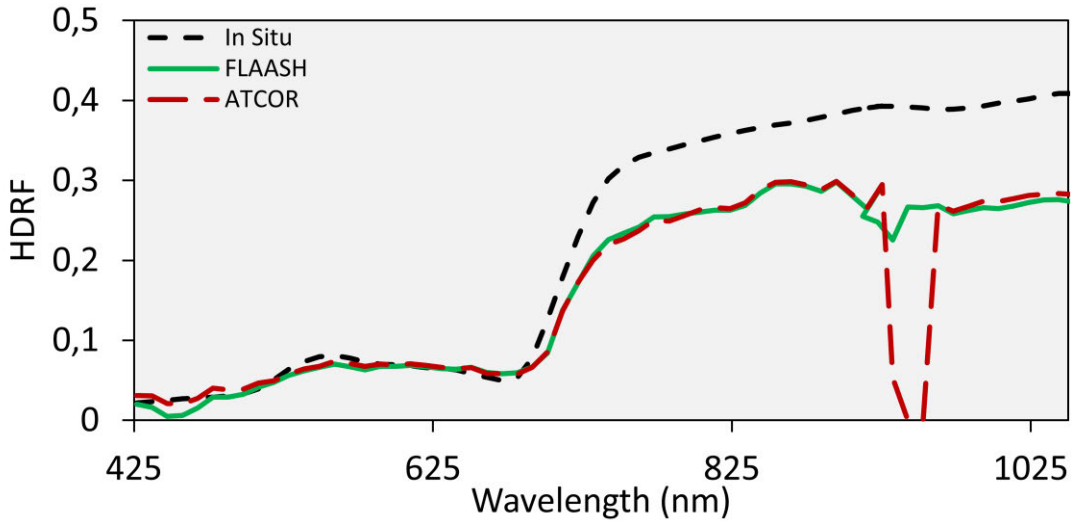

Figure 24. Comparison of HDRF from atmospherically corrected Hyperion images and *in situ* HDRF measurements from a homogeneous grass field. Day of year: 161 (2010/06/10).

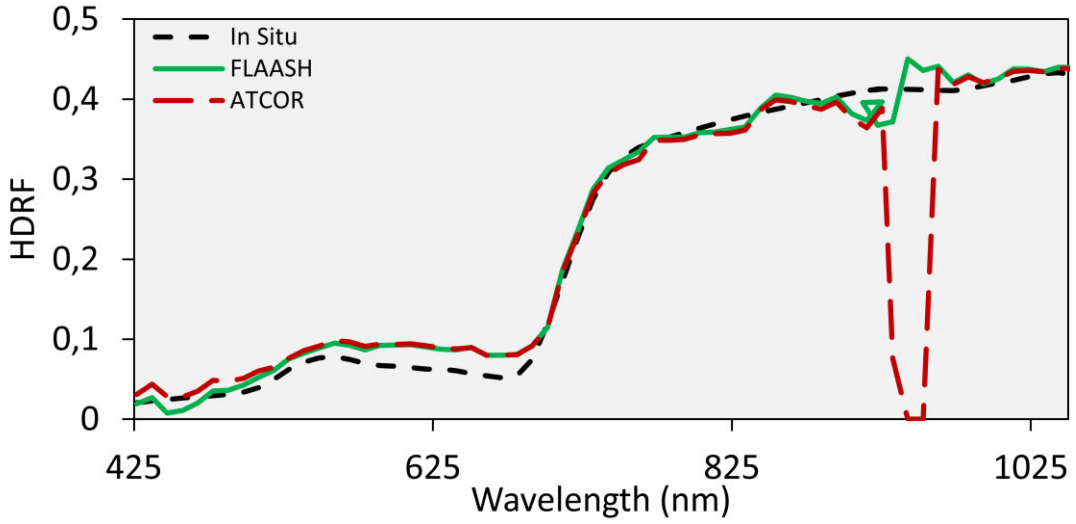

Figure 25. Comparison of HDRF from atmospherically corrected Hyperion images and *in situ* HDRF measurements from a homogeneous grass field. Day of year: 184 (2010/07/03).

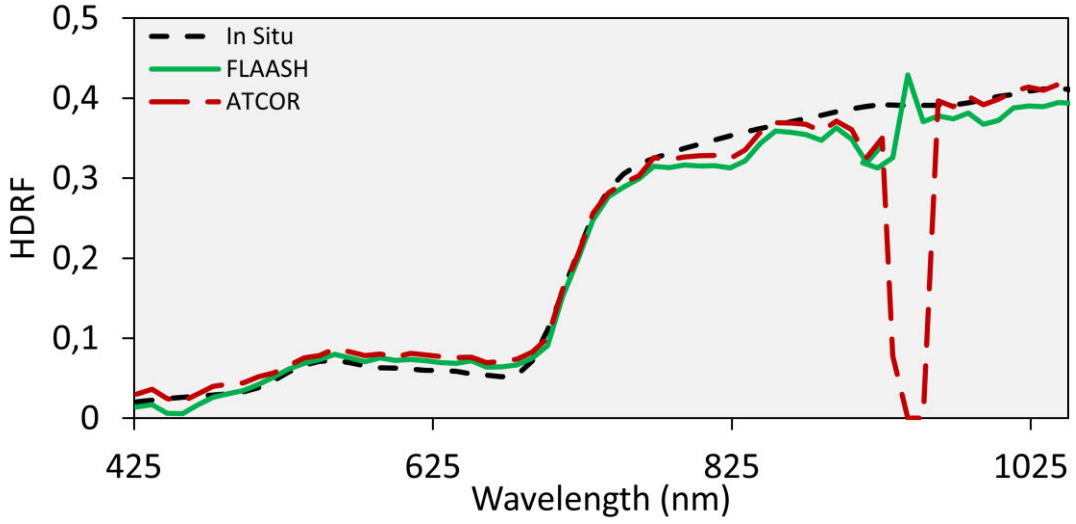

Figure 26. Comparison of HDRF from atmospherically corrected Hyperion images and *in situ* HDRF measurements from a homogeneous grass field. Day of year: 195 (2010/07/11).

The DOY 161 plot also shows a large deviation between the *in situ* measured reflectance and both the FLAASH and ATCOR reflectance (Figure 24). The fit for the visible wavelengths is good. However there is considerable difference in the NIR; resulting in overall RMSE values of over 0.05 for both algorithms (Table 6). The scene had the highest cloud cover of the captured scenes. An unseen thin cloud or shadow may have impacted the Hyperion derived reflectance factors over the field; this is however not evident from a visual inspection of the scene.

DOY 184 has good correlation between the *in situ* measurements and Hyperion (Figure 25). The fit is particularly good in the NIR region. In the visible region, both Hyperion reflectance factors show higher reflectance than the *in situ* measurements. With regard to the RMSE values, ATCOR performs slightly better for this date than FLAASH. This is likely due to the short wavelengths, where FLAASH shows its customary very low reflectance (Table 6).

The final scene, DOY 195, also shows good fit between the Hyperion reflectance factors and *in situ* (Figure 26). Particularly in the SWIR sensing array wavelengths the ATCOR algorithm outperforms FLAASH. It should be noted that the difference in RMSE is minimal; this is due to FLAASH performing very well over a large range of the visible area of the spectrum.

Overall both algorithms performed well, with the DOY 153, 184 and 195 scenes showing exceptional fit. The 125 scene shows a very similar spectral pattern, with just an absolute shift in reflectance, which should not impact the calculation of red edge parameters. While the 161 scene is of some concern, the RMSE values are not overly high at below 0.06 (Table 6). An error of around 6% can be considered good from any form of atmospheric correction.

The results are in accord with San and Suzen (2010), who found that all of the MODTRAN based atmospheric correction algorithms performed well, with slight variations

Table 6. MD and RMSD between Hyperion HDRF and *in situ* measured HDRF

	125	**153**	**161**	**184**	**195**	**Average**
FLAASH MD	-0.0570	0.0014	-0.0521	0.0089	-0.0081	-0.0214
ATCOR MD	-0.0580	0.0053	-0.0488	0.0095	0.0033	-0.0178
FLAASH RMSE	0.0604	0.0114	0.0545	0.0131	0.0154	0.0309
ATCOR RMSE	0.0614	0.0119	0.0529	0.0146	0.0118	0.0305

between wavelength regions. The Hyperion spectra do however show considerable noise compared to the *in situ* measurements, especially around atmospheric absorption features. This can likely never be corrected using atmospheric correction. The use of spectral smoothing could prove beneficial for overall accuracy; however the applicability of spectral smoothing for Hyperion data would require extensive further study.

5.3. Validation of Hyperion atmospheric correction against MODIS products

In contrast to the grass field spectra, a clear difference can be seen between the two algorithms in the visible part of the spectrum when comparing them to the MODIS reflectance (Figure 27, Figure 28 and Figure 29). The FLAASH reflectance factors are lower than the ATCOR produced ones for the MODIS green and red bands. The NIR part of the spectrum is

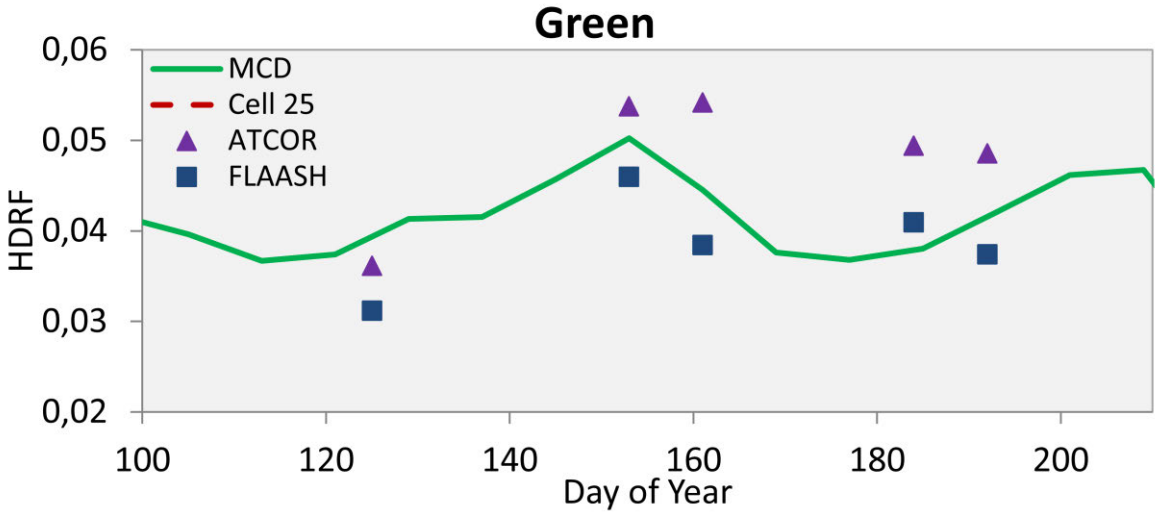

Figure 27. Seasonal comparison of the MODIS MCD43A4 product against Hyperion FLAASH and ATCOR corrected HDRF. The MCD43A4 product has a temporal resolution of 8 days. The Hyperion bands were binned to corresponding MODIS bands. The MOD13Q1 product is not produced for the green band.

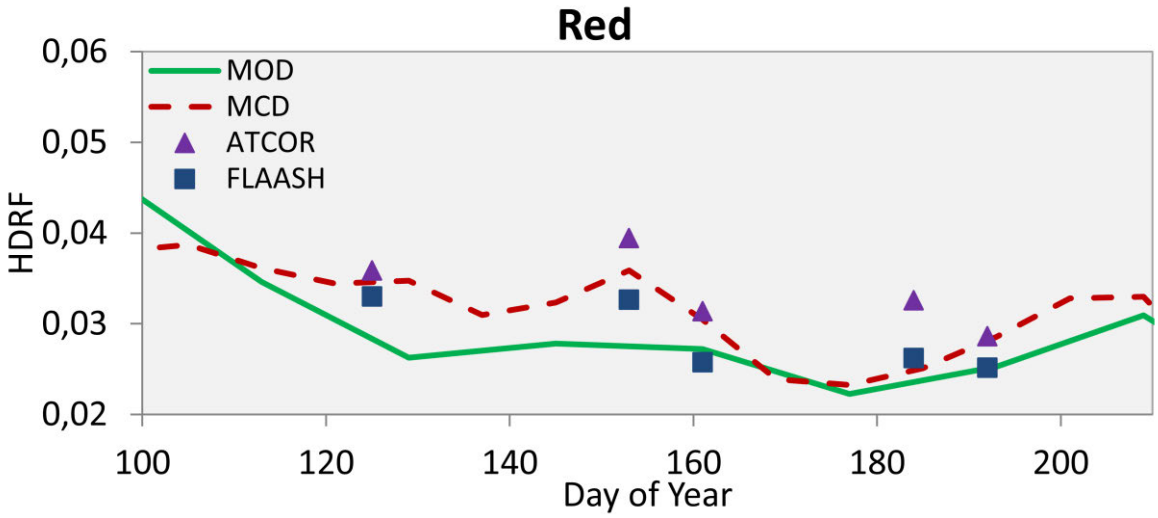

Figure 28. Seasonal comparison of the MODIS MCD43A4 and MOD13Q1 products against Hyperion FLAASH and ATCOR corrected HDRF. The MCD43A4 product has a temporal resolution of 8 days, and the MOD13Q1 16 days. The Hyperion bands were binned to corresponding MODIS bands.

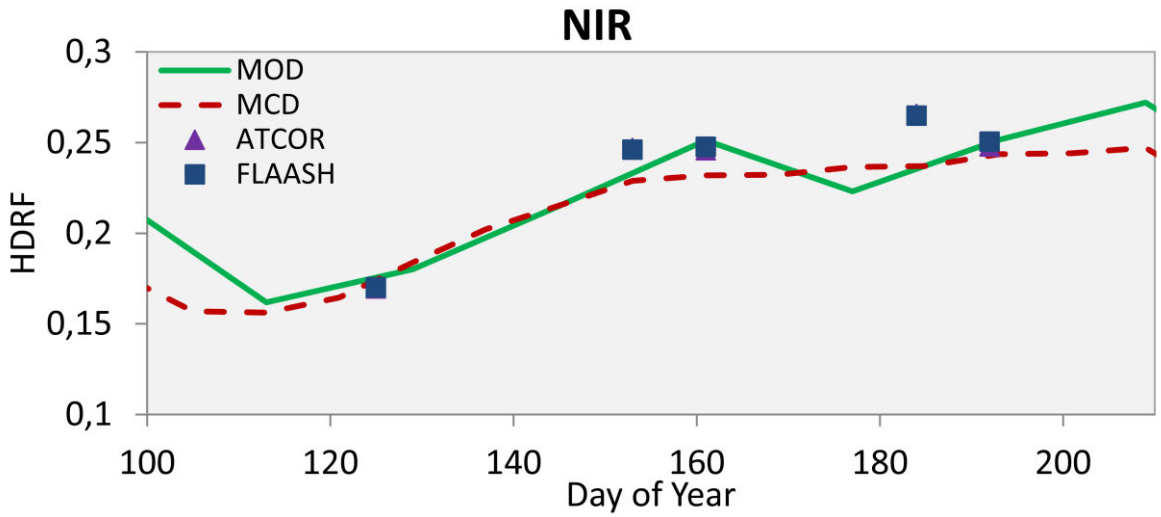

Figure 29. Seasonal comparison of the MODIS MCD43A4 and MOD13Q1 products against Hyperion FLAASH and ATCOR corrected HDRF. The MCD43A4 product has a temporal resolution of 8 days, and the MOD13Q1 16 days. The Hyperion bands were binned to corresponding MODIS bands.

very similar for both algorithms. Overall we can also see a very good agreement between the Hyperion derived reflectance factors and the MODIS reflectance products.

For the green band, we can see that both reflectance factors follow the trend set by the MODIS data very well (Figure 27). ATCOR produces a slightly higher reflectance factor than the MODIS product, signified by a MD value of around 0.003 (Table 7). FLAASH on the other hand overall produces a lower reflectance value than the MODIS product. FLAASH also has a slightly lower RMSE (Table 8).

The red band also shows a good fit between the MODIS product and both Hyperion reflectance factors (Figure 28). FLAASH seems to work very well, producing a reflectance factor in between the two MODIS products. FLAASH achieves a RMSE value of under 0.004 for both of the MODIS products. The ATCOR reflectance factor performs slightly worse in this comparison, being closer to the MODIS MCD reflectance product. However the overall trend is similar.

Both Hyperion reflectance factors are almost identical in the NIR band (Figure 29). In contrast to the validation against the grass field, the

Table 7. MD between Hyperion HDRF and MODIS products. The MOD13 product is not produced for green.

MD	Green	Red	NIR	Average
ATCOR MCD	0.0029	0.0028	0.0132	0.0063
ATCOR MOD		0.0072	0.0071	0.0072
FLAASH MCD	-0.0034	-0.0018	0.0128	0.0025
FLAASH MOD		0.0026	0.0067	0.0047

Table 8. RMSD between Hyperion HDRF and MODIS products. The MOD13 product is not produced for green.

RMSD	Green	Red	NIR	Average
ATCOR MCD	0.0056	0.0039	0.0172	0.0089
ATCOR MOD		0.0079	0.0152	0.0115
FLAASH MCD	0.0049	0.0025	0.0166	0.0080
FLAASH MOD		0.0033	0.0146	0.0090

DOY 184 reflectance factor in the NIR seems to be slightly too high. On the whole we can see a good fit between the MODIS reflectance and the Hyperion reflectance factors.

Based on the comparison to MODIS data the FLAASH algorithm seems to perform slightly better. However both algorithms produce a good fit to the MODIS products, following the overall seasonal trends, and the use of either could be justified.

5.4. Red edge inflection point calculation

In Figure 30 we can see the seasonal time series of the REIP for the understory forest

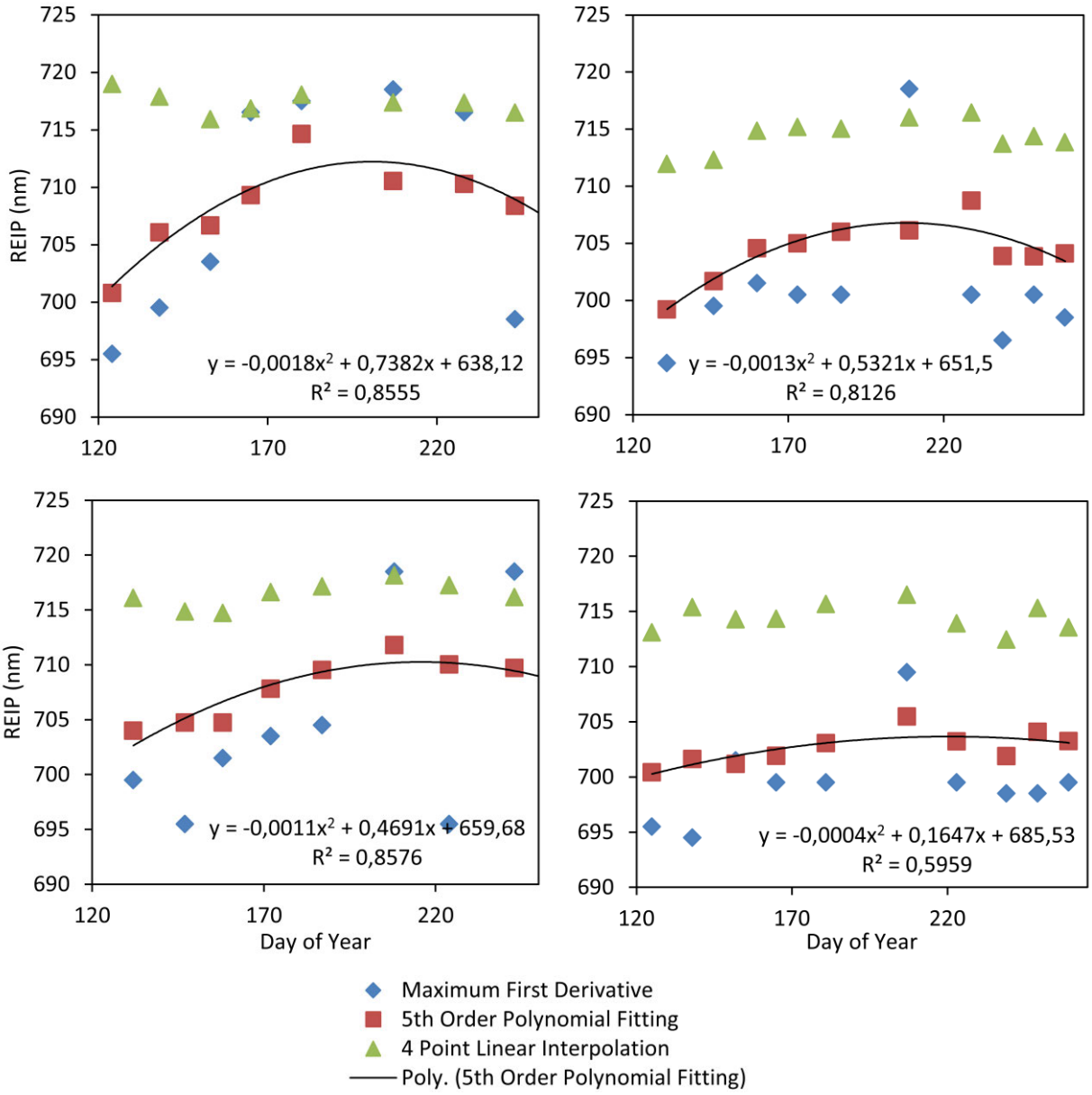

Figure 30. Seasonal comparison of REIP calculated using different methods, using in situ measured understory HDRF from forest sites. A second order polynomial is fitted to the fifth-order polynomial fitting method REIP values, with the R^2 values and equations of the fitting shown. H3 Herb-rich birch site (top left), U26 Mesic spruce site (top right), U18 Sub-Xeric pine site (bottom left), U10 Xeric Scots pine site (bottom right).

plots, for each of the calculation methods. The different calculation methods produce different REIP results; resulting in different seasonal patterns in REIP. From the literature review we can expect the red edge and subsequently the REIP to be either correlated with LAI or chlorophyll content (Gates et al., 1965; Filella and Peñuelas, 1994; Kodani et al., 2001; Pu et al., 2003; Zhang et al., 2007; Herrmann et al., 2010). The seasonal trend in REIP should thus follow the seasonal trend found in LAI and chlorophyll, with strong growth in the spring, a plateau in the summer, and fall in the autumn (Kodani *et al*., 2001; Rautiainen *et al*., 2009; Rautiainen *et al*., 2011). The trend should be strongest in the H3 birch site due to the seasonal growth patterns of the herbaceous species and graminoids that are dominant in the understory (Rautiainen *et al*., 2011). The least variation should be seen the xeric U10 pine site with lichens and heathers, which show less seasonal variation (Rautiainen *et al*., 2011).

The fifth-order polynomial fitting method shows strong seasonal trends for three of the plots. The xeric U10 pine plot shows little variation over the growing season, as expected due to its composition. There is some seasonal variation; it is however not on the same scale as the other three sites. The other sites show a clear trend in the REIP with strong increase for the first half of the growing season and steady decline in the second half. Overall the trend is as expected; with strong seasonal change in reflectance following the expected changes in the LAI and chlorophyll content of the understory vegetation.

The maximum first derivative calculation also shows a seasonal trend in REIP. However there are also changes in the REIP that are not explained by seasonal patterns in LAI or chlorophyll. Unlike the gradual change seen in the polynomial fitting, the changes are often drastic, with changes of over 10 nm in REIP from one measurement to the next. This may partly be due to the nature of the spectral measurements, with diffuse illumination and heterogeneous surfaces. However the jumps are seen in all of the four sites, suggesting that the maximum first derivative is being impacted by noise in the data rather than seasonal changes in the red edge.

The four-point linear interpolation method produces very little variation in REIP. The method produces REIP values around 715 nm independent understory composition or day of year. The method shows the weakest trend over the growing season.

Both the maximum first derivative and fifth-order polynomial fitting methods show the expected seasonal trends in REIP. However the maximum first derivative also shows large changes independent of the seasonal trend. The polynomial fitting method produces gradual

changes in REIP that follow the expected trends outlined by the literature. The polynomial fitting also shows outliers from the general trend, likely due to the variation in illumination conditions and potentially due to spatial variation. Because of this a second-order polynomial was fitted to the polynomial fitting time series of REIP values. This was done eliminate outlier from the seasonal time series, and allowed for interpolation to satellite dates for correlation.

In Figure 31 we can see the seasonal time series of REIP from the Hyperion imagery for the forest plots. The U10 pine site was not visible in three of the Hyperion images and

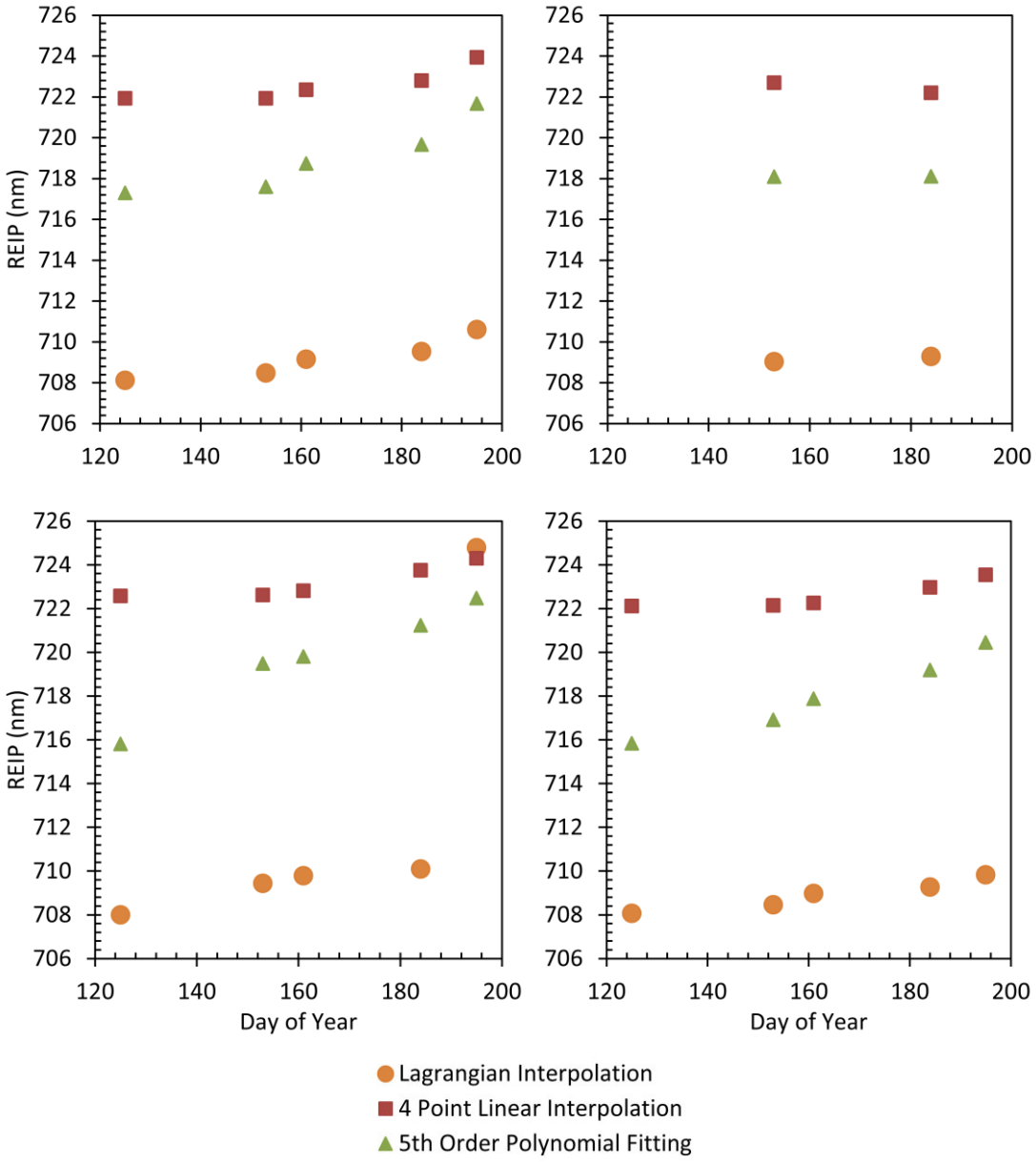

Figure 31. Seasonal comparison of REIP from forest sites calculated using different methods from FLAASH atmospherically corrected Hyperion top-of-canopy HDRF. U26 spruce site (top left), U10 pine site (top right), H3 birch site (bottom left), U18 pine site (bottom right). Only two imaging dates are available for the U10 pine site.

thus only consists of two points. The Hyperion imagery is from above the canopy and the time series covers a shorter time period so the trends are less clear than with the *in situ* data.

Overall the strongest seasonal trend in REIP should be seen the broadleaf H3 birch site. As broadleaf sites have the largest change in LAI and canopy chlorophyll content. As outlined by Rautiainen *et al*. (2011), the coniferous sites also show a seasonal trend in LAI, with the exception of the U10 pine site, which showed very little variation in LAI. The seasonal variation of chlorophyll content in the canopy of coniferous sites is unclear from the literature (Silkina and Vinokurova, 2008).

Like with the *in situ* data, the four-point linear interpolation method shows very little variation in REIP. The REIP stays constant at around 722 nm, independent of forest type or measurement date.

The Lagrangian interpolation method shows an increasing trend in REIP over the time series. The change is gradual, with the exception of the H3 birch site, which shows a dramatic increase for the last date (Figure 31). The Lagrangian interpolation method is sensitive to the shift in maximum first derivative, which is used as the central point for the interpolation.

The fifth-order polynomial fitting shows the largest overall change in REIP. The REIP increases over the growing season for most plots as expected. The change is largest in the H3 birch site, with a growth in REIP from around 716 nm to 722 nm. The U10 pine site shows practically no change between the two measurements. The fifth-order polynomial fitting

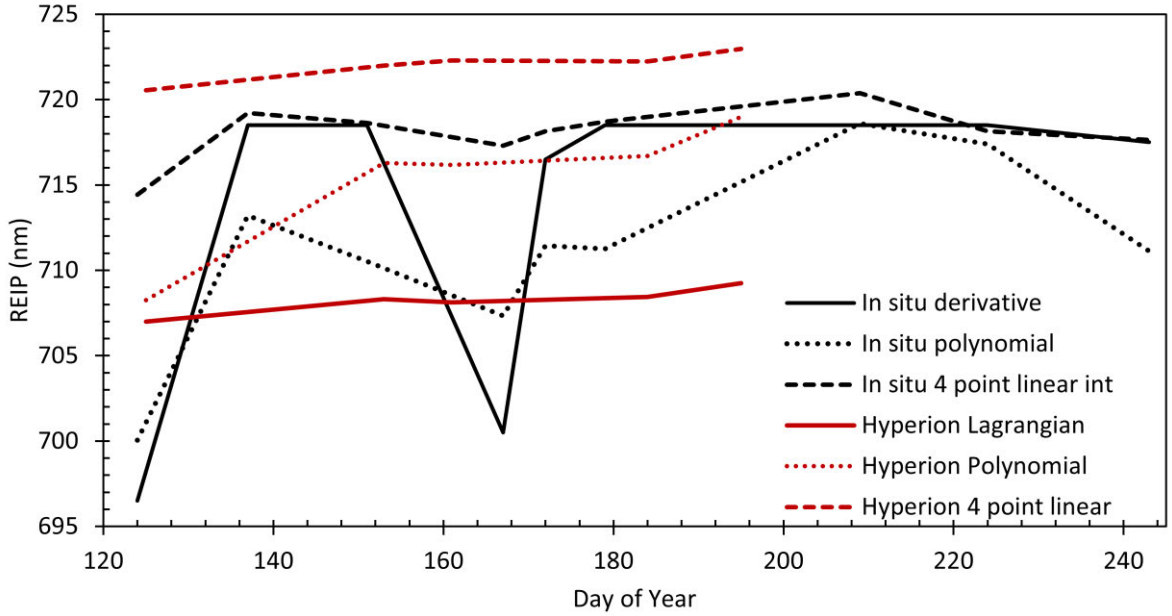

Figure 32. Seasonal comparison of the grass field REIP calculated using different methods from is situ spectroscopy measurements and Hyperion imagery.

produces a time series of REIP in accordance to expectations.

A direct comparison of REIP from both the *in situ* and Hyperion data can be made using the grass field (Figure 32). Like with the understory and forest plots, the four-point linear interpolation method shows little change for either the Hyperion or *in situ* data. The Lagrangian interpolation for the Hyperion data stays also shows little variation over the season. The maximum first derivative from *in situ* data show a general trend, with a rapid increase in the spring and plateau over the summer, with the exception of DOY 167, which dramatic drop from the summer plateau.

Looking at just the fifth-order polynomial fittings in Figure 33 we can see a clear trend over the growing season. The trend shows a gradual increase in the REIP over the growing season. The *in situ* time series also shows some variation in REIP that is not accounted for by a seasonal trend. The site is not completely homogeneous, being a grass field that is being used throughout the summer. The grass in the field is cut at times and parts of the field are used for sports leading to variation in the spectral reflectance not caused by typical seasonal change. If a second-order polynomial is fitted to the two time series of REIP we can see very similar trends. There is an absolute difference between the two REIP trends of about 5 nm; the shift is less than the Hyperion spectral resolution of 10 nm. The similarities between the trends give us confidence in the use of the polynomial fitting method for extracting the REIP

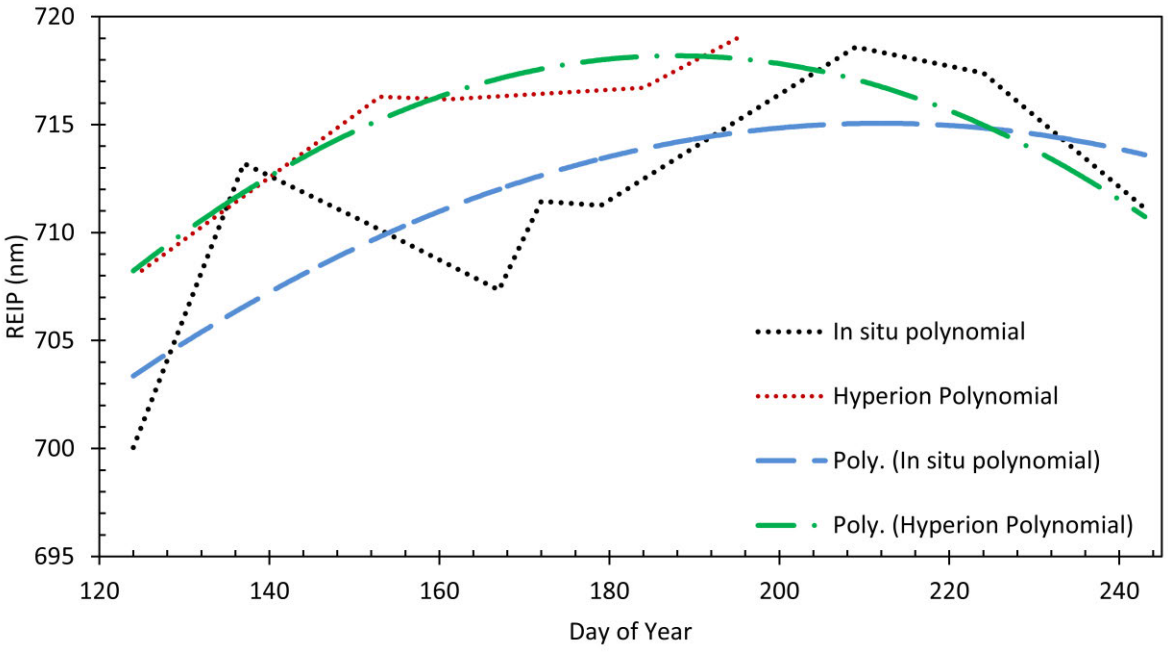

Figure 33. Seasonal comparison of grass field REIP calculated using the fifth-order polynomial fitting method from both Hyperion HDRF and *in situ* measured HDRF. Second order polynomials were fitted to both time series.

from Hyperion and field spectroscopy data.

Based on the seasonal trends, the fifth-order polynomial fitting is the best method for calculating the REIP from both the understory and Hyperion data. The method produces seasonal trends that follow the expected seasonal trends of LAI and chlorophyll in vegetation. The maximum first derivative method from the very high resolution understory measurements also followed the expected seasonal trend; however the method is too sensitive to noise in the data. The Lagrangian interpolation method from Hyperion data showed little to no change in REIP in any scene. The four-point linear interpolation, which Pu et al. (2003) showed to have the highest correlation with LAI, showed very little seasonal change in either the understory or Hyperion sites.

5.5. Hyperion red edge inflection point comparison against canopy leaf area index and understory red edge inflection point

In Figure 34 we see a seasonal time series of tree-level LAI, understory REIP from *in situ* measurements and top of canopy REIP from Hyperion. Overall the three variables show similar trends over the time series (Figure 34).

Particularly the REIP trends follow each other very closely for all four sites. There is gradual increase in REIP of the growing season. An absolute difference between the understory REIP and the Hyperion REIP, of about 15 to 20 nm, can however be seen, with the Hyperion REIP being higher. The similarity between the two REIP trends is striking. The largest difference can be seen in the U10 pine site, where the Hyperion REIP shows almost no change, while the understory shows a slight increase in REIP (Figure 34). The site however only has two Hyperion measurements.

The three coniferous sites also show a good correlation between LAI and both REIP trends. We see a gradual increase in LAI over the growing season.

The H3 birch plot shows a clear difference between the LAI trend and the two REIP trends. The LAI trend follows the trend outlined by the literature, with a rapid growth in the spring and plateau in the summer. The REIP trends however show a gradual and smoother increase over the growing season without the plateau in the summer (Figure 34).

Figure 35 shows the comparison of REIP from Hyperion images and LAI. Using all the data points there was no correlation between REIP and LAI ($R^2 < 0.13$). On an individual site basis there is a high correlation: U18 pine $R^2 = 0.86$, U26 spruce $R^2 = 0.8$, H3 birch $R^2 =$

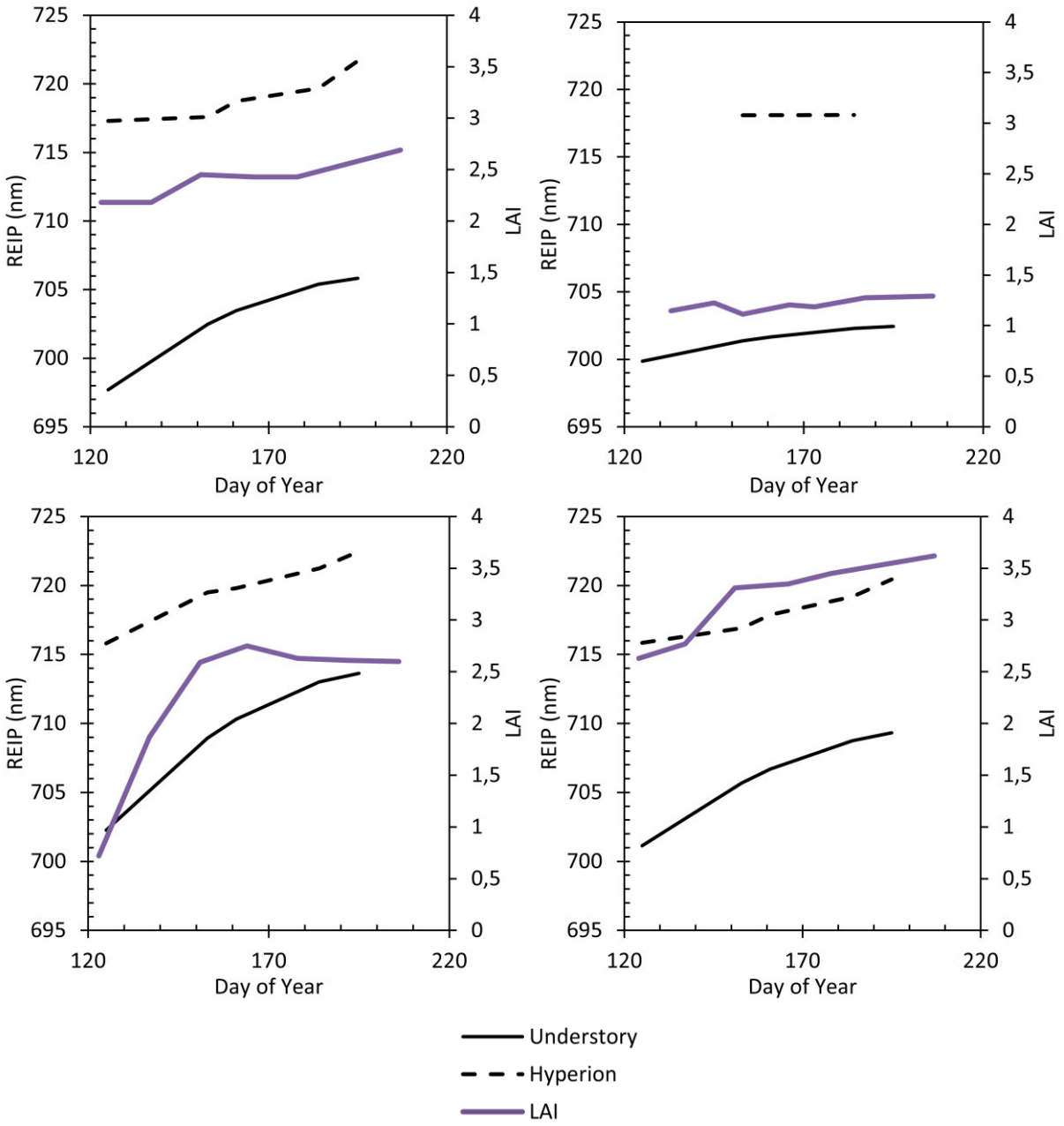

Figure 34. REIP calculated using the fifth-order polynomial fitting method from in situ understory HDRF and top-of-canopy Hyperion HDRF. Plotted with canopy-level LAI. U26 spruce site (top left), U10 pine site (top right), H3 birch site (bottom left), U18 pine site (bottom right). Only two Hyperion imaging dates are available for the U10 pine site.

0.79. The change in LAI is small for plots with the highest correlation: U18, and U26 (Figure 35). However, even the H3 birch site has a high correlation between Hyperion REIP and LAI ($R^2 = 0.79$).

Figure 36 shows the REIP of the understory against the REIP from Hyperion images. The second-order polynomial curve, from the fifth-order polynomial fitting was used for the correlation. There is an absolute difference in the REIP values, with the Hyperion REIP values being about 15 nm higher than the understory REIP. When excluding the grass field site, there is a strong linear relationship ($R^2 = 0.59$) between the REIP estimates. The grass

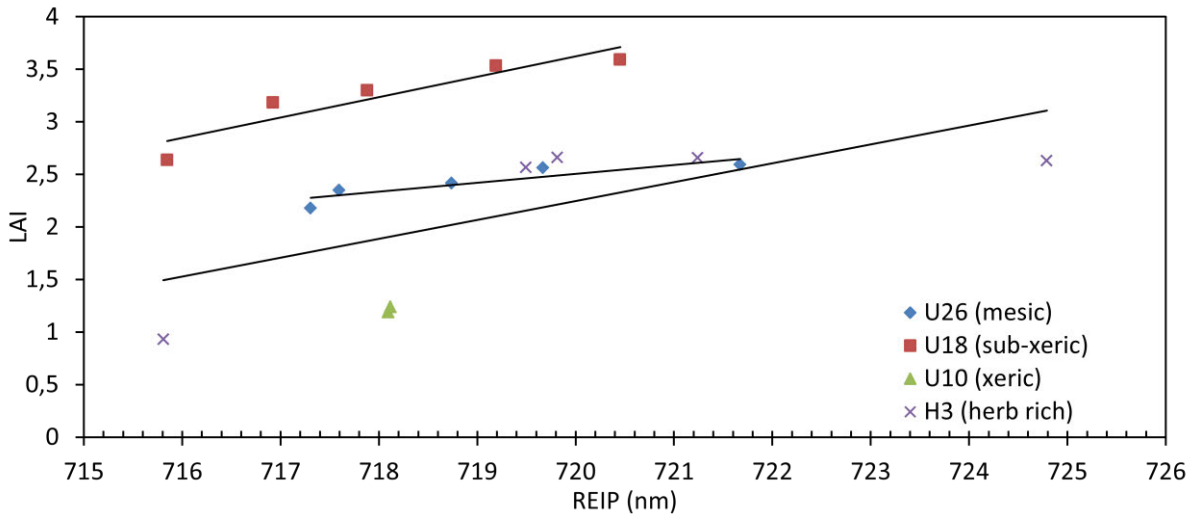

Figure 35. Hyperion REIP calculated using the polynomial fitting method plotted against LAI. R^2 values for individual plots: U18 pine 0.86 (square), U26 spruce 0.8 (diamond), H3 birch 0.79 (cross), U10 pine (triangle, no regression line). Only two dates were available for the U10 pine site, so no regression line was fitted.

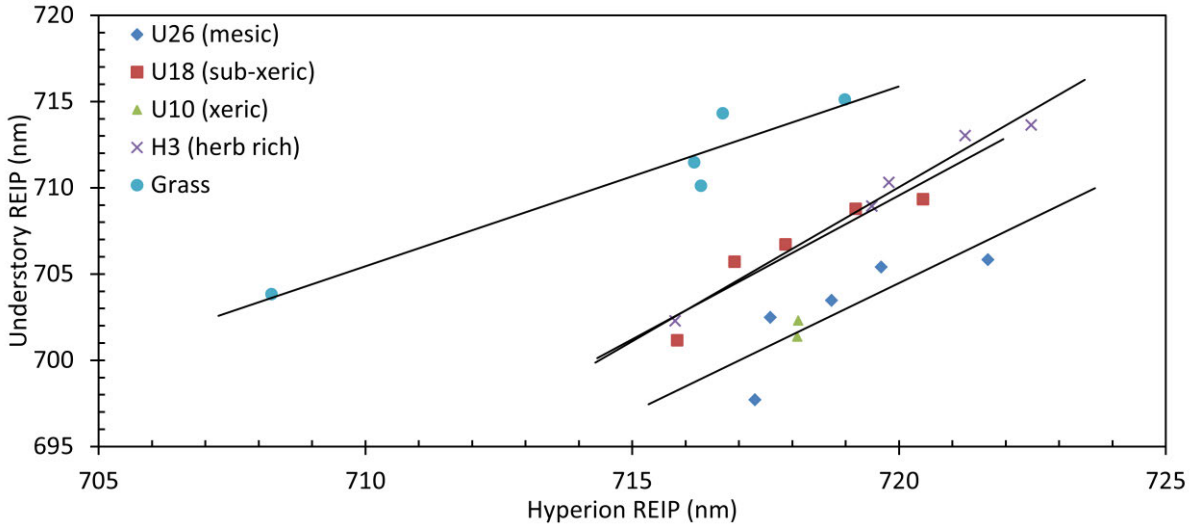

Figure 36. Understory REIP calculated using the polynomial method plotted against the Hyperion REIP calculated using the polynomial method. R^2 values for individual plots: U18 pine 0.87 (square), U26 spruce 0.66 (diamond), H3 birch 0.98 (cross), U10 pine (triangle), grass 0.91 (circle). Only two dates were available for the U10 pine site, so no regression line was fitted.

field was not included because it showed overall a higher REIP values than the other *in situ* measurements. This is likely caused by the difference in measurement conditions, direct light for the grass field compared to diffuse for the other four sites. For individual sites we see mainly a high correlation between the two REIP trends: U18 pine $R^2 = 0.87$, H3 birch $R^2 = 0.98$, grass $R^2 = 0.91$. The U26 spruce site has the lowest correlation between the two REIP trends with an R^2 value of just 0.66.

In contrast to Pu et al. (2003), there was no overall correlation between Hyperion REIP and canopy level LAI, with R^2 value of less than 0.13. On an individual site basis there was however strong correlation between the two parameters. The lack of correlation may

partly be due to the small sample size of this study, with only four sites and a maximum of five measurements per site. As seen in the Birch H3 site, the LAI trend significantly differs from the Hyperion REIP trend despite a high correlation (Figure 34). Changes in LAI do not fully explain the seasonal changes of the Hyperion REIP. The understory REIP on the whole shows a better correlation with Hyperion REIP than LAI does.

Unfortunately the Hyperion scenes did not exceed past the peak of the growing season, the dynamics of the REIP in the autumn would be of interest.

5.6. Red edge dynamics

A look at the first derivative values in the red edge can give us an insight into the red edge and how the different REIP calculation methods work. The REIP is simply the point in the red edge where the rate of change is the highest; however the rate of change within the red edge is not Gaussian with a clearly defined highest peak. The rate of change is influenced by the type

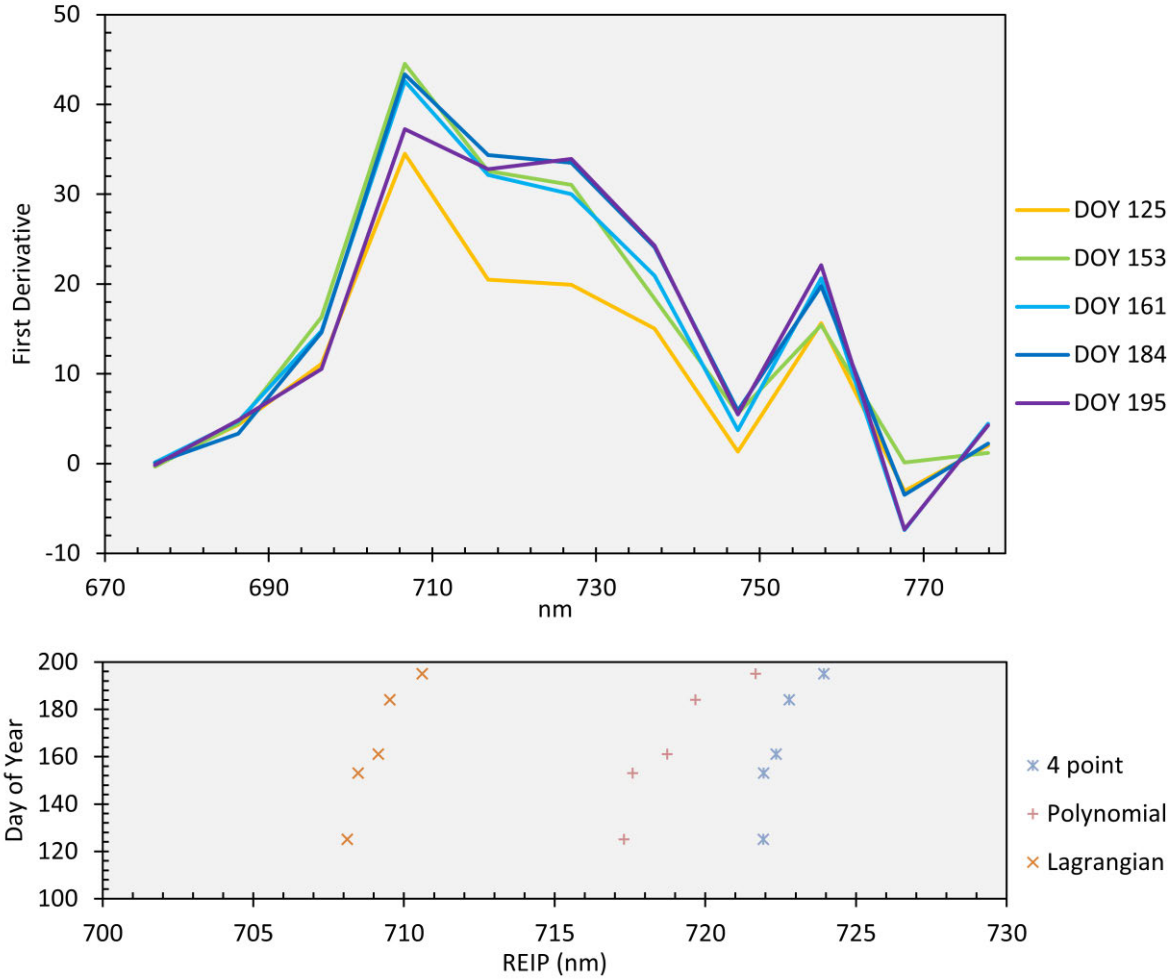

Figure 37. Seasonal development of the Hyperion red edge in the U26 spruce site. Lines show the first derivative values for wavelengths in between Hyperion bands for the red edge (top). Markers show the calculated REIP (bottom).

of vegetation and the season.

As has been pointed out by Filella and Peñuelas (1994), and Kodani et al. (2001) the first derivative of the red edge generally has two distinctive peaks. These peaks can also be seen in the Hyperion data, with a strong peak at 706nm, with the second peak coming at 726nm (Figure 37, Figure 38, and Figure 39). This trend develops over the growing season, while the first peak shows little change in intensity, the second peak becomes more pronounced later in the growing season. In addition a peak can be seen at 757nm in Hyperion data; however this is located in the 'shoulder' before the NIR plateau and is caused by the O_2 absorption feature at 760 nm.

In Figure 37 we can see a slight development of the double peak for the U26 spruce site; the latter peak is not very evident for most of the growing season. The height of the first derivative peak at 706nm stays almost constant for DOY 153 to DOY 185. The first peak is lower for DOY 125 and DOY 195. The second peak at 726nm grows over the season

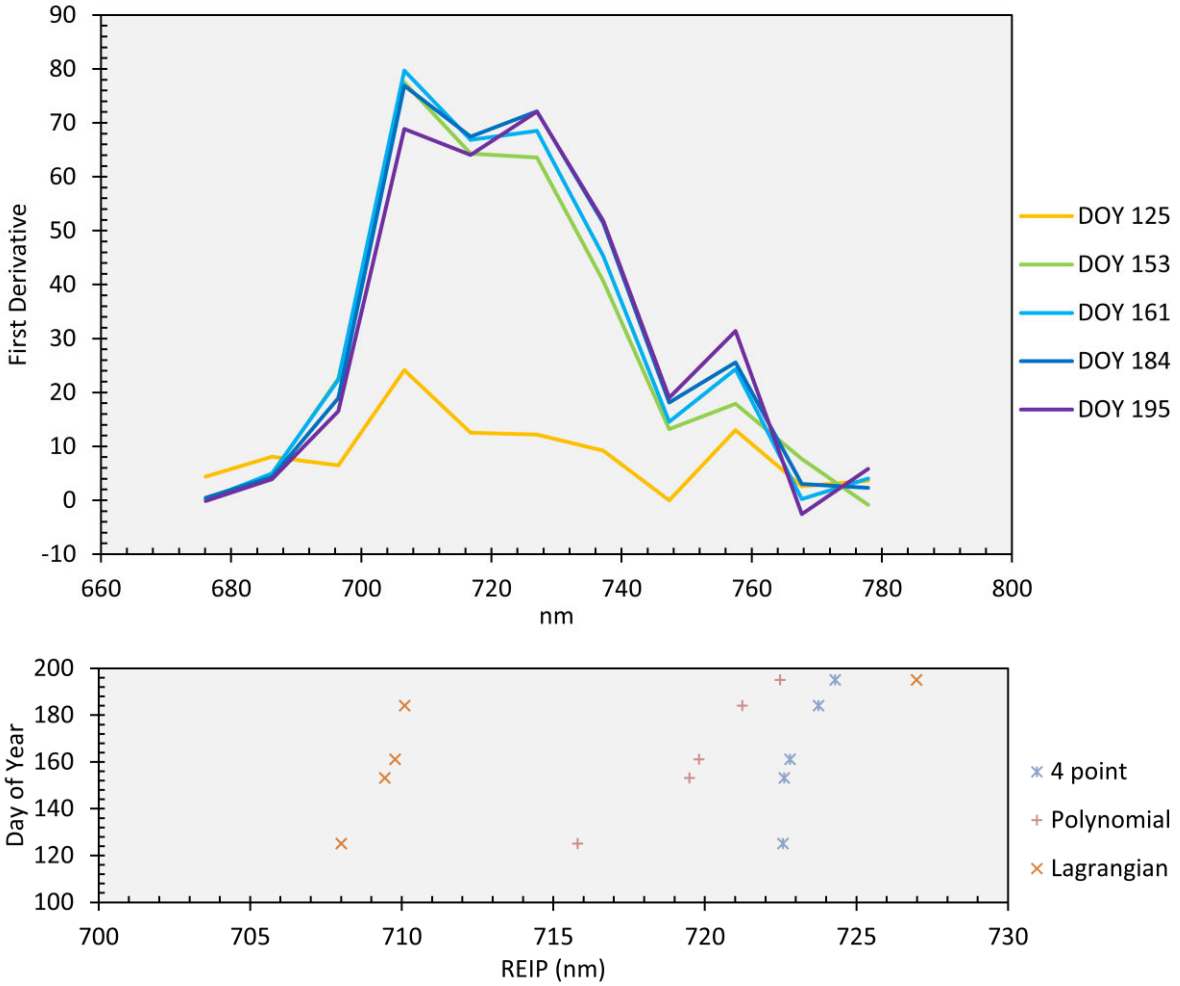

Figure 38. Seasonal development of the Hyperion red edge in the H3 birch site. Lines show the first derivative values for wavelengths in between Hyperion bands for the red edge (top). Markers show the calculated REIP (bottom).

surpassing the first derivative value at 716n at the two final dates. With the decrease in the height of the first peak at DOY 195 we see the second peak almost reach the same height. The REIP calculation results show little change with time, especially for the four-point linear interpolation and the Lagrangian interpolation method. The Lagrangian shows the REIP consistently near the first peak, with the four-point linear interpolation results being nearer the second. The polynomial fitting method shows a REIP in between the two peaks, with a shift towards the second peak as the latter becomes stronger.

Figure 39 shows a clear growth of the second peak in the U18 pine site. The first peak stays almost constant after DOY 125. The second peak grows gradually over the season, almost reaching the level of the first peak at DOY 195. As with the previous site the REIP calculated with the Lagrangian interpolation and four-point linear interpolation stay almost constant. The REIP from the polynomial fitting method shifts towards the NIR as the second

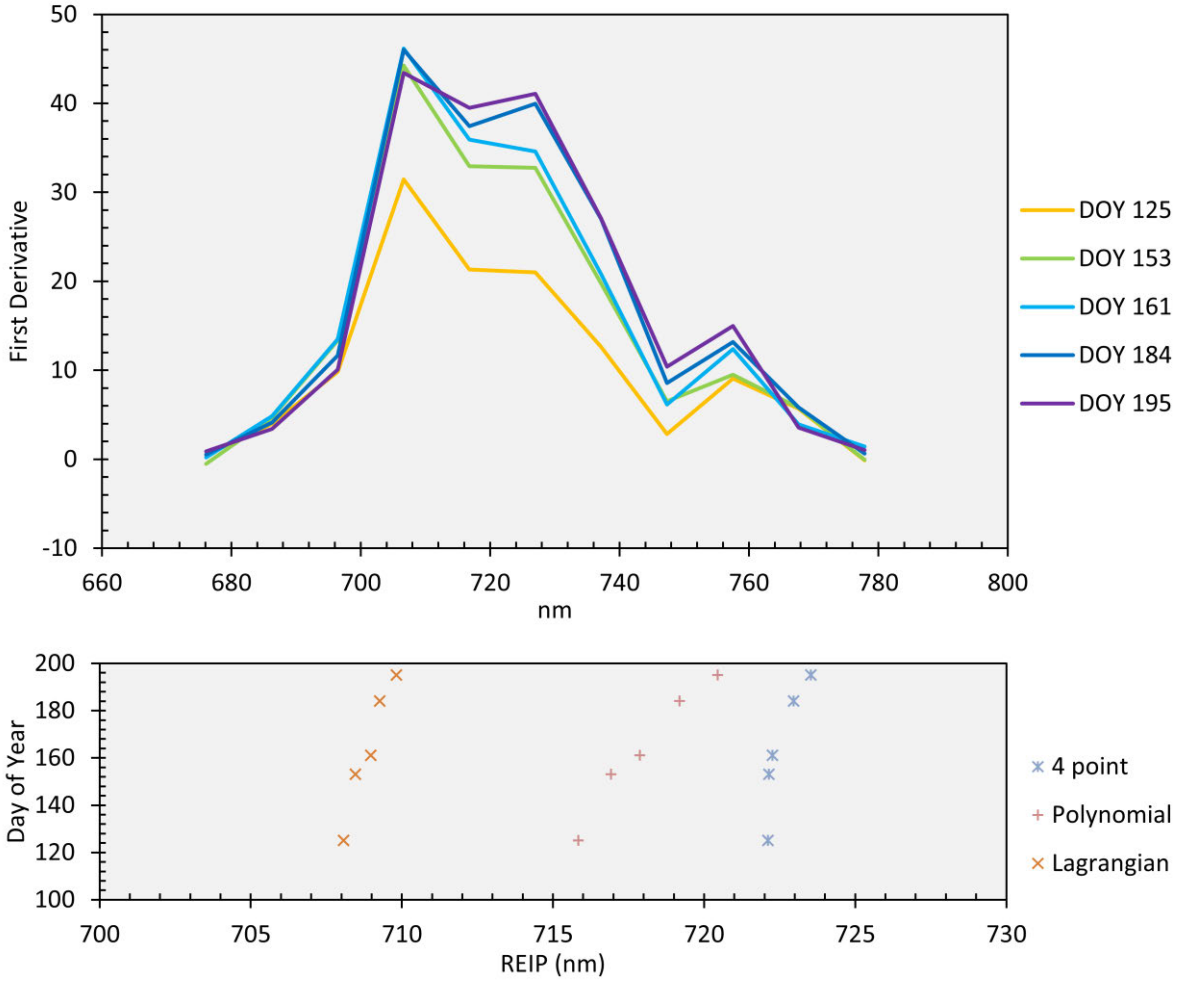

Figure 39. Seasonal development of the Hyperion red edge in the U18 pine site. Lines show the first derivative values for wavelengths in between Hyperion bands for the red edge (top). Markers show the calculated REIP (bottom).

peak grows.

Figure 38 from the H3 birch site slightly differs from the two previous plots due to it being broadleaf compared to coniferous. The two peaked nature of the derivative is still present. The second peak even surpasses the first peak at DOY 195. As the second peak becomes the highest peak the Lagrangian interpolation result changes dramatically: with a slight change in the first derivative the REIP jumps about 20nm towards the NIR. The four-point linear interpolation shows very little change over the season as with the previous sites. The polynomial fitting method shows a gradual shift towards the NIR as the second peak grows.

Pu et al. (2003) recommend the four-point linear interpolation method specifically for Hyperion data. In this study however, the method produced little seasonal variation in the REIP from either Hyperion or field spectroscopy data (Figure 30 and Figure 31). The red edge is not a linear feature with a simple peak in reflectance growth as is assumed by the four-point linear interpolation. By making that assumption, the four-point linear interpolation is more an indicator of the ratio between reflectance at red and NIR. The Lagrangian method would perhaps be better suited to sensors which only have one band in the red edge region. For Hyperion it is too sensitive to the second peak surpassing the first, and otherwise shows very little variation. The dynamic of the red edge explains why the polynomial fitting method works best for Hyperion data. While the polynomial fitting does not directly take into account the two peaked nature of the red edge first derivative. Using a fifth-order polynomial allows for a good fit to the actual shape of the red edge, and the fitted polynomial only has one peak in its first derivative. This peak is located in between the two direct first derivative peaks, but is sensitive to the growth of either peak.

The two peaked nature of the red edge has been identified by previous studies (Filella and Peñuelas, 1994; Kodani *et al*., 2002). The underlying reason for the two peaked nature has not been identified. The red edge in vegetation is generally seen as being influenced only by chlorophyll absorption in visible wavelengths and plant cell structure in the NIR. It is however likely that the red edge is directly influenced by some absorption feature, which is hidden by the high rate of change of reflectance found in the region.

6. CONCLUSIONS

Hyperion data requires extensive processing before it can be utilized; the process is however well documented and good results can be achieved. For monitoring vegetation the spatial resolution is sufficient while the high spectral resolution opens up a number of possibilities for further study.

Both ATCOR and FLAASH performed well for atmospheric correction. The spectral calibration of Hyperion is likely not accurate enough for either method to produce perfect results. The use of either algorithm could be justified. In comparison to a field calibration site both algorithms produced RMSE values of under 6% for all scenes, and under 2% for three scenes. Aerosol retrieval did not work with either algorithm, on any scene. In addition the use of a sun photometer for aerosol level estimation was not effective. Further research is needed to determine the optimal method of aerosol retrieval for Hyperion imagery; however an optical weather sensor provided a good guideline for FLAASH processing.

There are number of suggested methods for calculating REIP from Hyperion data, only fifth-order polynomial fitting method showed the expected trend in REIP over the growing season. The other methods showed either very little change in REIP or were too sensitive to noise. The red edge itself does not seem to be as straightforward as assumed. A clear double peak can be seen in first derivative of the Hyperion red edge. The polynomial fitting method performs well despite this.

There was no correlation overall between LAI and Hyperion REIP in this study. However on a site specific basis the correlation was high. Hyperion REIP was more closely correlated with understory REIP than LAI.

7. ACKNOWLEDGEMENTS

The LAIDetectives group made this study possible and provided extensive help and critique throughout the thesis. Specifically thanks to Miina Rautiainen for her confidence in my abilities and Janne Heiskanen for his expertise in processing satellite imagery.

A special thanks to Matti Mõttus for his patience and encouragement along the way.

This study was funded by Emil Aaltonen Foundation and the University of Helsinki Research Funds.

MODIS data was provided courtesy of NASA LP DAAC. Hyperion data was provided courtesy of the USGS.

The author would like to thank Titta Majasalmi and Anu Akujärvi for field work collecting and preprocessing the LAI and field spectroscopy data.

Guillaume Drolet, from the University of Edinburgh, provided the original SpecMM processing script.

A trial ATCOR license was provided for the study by Daniel Schläpfer.

REFERENCES

ASD, 1999. ASD Technical Guide 3rd Ed. Section 0-1

Bannon, D., 2009. Hyperspectral imaging: Cubes and slices. *Nature Photonics*, 3, pp.627-629

Barry, P., 2001. *EO-1/ Hyperion Science Data User's Guide, Level 1_B*, TRW Space, Defense & Information Systems

Berk, A., Bernstein, L.S., Anderson, G.P., Acharya, P.K., Robertson, D.C., Chetwynd, J.H. and Adler-Golden, M., 1998. MODTRAN Cloud and Multiple Scattering Upgrades with Application to AVIRIS. *Remote Sensing of Environment,* 65(3), pp.367-375

Bonhan-Carter, G. F., 1988. Numerical procedures and computer program for fitting an inverted Gaussian model to vegetation reflectance data. *Computers & Geosciences,* 14(3), pp.339-356

Campell, J.B., 1996. *Introduction to Remote Sensing*, 2nd ed. New York: The Guilford Press

Centre National d'Études Spatiales (CNES), 2011. VENμS satellite. [online] (Last updated 13 January 2011) Available at: <http://smsc.cnes.fr/VENUS/GP_satellite.htm> [Accessed 27 March 2012].

Chen, J.M., Black, T.A., 1992. Defining leaf area index for non flat leaves. *Plant Cell and Environment*, 15, pp.421-429.

Chen, J.M., Rich, P.M., Gower, S.T., Norman, J.M. and Plummer, S., 1997. Leaf area index of boreal forests: Theory, techniques, and measurements. *Journal of Geophysical Research*, 102(D24), pp.29429-29443

Cho, M. A., and Skidmore, A. K., 2006. A new technique for extracting the red edge position from hyperspectral data: The linear extrapolation method. *Remote Sensing of Environment,* 101, pp.181-193

Clark, B., Suomalainen J. and Pellikka P., 2010. A comparison of methods for the retrieval of surface reflectance factor from multi-temporal SPOT HRV, HRVIR and HRG multispectral satellite imagery. *Canadian Journal of Remote Sensing,* 36, pp.397–411

Commonwealth Scientific and Industrial Research Organisation (CSIRO), 2002. *Discussions around Hyperion Data: Background Notes for the Hyperion Data Users Workshop*, Contributions from: Jupp, D.L.B., Datt B., Lovell, J., Campbell S., King, E., the [A]SVT and others.

Darvishzadeha, R., Atzbergerb, C., Skidmorec, A. K. and Abkard, A. A., 2009. Leaf Area Index derivation from hyperspectral vegetation indices and the red edge position. *International Journal of Remote Sensing,* 30(23), pp.6199-6218

Datt B., McVicar T.R., VanNiel T. G., Jupp D.L.B., and Pearlman J. S., 2003. Preprocessing EO-1 Hyperion Hyperspectral Data to Support the Application of Agricultural Indexes. *IEEE Transactions on Geoscience Remote Sensing*, 41(6)

Dawson, T.P. and Curran, P.J., 1998. A new technique for interpolating the reflectance red edge position. *International Journal of Remote Sensing*, 19, pp.2133-2139

Deutsche Forschungsanstalt für Luft- und Raumfahrt (DLR) 2012. EnMAP Sensor. [online] Available at: <http://www.enmap.org/sensor> [Accessed 27 March 2012].

DLBJ, 2002. Report on work done during the US Visit and SVT Meeting by DLBJ & Jay. [online] Available at: <http://www.cossa.csiro.au/hswww/oz_pi/dlbj_us_0402.htm>, [Accessed 09 August 2011].

Du, H., Fuh, R. A., Li, J., Corkan, A. and Lindsey, J. S., 1998. PhotochemCAD: A computer-aided design and research tool in photochemistry. *Photochemistry and Photobiology,* 68, pp.141-142

ENVI, 2009, *Atmospheric Correction Module Version 4.7: QUAC and FLAASH User's Guide*, ITT Visual Information Solutions

European Space Agency (ESA), 2011. Sentinel-2. [online] (Last updated 7 March 2011) Available at: <http://www.esa.int/esaLP/SEMM4T4KXMF_LPgmes_0.html> [Accessed 27 March 2012].

ESRL, N.D. Earth System research laboratory, Trends in Atmospheric Carbon Dioxide [online] Available at: <http://www.esrl.noaa.gov/gmd/ccgg/trends/co2_data_mlo.html> [Accessed 27 March 2012].

Felde, G.W., Anderson, G.P., Cooley, T.W., Matthew, M.W., adler-Golden, S.M., Berk, A. and Lee, J., 2003. Analysis of Hyperion data with the FLAASH atmospheric correction algorithm. Proceedings of the Geoscience and Remote Sensing Symposium, IGARSS 2003. pp.90-92

Filella, I. and Peñuelas, J., 1994. The red edge position and shape as indicators of plant chlorophyll content, biomass and hydric status. *International Journal of Remote Sensing*, 15(7), pp.1459-1470

Gao, X., Huete, A.R., and Didan, K., 2003. Multisensor Comparisons and Validation of MODIS Vegetation Indices at the Semiarid Jornada Experimental Range. *IEEE Tranactions on Geoscience and Remote Sensing*, 41(10), pp. 2368-2381

Gao, B.C., Davis, C.O. and Goetz, A.F.H., 2006, A review of atmospheric correction techniques for hyperspectral remote sensing of land surfaces and ocean color. *IEEE International Conference on Geoscience and Remote Sensing Symposium*, IGARSS 2006. pp.1979-1981.

Gates, D.M., Keegan, H.J., Schleter J.C. and Weidner, V.R., 1965. Spectral Properties of Plants. *Applied Optics*, 4(1)

Goodenough, D.G., Dyk, A., Niemann, K.O., Pearlman, J.S., Chen, H., Han, T., Murdoch, M. and West, C., 2003. Processing Hyperion and ALI for Forest Classification. *IEEE Transactions on Geoscience Remote Sensing*, 41, pp.1321-1331

Guyot, G. and Baret, F., 1988. Utilisation de la haute resolution spectrale pour suivre l'etat des couverts vegetaux (Utilisation of the high spectral resolution to follow the status of the covered vegetation). *Proceedings of the Fourth International Colloquium on Spectral Signatures of Objects in Remote Sensing*. Aussois, France 18-22 January 1988, ESA SP-287. pp.279-286.

Guyot, G., Baret, F. and Jacquemoud, S., 1992. Imaging spectroscopy for vegetation studies. *Imaging Spectroscopy: Fundamentals and Prospective Application*, pp.145-165

Hari, P. & Kulmala, M., 2005. Station for Measuring Ecosystem-Atmosphere Relations (SMEAR II). *Boreal Environment Research*, 10. pp.315-322

Herrmann, I., Pimstein, A., Karnieli, A., Cohen, Y., Alchanatis, V. and Bonfil, D. J., 2010. Assessment of leaf area index by the red-edge inflection point derived from VENμS bands. *Proceedings 'Hyperspectral 2010 Workshop'*, Frascati, Italy, 17-19 March 2010, ESA SP-683

Horvath, H., 1971. On the applicability of the Koschmieder visibility formula. *Atmospheric Environment*, 5(3), pp.177-184

Huete, A., Didan, K., Miura, T., Rodriguez, E.P., Gao X. and Ferreira, L.G., 2002, Overview of the radiometric and biophysical performance of the MODIS vegetation indices, *Remote Sensing of Environment*, 83, pp.195-213.

Jago, R.A., Cutler, M.E.J. and Curran, P.J., 1999. Estimating canopy chlorophyll concentration from field and airborne spectra. *Remote Sensing of Environment*, 68, pp.217-224

Jeffrey, A., 1985. *Mathematics for Engineers and Scientists.* Wokingham, UK: Van Nostrand Reinhold

Jensen, J.R., 1996. *Introductory digital image processing*, 2nd ed. Upper Saddle River (NJ): Prentice Hall.

Jensen, J.R., 2000 remote sensing of the environment. Upper Saddle River (NJ): Prentice Hall.

Jimenez, L.O. and Landgrebe, D.A., 1999, Hyperspectral Data Analysis and Supervised. Feature Reduction Via Projection Pursuit. *IEEE Tranactions on Geoscience and Remote Sensing*, 37(6), pp.2653-2667.

Karpouzli, E. and Malthus, T., 2003. The empirical line method for the atmospheric correction of IKONOS imagery. International Journal of Remote Sensing, 24(5), pp.1143-1150

Kaufman, Y.J., Wald, A.E., Remer, L.A., Gao, B.-C., Li, R.-R. and Flynn L., 1997. The MODIS 2.1-μm Channel-Correlation with Visible Reflectance for Use in Remote Sensing of Aerosol. *IEEE Transactions on Geoscience Remote Sensing*, 35, pp.1286-1298

Khurshid, K.S., Staenz, K., Sun, L., Neville, R., White, H.P., Bannari, A., Champagne, C.M. and Hitchcock, R., 2006. Preprocessing of EO-1 Hyperion data, *Canadian Journal of Remote Sensing*, 32(2), pp.84-97

Kodani, E., Awaya, Y. and Tanaka, K., 2001. Seasonal patterns of canopy structure, biochemistry and spectral reflectance in a broad-leaved deciduous *Fagus crenata* canopy. *Forest Ecology and Management*, 167, pp.233-249

Li, Y., Demetriades-Shah, T.H., Kanemasu, E.T., Shultis, J.K. and Kirkham, M.B., 1993. Use of second derivatives of canopy reflectance for monitoring prairie vegetation over different soil backgrounds. *Remote Sensing of Environment*, 44(1), pp.81-87

LI-COR, 1992. *LAI-2000 Plant Canopy Analyzer: Instruction Manual*. Lincoln, Nebraska, LI-COR, Inc.

Liang, S., 2004. *Quantitative Remote Sensing of Land Surfaces*. Hobokenk, New Jersey: John Wiley and Sons, Inc.

Liang, S., Fang, H., and Chen, M., 2001. Atmospheric correction of Landsat ETM+ surface imagery - Part I: Methods. *IEEE Transactions on Geoscience and Remote Sensing*, 39(11), pp. 2490-2498

Majasalmi, T., Rautiainen, M., Stenberg, P. and Rita H., 2012, Optimizing the sampling scheme for LAI-2000 measurements in a boreal forest. *Agricultural and Forest Meteorology* 154-155, pp.38-43

Maliet, E. and Poinsignon, V., 2006. A superspectral microsatellite system for GMES land cover applications. *Acta Astronautica*, 59, (1-5), pp.107-112

McVicar, T.R., Niel, T.G.V. and Jupp, D.L.B., 2001. Geometric Validation of Hyperion Data acquired by Earth Observing 1 Satellite at Coleambally Irrigation Area. *CSIRO Land and Water*, Draft XX/01, October

Mutanga, O. and Skidmore, A.K., 2004. Narrow band vegetation indices overcome the saturation problem in biomass estimation. *International Journal of Remote Sensing*, 25(19), p.3999-4014

Myneni, R., Keeling, C., Tucker, C., Asrar G. and Nemani, R., 1997. Increased plant growth in the northern high latitudes from 1981 to 1991. *Nature,* 386, pp.698-702

NASA, 2007. AERONET SYSTEM DESCRIPTION. [online] (Last updated 04 December 2007) Available at: <http://aeronet.gsfc.nasa.gov/new_web/system_descriptions_instrument.html> [Accessed 27 March 2012].

NASA, 2009a. NASA 2008 HyspIRI Whitepaper and Workshop Report. [online] (Last updated May 2009) Pasadena, California: Jet Propulsion Laboratory, California Institute of Technology. Available at: <http://hyspiri.jpl.nasa.gov/downloads/2008_Workshop/2008%20HyspIRI%20Whitepaper%20and%20Science%20Workshop%20Report-r2.pdf> [Accessed 28 March 2012].

NASA, 2009b. Aerosol Angstrom Exponent. [online] (Last updated 24 November 2009) Available at: <http://disc.sci.gsfc.nasa.gov/data-holdings/PIP/aerosol_angstrom_exponent.shtml> [Accessed 27 March 2012].

NASA, 2011. Aerosol Optical Thickness. [online] (Last updated 02 December 2011) Available at: <http://daac.gsfc.nasa.gov/data-holdings/PIP/aerosol_optical_thickness_or_depth.shtml> [Accessed 27 March 2012].

NASA, n.d. MODIS Specifications. [online] Available at: <http://modis.gsfc.nasa.gov/about/specifications.php> [Accessed 27 March 2012].

Pearlman, J.S., Barry P.S., Segal C.C., Shepanski J., Beiso D. and Carman S.L., 2003, Hyperion, a Space-Based Imaging Spectrometer, *IEEE Transactions on Geoscience Remote Sensing*, 41

Pu, R., Gong, P., Biging, G.S. and Larrieu, M.R., 2003. Extraction of red edge optical parameters from Hyperion data for estimation of forest leaf area index. *IEEE Transactions on Geoscience Remote Sensing*, 41, pp.916-921

Puschell, J.J., 2000, Hyperspectral imagers for current and future missions. *Proceedings of SPIE,* 4041, pp.121-132

Rautiainen, M., Nilson, T. and Lükk, T., 2009. Seasonal reflectance trends of hemiboreal birch forests. *Remote Sensing of Environment*, 113, pp.805-815.

Rautiainen, M., Mõttus, M., Heiskanen, J., Akujärvi, A., Majasalmi, T. and Stenberg, P., 2011. Seasonal reflectance dynamics of common understory types in a northern European boreal forest. *Remote Sensing of Environment*, 115, pp.3020-3028.

Richter, R. and Schläpfer, D., 2011. Atmospheric / Topographic Correction for Satellite Imagery, ATCOR-2/3 User Guide, Version 8.0.2, ReSe Applications Schläpfer

San, B.T. and Suzen M.L., 2010, Evaluation of Different Atmospheric Correction Algorithms for EO-1 Hyperion Imagery*, International Archives of the Photogrammetry, Remote Sensing and Spatial Information Science*, Volume XXXVIII, Part 8, Kyoto Japan

Schaaf, C., 2010. MODIS BRDF/Albedo Product (MCD43) User's Guide. [online] (Last updated January 2011) Available at: <http://www-modis.bu.edu/brdf/userguide/intro.html> [Accessed 27 March 2012].

Schlerf, M., Atzberger, C. and Hill, J., 2005. Remote sensing of forest biophysical variables using HyMap imaging spectrometer data. *Remote Sensing of Environment*, 95(2), pp.177-194

Silkina O.V. and Vinokurova R.I., 2009. Seasonal dynamics of chlorophyll and microelement content in developing conifer needles of *Abies sibirica* and *Picea abies*. *Russian Journal of Plant Physiology*, 56(6), pp.780-786

Strahler *et al*., 1999. MODIS BRDF/Albedo Product: Algorithm Theoretical Basis Document Version 5.0, MODIS Product ID: MOD43

Sun, L., Neville, R. and Staenz, K., 2008. Automatic destriping of Hyperion imagery based on spectral moment matching. *Canadian Journal for Remote Sensing*, 34 (S1), pp.S68-S81

Thenkabail, P.S., Smith, R.B. and DePauw, E., 2000. Hyperspectral vegetation indices and their relationships with agricultural crop characteristics. *Remote Sensing of Environment*, 71(2), pp.158-182

Ungar, S.G., Pearlman, J.S., Mendenhall J.A. and Reuter, D., 2003, Overview of the Earth Observing One (EO-1) Mission. *IEEE Transactions on Geoscience Remote Sensing*, 41(6), pp.1149-1159.

USGS, 2010a, Earth Observing 1 (EO-1). [online] (Last updated 02 November 2010) Available at: <http://edcsns17.cr.usgs.gov/eo1/> [Accessed 27.06.2011].

USGS, 2010b, Look Angles and Coverage Area. [online] (Last updated 02 November 2010) Available at: <http://edcsns17.cr.usgs.gov/eo1/acquisition/lookangle> [Accessed 27.06.2011].

USGS, 2011, Earth Observing 1 (EO-1). [online] (Last updated 20 December 2011) Available at: <http://eros.usgs.gov/#/Find_Data/Products_and_Data_Available/ALI> [Accessed 27 March 2012].

Vaisala, 2002, Weather Sensor FD12P, User's Guide, Vaisala

Vermote E.F., Tanre D., Deuze J.L., Herman M. and Morcrette J.J., 1997. Second Simulation of the Satellite Signal in the Solar Spectrum, 6S: An Overview, *IEEE Tranactions on Geoscience and Remote Sensing*, 35(3), pp.675-686

Vermote, E.F. and Vermeulen, A., 1999. MODIS Algorithm Technical Background Document ATMOSPHERIC CORRECTION ALGORITHM: SPECTRAL REFLECTANCES (MOD09) Version 4.0.

Vermote, E.F., Kotchenova S.Y. and Ray J.P., 2011. MODIS Surface Reflectance User's Guide, MODIS Land Surface Reflectance Science Computing Facility, Version 1.3.

Wade, T. and Sommer, S. (editors), 2006. *A to Z GIS*, 2nd ed. Redlands, California: ESRI Press

Watson, D., 1947. Comparative physiological studies in the growth of field crops. I. Variation in net assimilation rate and leaf area between species and varieties, and within and between years. *Annales of Botany*, 11(1), pp.41-76

Yuan, Jinguo and Zheng Niu, 2008, *Evaluation of Atmospheric Correction Using FLAASH,* International Workshop on Earth Observation and Remote Sensing Applications

APPENDIX

A – Hyperion Bands

Band	Original wavelength (nm)	Set to 0	WL after desmile (nm)	FWHM (nm)
1	355,6	Yes		11,39
2	365,8	Yes		11,39
3	375,9	Yes		11,39
4	386,1	Yes		11,39
5	396,3	Yes		11,39
6	406,5	Yes		11,39
7	416,6	Yes		11,39
8	426,8	No	426,82	11,39
9	437,0	No	436,99	11,39
10	447,2	No	447,17	11,39
11	457,3	No	457,34	11,39
12	467,5	No	467,52	11,39
13	477,7	No	477,69	11,39
14	487,9	No	487,87	11,38
15	498,0	No	498,04	11,35
16	508,2	No	508,22	11,31
17	518,4	No	518,39	11,26
18	528,6	No	528,57	11,19
19	538,7	No	538,74	11,11
20	548,9	No	548,92	11,02
21	559,1	No	559,09	10,93
22	569,3	No	569,27	10,84
23	579,4	No	579,45	10,74
24	589,6	No	589,62	10,65
25	599,8	No	599,80	10,56
26	610,0	No	609,97	10,48
27	620,1	No	620,15	10,41
28	630,3	No	630,32	10,36
29	640,5	No	640,50	10,32
30	650,7	No	650,67	10,29
31	660,8	No	660,85	10,29
32	671,0	No	671,02	10,30
33	681,2	No	681,20	10,33
34	691,4	No	691,37	10,39
35	701,5	No	701,55	10,46
36	711,7	No	711,72	10,53
37	721,9	No	721,90	10,60
38	732,1	No	732,07	10,66
39	742,3	No	742,25	10,69
40	752,4	No	752,43	10,71
41	762,6	No	762,60	10,73
42	772,8	No	772,78	10,79
43	783,0	No	782,95	10,88
44	793,1	No	793,13	10,99
45	803,3	No	803,30	11,10
46	813,5	No	813,48	11,20
47	823,7	No	823,65	11,26
48	833,8	No	833,83	11,28
49	844,0	No	844,00	11,28
50	854,2	No	854,18	11,28
51	864,4	No	864,35	11,28
52	874,5	No	874,53	11,28
53	884,7	No	884,70	11,28
54	894,9	No	894,88	11,28
55	905,1	No	905,05	11,28
56	915,2	No	915,23	11,28
57	925,4	No	925,41	11,28
58	935,6	Yes		11,28
59	945,8	Yes		11,28
60	955,9	Yes		11,28
61	966,1	Yes		11,28
62	976,3	Yes		11,28
63	986,5	Yes		11,28
64	996,6	Yes		11,28
65	1006,8	Yes		11,28
66	1017,0	Yes		11,28
67	1027,2	Yes		11,28
68	1037,3	Yes		11,28
69	1047,5	Yes		11,28
70	1057,7	Yes		11,28
71	851,9	Yes		11,28
72	862,0	Yes		11,28
73	872,1	Yes		11,28
74	882,2	Yes		11,28
75	892,3	Yes		11,28
76	902,4	Yes		11,28
77	912,5	No	912,45	11,05
78	922,5	No	922,54	11,05
79	932,6	No	932,64	11,05
80	942,7	No	942,73	11,05
81	952,8	No	952,82	11,05
82	962,9	No	962,91	11,05
83	973,0	No	972,99	11,05
84	983,1	No	983,08	11,05
85	993,2	No	993,17	11,05
86	1003,3	No	1003,30	11,05
87	1013,3	No	1013,30	11,05
88	1023,4	No	1023,40	11,05
89	1033,5	No	1033,50	11,05
90	1043,6	No	1043,59	11,04
91	1053,7	No	1053,69	11,04
92	1063,8	No	1063,79	11,03
93	1073,9	No	1073,89	11,02
94	1084,0	No	1083,99	11,01
95	1094,1	No	1094,09	11,00
96	1104,2	No	1104,18	10,99
97	1114,2	No	1114,18	10,97
98	1124,3	No	1124,28	10,96
99	1134,4	No	1134,38	10,94
100	1144,5	No	1144,48	10,92
101	1154,6	No	1154,58	10,91
102	1164,7	No	1164,68	10,89
103	1174,8	No	1174,77	10,87
104	1184,9	No	1184,87	10,85
105	1195,0	No	1194,97	10,83
106	1205,1	No	1205,07	10,82
107	1215,2	No	1215,17	10,80
108	1225,2	No	1225,17	10,78
109	1235,3	No	1235,27	10,77
110	1245,4	No	1245,36	10,75
111	1255,5	No	1255,46	10,74
112	1265,6	No	1265,56	10,73
113	1275,7	No	1275,66	10,72
114	1285,8	No	1285,76	10,71
115	1295,9	No	1295,86	10,70
116	1306,0	No	1305,96	10,70
117	1316,1	No	1316,05	10,69
118	1326,1	No	1326,05	10,69
119	1336,2	No	1336,15	10,69
120	1346,3	No	1346,25	10,70
121	1356,4	No	1356,35	10,71
122	1366,5	No	1366,45	10,72
123	1376,6	No	1376,55	10,73
124	1386,7	No	1386,64	10,74
125	1396,7	No	1396,74	10,76
126	1406,8	No	1406,84	10,78
127	1416,9	No	1416,94	10,80
128	1426,9	No	1426,94	10,83
129	1437,0	No	1437,04	10,85
130	1447,1	No	1447,14	10,88

Band	Original wavelength (nm)	Set to 0	WL after desmile (nm)	FWHM (nm)
131	1457,2	No	1457,23	10,91
132	1467,3	No	1467,33	10,94
133	1477,4	No	1477,43	10,97
134	1487,5	No	1487,53	11,01
135	1497,6	No	1497,63	11,04
136	1507,7	No	1507,73	11,08
137	1517,8	No	1517,83	11,11
138	1527,9	No	1527,92	11,15
139	1537,9	No	1537,92	11,18
140	1548,0	No	1548,02	11,22
141	1558,1	No	1558,12	11,25
142	1568,2	No	1568,22	11,28
143	1578,3	No	1578,32	11,31
144	1588,4	No	1588,42	11,35
145	1598,5	No	1598,51	11,38
146	1608,6	No	1608,61	11,40
147	1618,7	No	1618,71	11,43
148	1628,8	No	1628,81	11,45
149	1638,8	No	1638,81	11,48
150	1648,9	No	1648,91	11,50
151	1659,0	No	1659,01	11,51
152	1669,1	No	1669,10	11,53
153	1679,2	No	1679,20	11,54
154	1689,3	No	1689,30	11,55
155	1699,4	No	1699,40	11,56
156	1709,5	No	1709,50	11,56
157	1719,6	No	1719,60	11,56
158	1729,7	No	1729,70	11,56
159	1739,7	No	1739,69	11,56
160	1749,8	No	1749,79	11,55
161	1759,9	No	1759,89	11,53
162	1770,0	No	1769,99	11,52
163	1780,1	No	1780,09	11,50
164	1790,2	No	1790,19	11,48
165	1800,3	No	1800,29	11,45
166	1810,4	No	1810,38	11,43
167	1820,5	No	1820,48	11,40
168	1830,6	No	1830,58	11,37
169	1840,6	No	1840,58	11,34
170	1850,7	No	1850,68	11,30
171	1860,8	No	1860,78	11,27
172	1870,9	No	1870,87	11,24
173	1881,0	No	1880,97	11,20
174	1891,1	No	1891,07	11,17
175	1901,2	No	1901,17	11,13
176	1911,3	No	1911,27	11,10
177	1921,4	No	1921,37	11,07
178	1931,5	No	1931,47	11,04
179	1941,6	No	1941,57	11,02
180	1951,6	No	1951,56	10,99
181	1961,7	No	1961,66	10,97
182	1971,8	No	1971,76	10,95
183	1981,9	No	1981,86	10,94
184	1992,0	No	1991,96	10,92
185	2002,1	No	2002,06	10,91
186	2012,2	No	2012,16	10,91
187	2022,3	No	2022,25	10,91
188	2032,4	No	2032,35	10,91

Band	Original wavelength (nm)	Set to 0	WL after desmile (nm)	FWHM (nm)
189	2042,5	No	2042,45	10,90
190	2052,5	No	2052,45	10,90
191	2062,6	No	2062,55	10,89
192	2072,7	No	2072,65	10,87
193	2082,8	No	2082,75	10,86
194	2092,8	No	2092,84	10,84
195	2102,9	No	2102,94	10,82
196	2113,0	No	2113,04	10,80
197	2123,1	No	2123,14	10,78
198	2133,2	No	2133,24	10,76
199	2143,3	No	2143,34	10,73
200	2153,3	No	2153,34	10,71
201	2163,4	No	2163,43	10,68
202	2173,5	No	2173,53	10,66
203	2183,6	No	2183,63	10,63
204	2193,7	No	2193,73	10,61
205	2203,8	No	2203,83	10,58
206	2213,9	No	2213,93	10,56
207	2224,0	No	2224,02	10,53
208	2234,1	No	2234,12	10,51
209	2244,2	No	2244,22	10,49
210	2254,2	No	2254,22	10,47
211	2264,3	No	2264,32	10,46
212	2274,4	No	2274,42	10,44
213	2284,5	No	2284,52	10,43
214	2294,6	No	2294,62	10,42
215	2304,7	No	2304,71	10,41
216	2314,8	No	2314,81	10,41
217	2324,9	No	2324,91	10,41
218	2335,0	No	2335,01	10,41
219	2345,1	No	2345,11	10,41
220	2355,2	No	2355,21	10,41
221	2365,2	No	2365,20	10,41
222	2375,3	No	2375,30	10,41
223	2385,4	No	2385,40	10,41
224	2395,5	No	2395,50	10,41
225	2405,6	Yes		10,41
226	2415,7	Yes		10,41
227	2425,8	Yes		10,41
228	2435,9	Yes		10,41
229	2446,0	Yes		10,41
230	2456,1	Yes		10,41
231	2466,1	Yes		10,41
232	2476,2	Yes		10,41
233	2486,3	Yes		10,41
234	2496,4	Yes		10,41
235	2506,5	Yes		10,41
236	2516,6	Yes		10,41
237	2526,7	Yes		10,41
238	2536,8	Yes		10,41
239	2546,9	Yes		10,41
240	2557,0	Yes		10,41
241	2567,0	Yes		10,41
242	2577,1	Yes		10,41